Downloaded from orbit.dtu.dk on: Oct 14, 2026

DTU Library

Analysis of Data from the Gedser Wind Turbine 1977-1979

Lundsager, P.; Frandsen, Sten Tronæs; Christensen, Carl Jørgen

Publication date:
1980

Document Version
Publisher's PDF, also known as Version of record

Link back to DTU Orbit

Citation (APA):
Lundsager, P., Frandsen, S. T., & Christensen, C. J. (1980). *Analysis of Data from the Gedser Wind Turbine 1977-1979*. Risø National Laboratory. Risø-M No. M-2242

General rights
Copyright and moral rights for the publications made accessible in the public portal are retained by the authors and/or other copyright owners and it is a condition of accessing publications that users recognise and abide by the legal requirements associated with these rights.

- Users may download and print one copy of any publication from the public portal for the purpose of private study or research.
- You may not further distribute the material or use it for any profit-making activity or commercial gain
- You may freely distribute the URL identifying the publication in the public portal

If you believe that this document breaches copyright please contact us providing details, and we will remove access to the work immediately and investigate your claim.

RISØ-M-2242

ANALYSIS OF DATA FROM THE GEDSER WIND TURBINE 1977-1979

P. Lundsager, S. Frandsen, C.J. Christensen

Abstract. In this report a number of topics have been chosen for further analysis, based on the data from the Gedser wind turbine measurements, made during 1977 to 1979. The report contains chapters dealing with power characteristics based on 10 min. averages, coherence between measurements of wind and electric power based on high speed scanning, drive train oscillations and structural response of the rotor. In most of the chapters theoretical models are developed and evaluated. First chapter contains a summary of the measurements and last chapter contains a comparison of the Gedser wind turbine with modern Danish, Swedish and American experimental wind turbines, based on published data.

UDC 621.548 : 53.087

August 1980
Risø National Laboratory, DK-4000 Roskilde, Denmark

ISBN 87-550-0693-0
ISSN 0418-6435

Risø Repro 1980

LIST OF CONTENTS

	Page
1. SUMMARY OF MEASUREMENTS	9
2. LONG-TERM MEASUREMENTS, POWER CURVE	21
3. SHORT-TERM POWER MEASUREMENTS	37
4. POWER FLUCTUATIONS	56
5. ROTOR RESPONSE	70
6. COMPARISONS WITH OTHER TURBINES	105
Appendix I. THE ACCURACY OF THE CONVERTED DATA	120
Appendix II. ZERO CORRECTION	128

Preface

The work described in this report was carried out under contract with the Wind Power Program of the Ministry of Energy and the Electric Utilities in Denmark. Mr. Søren A. Jensen, M.Sc., of the Danish Ship Research Laboratory has under contract with Risø participated in the preparation of data for the chapters 2 and 6.

1. SUMMARY OF MEASUREMENTS

This chapter summarizes the measurements carried out on the Gedser wind turbine, Ref. 1.1.

The 200 kW Gedser windmill (Fig. 1.1 and Fig. 1.2) is the last and largest of 3 research wind turbines built in the 1950's by SEAS (Southeast Zealand Electricity Ltd.) and DEF (The Danish Association of Electricity Supply Undertakings), see Ref. 1.2. Table 1.1 shows a summary of the characteristics of the turbine, which deviates from the majority of new designs in that the rotor is 3-bladed, up-wind located and stall regulated. The blades are stiffened by a number of stays.

The wind turbine is located near Gedser in the southern part of the island Falster (Fig. 1.3). The site is characterized by its proximity to open sea in the prevailing wind direction (west) and a smooth landscape. Because of the long stretch where the wind is free to accelerate, the Gedser site is comparable to possible sites at the long west coast of Jutland, which are ordinarily counted as the best Danish sites for wind turbines.

Very few of the large wind turbines hitherto built have avoided major problems. One of those which did succeed is the Gedser wind turbine, which was in automatic operation during the years 1958-67 without major mechanical difficulties. Thus the design of the Gedser mill has proven to be quite successful for its time. It is therefore of considerable interest to study the design by studying the structural and aerodynamic response as well as the power production as a function of meteorological conditions.

The main objectives for this measuring program, as stated by DEF, (Ref. 1.3) are the determination of

(a) A power curve for the turbine.

Rotor location	Upwind
Rotor diameter	24 m
Number of blades	3
Blade tip velocity	38 m/s
Rotational velocity	30.19 rpm at zero slip
Rotor area	450 m^2
Blade construction	Steel, main spar, wooden webs, aluminium skin. Heavily stayed. Braking flaps in blade tips.
Regulation	Stall regulated, no pitch control
Generator	Asynchronous 200 kW, 750 rpm (1% slip at 200 kW)
Transmission	Double chain 1:24.84 (primary 1:4.74, secondary 1:5.24)
Tower	Stiffened concrete cylinder, hub height 24 m
Performance	Self-starting at 5 m/s 200 kW at 15 m/s Typical annual production 350.000 kWh/yr (Ref. 1.1)

Table 1.1. Main characteristics of the Gedser wind turbine.

(b) The loads on certain parts of the structure, especially the rotor, and the structural response under various conditions.

(c) The power quality. During the years of operation, power fluctuations were observed (Ref. 1.2).

To fulfil the aims of the program a number of parameters were measured. Two recording units were used: the readings of the sensors on the rotor were transmitted to a ground based receiver by means of a 28-channel telemetry system, while data from the

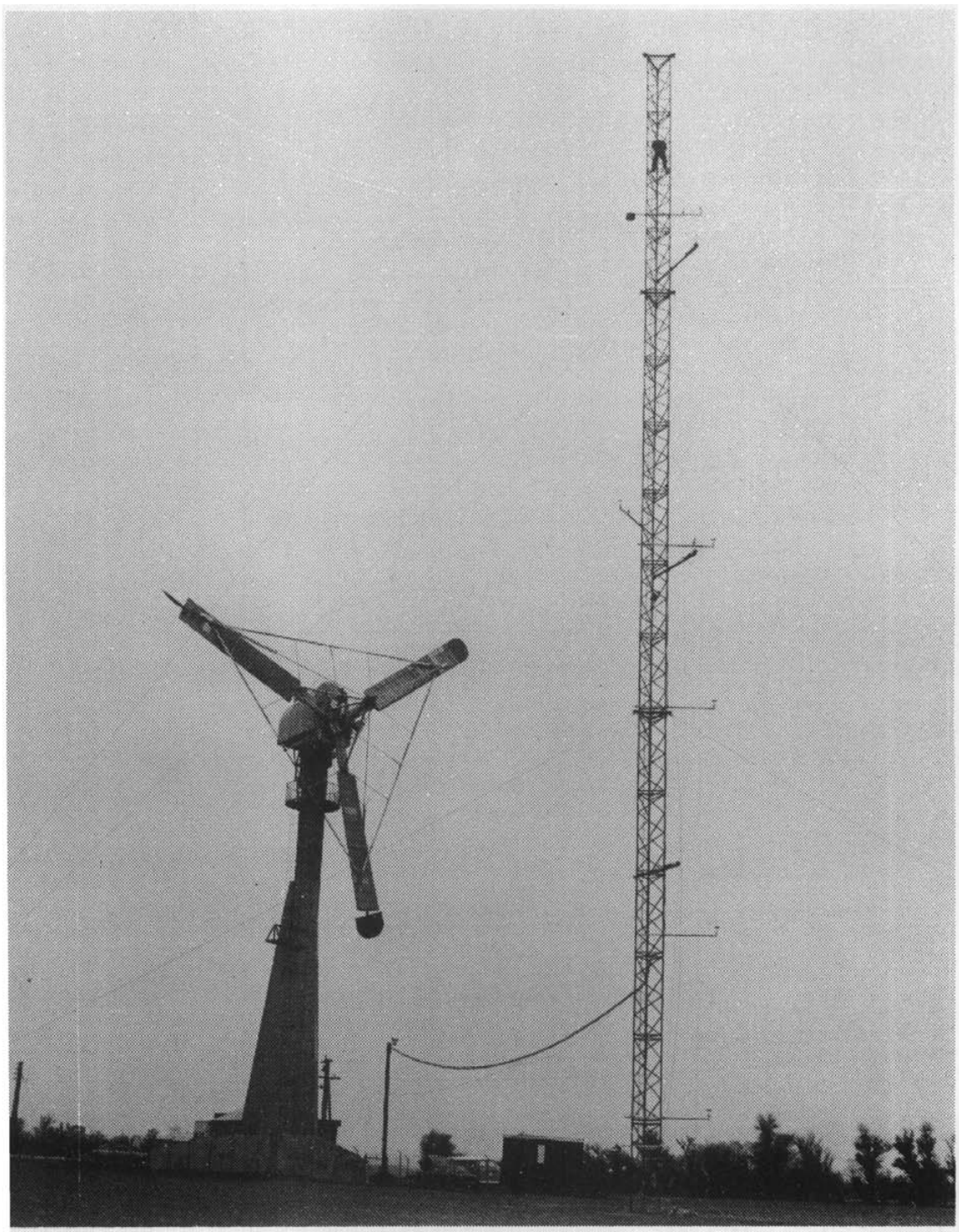

Fig. 1.1. The site of the Gedser wind turbine.

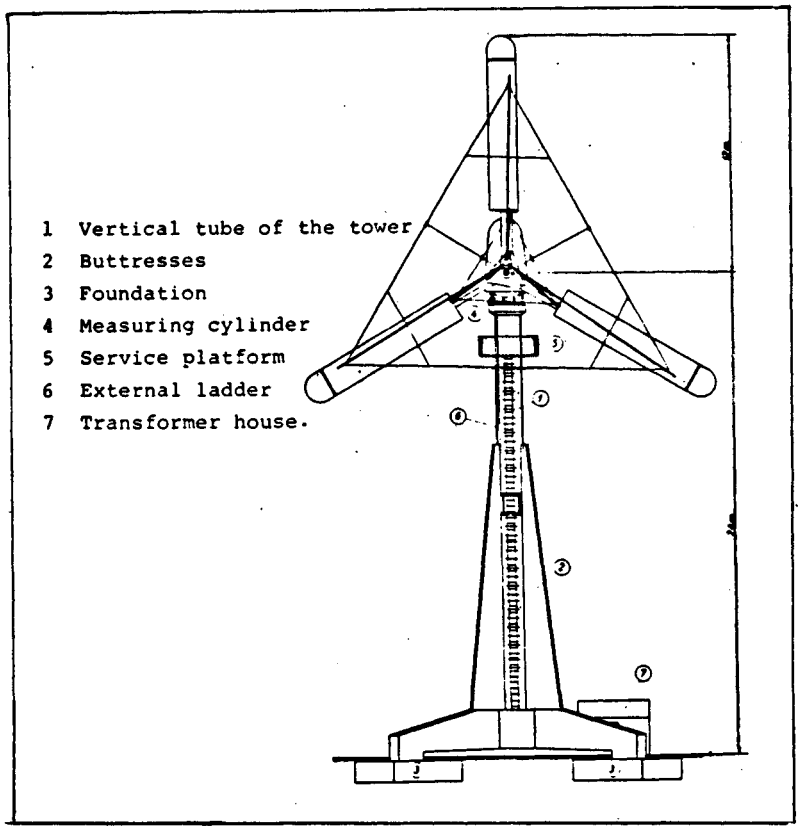

Fig. 1.2. The Gedser Wind Turbine.

nacelle, the turbine tower and the meteorological mast were sampled by another digital recording unit. The measured quantities are listed in Table 1.2 and their locations are shown in Fig. 1.4. The measured quantities can be described in summary as follows:

The rotor forces are in each run either described by 26 sensors which describe one blade or in some runs selected sensors attempting to describe the complete rotor rather than one blade.

The sensors measure flapwise, edgewise and torsional moments in 4 sections, the normal force in the innermost section, normal forces in 8 stays or wires connecting the blades plus 5 pressure differences between pressure and suction sides of the blade.

SENSOR NO	SYMBOL	DESCRIPTION			SENSOR GROUP
1	N11	AXIAL FORCE		SECT 1	
2	M11	TORSIONAL MOMENT		R= 1.42 M	1 (BLADE 3)
3	M21	BENDING MOMENT, CHORDWISE			
4	M31	BENDING MOMENT, FLAPWISE			
5	M12	TORSIONAL MOMENT		SECT 2	
6	M22	BENDING MOMENT, CHORDWISE		R= 4.72 M	
7	M32	BENDING MOMENT, FLAPWISE			(MAY BE
8	M13	TORSIONAL MOMENT		SECT 3	REPLACED
9	M23	BENDING MOMENT, CHORDWISE		R= 7.63 M	BY GROUP
10	M33	BENDING MOMENT, FLAPWISE			3 BLADE 2)
11	M14	TORSIONAL MOMENT		SECT 4	
12	M24	BENDING MOMENT, CHORDWISE		R= 9.56 M	
13	M34	BENDING MOMENT, FLAPWISE			
14	NIS	FORCE, INNER STAY			
15	NYS	FORCE, OUTER STAY			
16	NYB-31	FORCE, OUTER STAY FROM BLADE 3 TO BLADE 1			
17	NYB-32	FORCE, OUTER STAY FROM BLADE 3 TO BLADE 2			
18	NIB-31	FORCE, INNER STAY FROM BLADE 3 TO BLADE 1			
19	NIB-32	FORCE, INNER STAY FROM BLADE 3 TO BLADE 2			
20	NBS-31	FORCE, WIRE TO OUTER STAY FROM BLADE 3 TO BLADE 1			
21	NBS-32	FORCE, WIRE TO OUTER STAY FROM BLADE 3 TO BLADE 2			
22	PA	DIFFERENTIAL PRESSURE		R= 3.56 M	
23	PB	DIFFERENTIAL PRESSURE		R= 5.02 M	2
24	PC	DIFFERENTIAL PRESSURE		R= 6.85 M	
25	PD	DIFFERENTIAL PRESSURE		R= 7.94 M	BLADE 3
26	PE	DIFFERENTIAL PRESSURE		R= 10.35 M	
27	P1	HORIZONTAL FORCE	X_1-DIRECTION		
28	P2	HORIZONTAL FORCE	X_2-DIRECTION		4
29	M1	TILTING MOMENT	X_1-DIRECTION		
30	M2	TILTING MOMENT	X_2-DIRECTION		MEAS. CYL.
31	M3	TORSIONAL MOMENT	X_3-DIRECTION		
32	YAW	YAW RATE			
33	ACC X	ACCELLERATION	X-DIRECTION		5
34	ACC Y	ACCELLERATION	Y-DIRECTION		NACELLE
35	ACC W	ACCELLERATION	ω (ANGULAR)		
36	ROTPOS	ROTORPOSITION	1 PULSE/360°		6
37	ROTVEL		1 PULSE/1°		NACELLE
38	AZIMUT	NACELLE POSITION			
39		GENERATOR SHAFT TORQUE			7
40	TORQUE	SECONDARY SHAFT TORQUE			NACELLE
41	KVAR	KVAR			8
42	WKW	KWATT			NACELLE
43	VOLT	VOLT			
46	VA-12	X-COMPONENT WINDSPEED			
47	VB-12	Y-COMPONENT WINDSPEED		12 M	9
48	VC-12	Z-COMPONENT WINDSPEED			
49	T-12	TEMPERATURE			MET. TOWER
50	VA-24	X-COMPONENT WINDSPEED			
51	VB-24	Y-COMPONENT WINDSPEED		24 M	
52	VC-24	Z-COMPONENT WINDSPEED			
53	T-24	TEMPERATURE			
54	VA-36	X-COMPONENT WINDSPEED			
55	VB-36	Y-COMPONENT WINDSPEED		36 M	
56	VC-36	Z-COMPONENT WINDSPEED			
57	T-36	TEMPERATURE			
58		HORIZONTAL WINDSPEED		6 M	
59		HORIZONTAL WINDSPEED		12 M	10
60		HORIZONTAL WINDSPEED		24 M	
61		HORIZONTAL WINDSPEED		36 M	MET. TOWER
62		WIND DIRECTION		6 M	
63		WIND DIRECTION		12 M	
64		WIND DIRECTION		24 M	
65		WIND DIRECTION		36 M	
66		AIR TEMPERATURE		12 M	
67		AIR TEMPERATURE		36 M	
68		KWATT			NACELLE
44	WVEL 11	HORIZONTAL WINDSPEED		24 M	11
45	WDIR 1	WIND DIRECTION		24 M	MET. TOWER 1
88	WVEL 21	HORIZONTAL WINDSPEED		24 M	
89	WVEL 22	HORIZONTAL WINDSPEED		19 M	
90	WDIR	WIND DIRECTION		19 M	MET. MAST 2

Table 1.2. Sensors

SENSOR NO	SYMBOL	DESCRIPTION		SENSOR GROUP
69	N11	AXIAL FORCE	SECT 1	
70	M11	TORSIONAL MOMENT	R= 1.42 M	3 (BLADE 2)
71	M21	BENDING MOMENT, CHORDWISE		
72	M31	BENDING MOMENT, FLAPWISE		
73	M12	TORSIONAL MOMENT	SECT 2	
74	M22	BENDING MOMENT, CHORDWISE	R= 4.72 M	
75	M32	BENDING MOMENT, FLAPWISE		
76	M13	TORSIONAL MOMENT	SECT 3	(MAY REPLACE GROUP 1 BLADE 3)
77	M23	BENDING MOMENT, CHORDWISE	R= 7.63 M	
78	M33	BENDING MOMENT, FLAPWISE		
79	M14	TORSIONAL MOMENT	SECT 4	
80	M24	BENDING MOMENT, CHORDWISE	R= 9.56 M	
81	M34	BENDING MOMENT, FLAPWISE		
82	NIS	FORCE, INNER STAY		
83	NYS	FORCE, OUTER STAY		
84	NYB-21	FORCE, OUTER STAY FROM BLADE 2 TO BLADE 1		
85	NIB-21	FORCE, INNER STAY FROM BLADE 2 TO BLADE 1		
86	NBS-21	FORCE, WIRE TO OUTER STAY FROM BLADE 2 TO BLADE 1		
87	NBS-23	FORCE, WIRE TO OUTER STAY FROM BLADE 2 TO BLADE 3		

Table 1.2. Continued

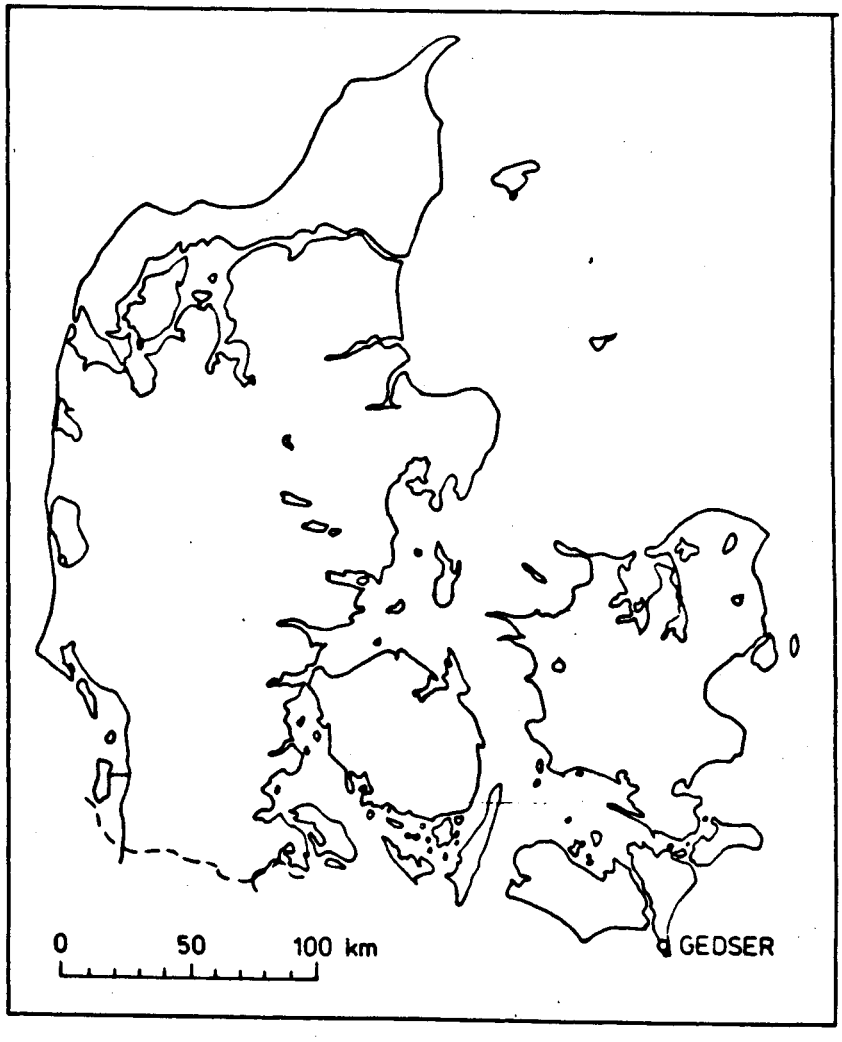

Fig. 1.3. Location of the Gedser wind turbine

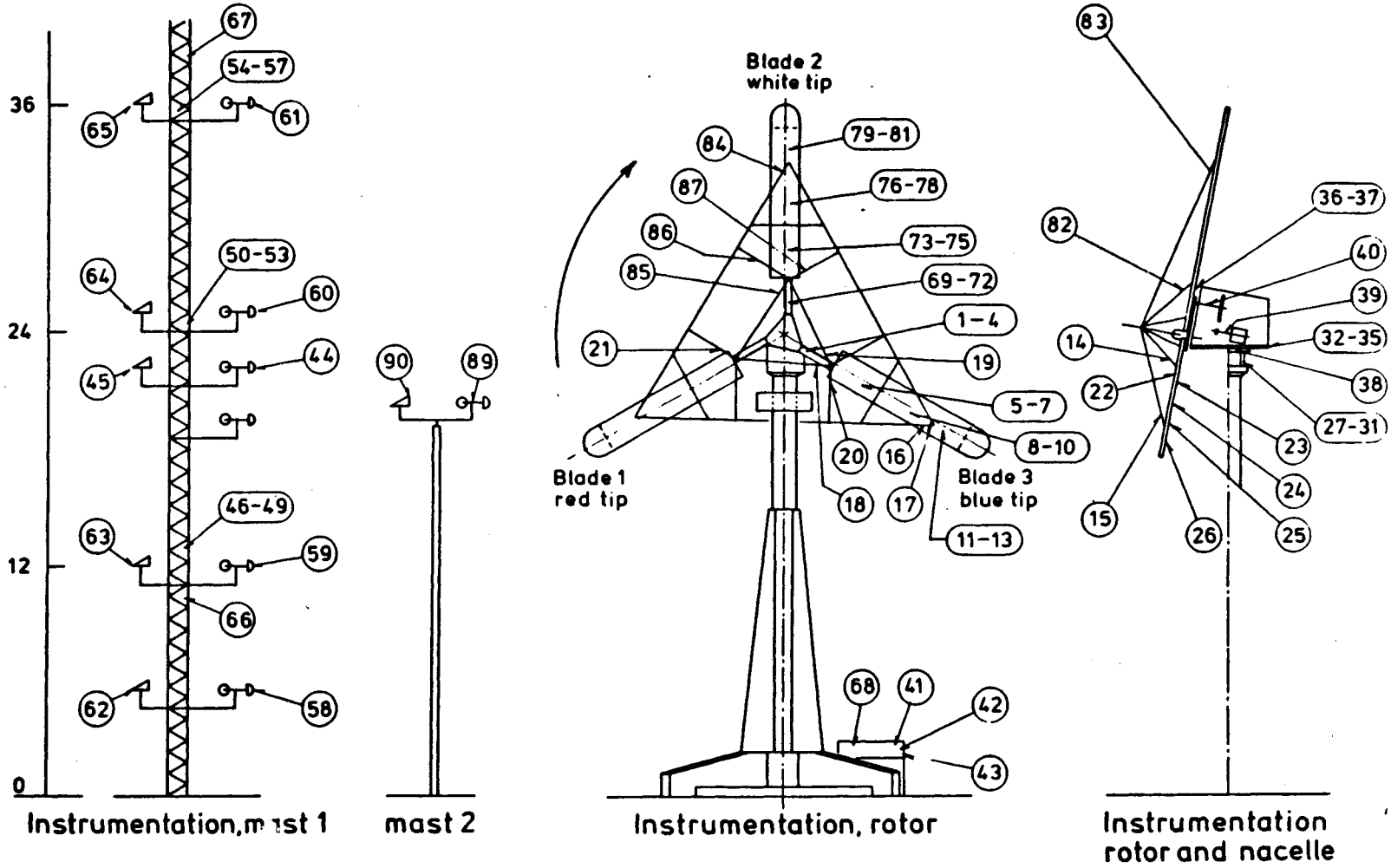

Fig. 1.4. Sensor numbers and positions.

One scan per rotor revolution is marked by a pulse from one of two rotor position sensors. This serves to synchronize the various sensor responses together. The other position sensor serves to measure rotor rotational speed. The power train is described by shaft torque, electric active power, reactive power, voltage and current.

The nacelle movements are described through two horizontal and one angular acceleration, yaw rate and nacelle azimuth position.

Forces measured between nacelle and tower are two horizontal forces and three moments.

Finally the wind field is measured with cup-anemometers and 1 wind-vane of fast responding types for the dynamical type measurements. For long-term statistics and climatology several cup-anemometers, wind-vanes and thermometers along a 40-m tower 30 m from the turbine are used.

The complete experiment can be viewed as three separate blocks: Laboratory measurements, short-term measurements and long-term measurements.

During the laboratory program, the structural characteristics of a rotor blade, Fig. 1.5, were studied through the response of the blade to simple forces. The laboratory tests were concluded at an early stage and resulted in the decision on the rotor instrumentation needed as outlinned above. It was concluded that forces and moments only in the main blade spar were sufficient for describing blade forces, as the cladding has a negligible influence. The necessary linear matrix calibration expressions were established on the basis of the simple forces.

Blade eigenfrequencies without stays were determined too. For flapwise bending the lowest frequency was 1.57 Hz. Edgewise bending 2.3-2.4 Hz.

Static calibrations of the measuring cylinder used for the nacelle-tower interface forces are described in Ref. 1.4.

The short-term measurements study the dynamical response of possibly every part of the turbine under operational conditions. A total of some 50 instruments are sampled at 50 Hz for approx. 40 mins. for each run. The 100,000 scans are stored on digital magnetic tape. A total of 17 runs have been obtained.

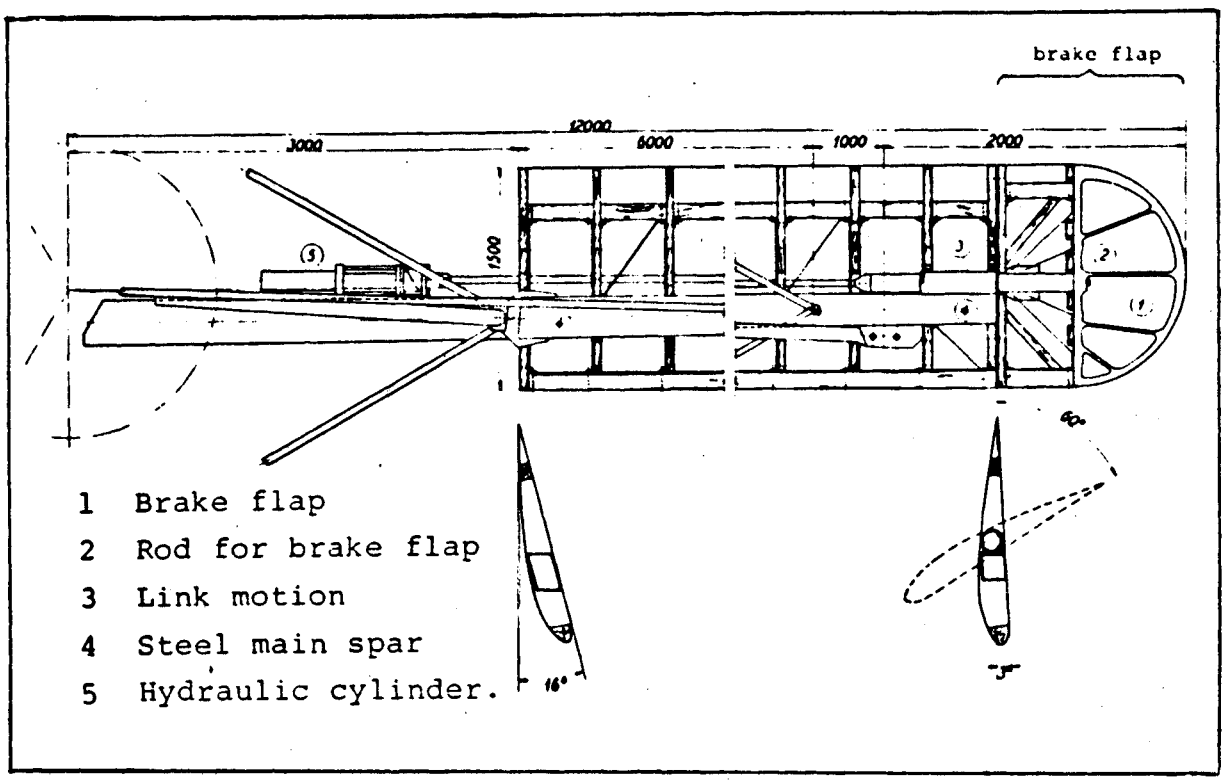

Fig. 1.5. Blade design.

A first main conclusion of this work is that the experimental set-up met with severe problems due to the extreme environment. Most major problems were solved, but occasional failures of individual measuring channels could not be avoided.

Some illustrating conclusions have been reached, coming out as a by-product of checks that mainly served to illustrate the correct function of the channels involved. The force balance as an average over several revolutions (which circumvents the rotating gravity force) on one blade has been checked, i.e. it is tested that total forces (blade root moments and forces and stay forces) balance out. This balance gives a reasonable check of the internal consistency of the data.

The edgewise moments in the blades have been checked against the power produced and against a calculated wind load distribution and reasonable agreement was found. Flapwise moments likewise agreed reasonably well with the assumed windload.

A few conclusions from these checks are: The rotor has no large aerodynamical and structural unsymmetries. Forces on the stays connecting to the blade tips are important, making the rotor a stiff structure. The stresses are generally quite low. Gyral forces are small. It is revealed that the correction of data for the static forces that are present without windload is not a simple matter.

Fourier analysis was applied to identify eigenfrequencies as well as other frequencies and the relative importance of these. Not surprisingly, most of the rotor forces are heavily dominated by the rotational frequency (0.5 Hz). Also, the measured eigenfrequencies showed good agreement with calculated frequencies for the rotor.

Plots of all measured quantities were made to check the quality of the data. Fig. 1.6 shows a sample of channels from one run. To get some rough idea of the magnitudes of the measured quantities, mean, rms, maximum and minimum values of each channel were calculated. The zero-values of the rotor channels were determined by turning the rotor slowly, averaging the reading over at elast one revolution.

A more detailed description of the measurements is found in Ref. 1.1.

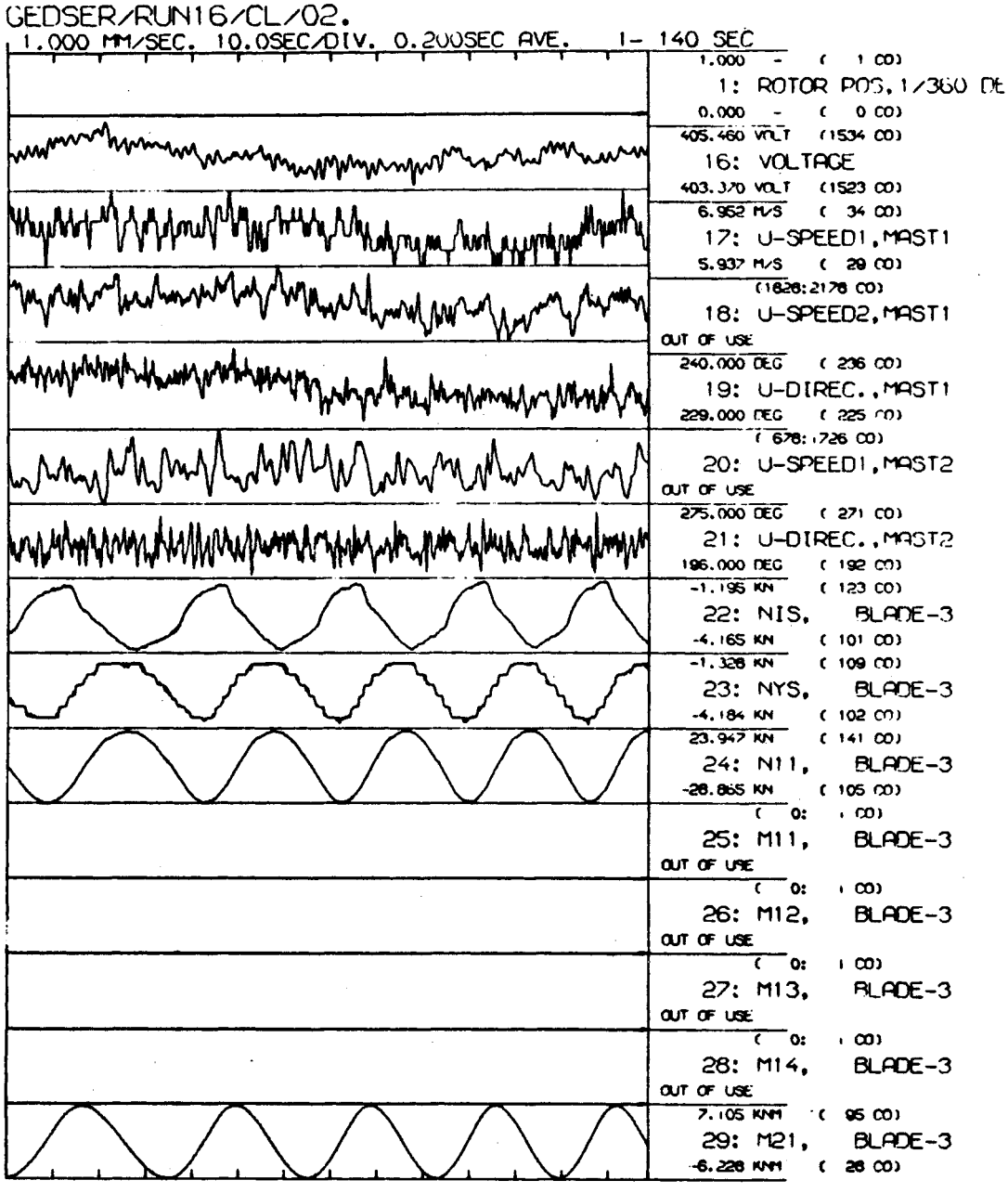

Fig. 1.6. Example of time history plot, used for data quality control, from the Gedser wind turbine.

REFERENCES

1.1. P. Lundsager, C.J. Christensen and S. Frandsen, The measurements on the Gedser Wind Mill 1977-79, Gedser test group 771.105-3, The wind power program of the Ministry of Commerce and the Electric Utilities in Denmark (Nov. 1979).

1.2. Danish Electric Utilities:
"Report from the Wind Power Committee",
(Vindkraftudvalgets Betænkning)
Union of Danish Electric Utilities. (1962) (In Danish).

1.3. Research Association of the Danish Electricity Supply Undertakings (DEFU):
"A Preliminary Test Program for the Gedser Wind Turbine".
(May 27th 1977).

1.4. Askegaard, V., Mossing, P.:
"Instrumentation and Calibration of Measuring Cylinder on Gedser Wind Turbine".
Structural Research Laboratory, Technical University of Denmark, Report S28/77 1978.

2. LONG-TERM MEASUREMENTS, POWER CURVE

Introduction

In order to gather statistics on the climatology of the site, a selected number of sensors were continuously recorded throughout the entire period of measurements. These data were recorded on a small tape recorder.

The following meteorological instruments were recorded: 3-5 cup-anemometers, 2 wind direction sensors, 2 thermometers and 1 difference thermometer. The wind speeds are averaged over 10 minutes, while the other instruments deliver instantaneous readings in volt read once each 10 minutes. All numbers are stored as binary numbers between 0 and 1023 (corresponding to a resolution of app. 0.1 per cent).

After some preliminary measuring sessions we found that valuable information could be achieved by including the electrical power output from the turbine in the climatological data acquisition system. This was done in June 1978, thus providing 10 minutes' averages of the power until the shut down of the turbine in April 1979. The recording system and the sensors are described in detail in Ref. 2.1.

Although the power production was recorded for 9 months, only app. 700 values (corresponding to 117 hours) were obtained due to various mechanical problems with the turbine as well as with the recording system. Of those 700 data points only half could be used for reasons which will be explained later.

The distance between the turbine and the meteorology tower is 35 m (the diameter of the rotor is 24 m). The relative positions

of mill and tower are shown in Fig. 2.1.

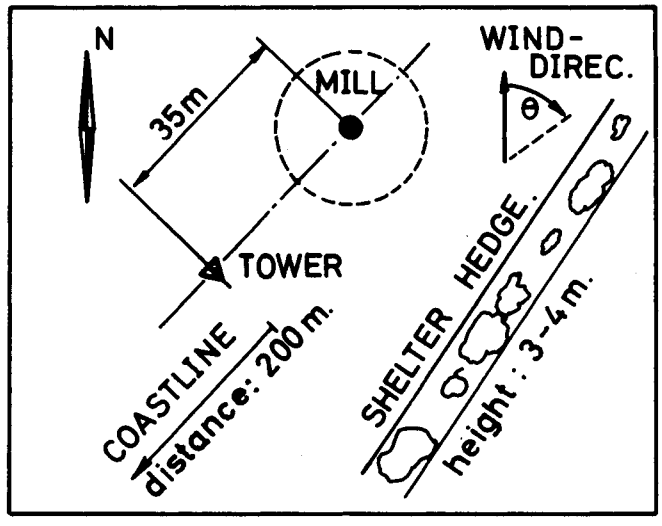

Fig. 2.1. Relative position of mill and tower.

The hedge to the S-E of the mill is not very high. Therefore it will have little impact on the air flow through the rotor. The coast line is app. 200 m S-W of the site and an earlier investigation indicated that when the wind comes from S-W, the upper half of the rotor area is actually exposed to the "open sea wind profile", while the wind profile below hub height corresponds to the surface roughness of the surrounding farmland.

The scope of the present investigation is to establish a power curve for the Gedser wind turbine in which the scatter of the measuring points is minimized. In other words, the resulting power curve should facilitate the calculation of the average production with as little uncertainty as possible. In addition we will be able to determine the power coefficient of the turbine.

Principle of averaging

The primary reason for choosing 10 minutes as the averaging period is that it is "meteorological standard". The choice implies that the turbulent fluctuations are averaged out.

Within a 10-minute period the average available power is propor-

tional to the cube of the wind speed:

$$\overline{P}_T \overset{\alpha}{\infty} \overline{(\overline{U} + u')^3} \sim \overline{U}^3 \left(1 + 3\left(\frac{\sigma_u}{\overline{U}}\right)^2\right) \qquad (2.1)$$

where $\overline{U}$ is the average wind speed, u' the fluctuating part of the longitudinal wind component and σ_u^2 the variance of U. The term $3\left(\frac{\sigma_u}{\overline{U}}\right)^2$ is of the order of 3 per cent. Therefore the use of 10-min. averaged wind speeds for calculating the power will have only a minor impact on the accuracy of the estimate of the available energy.

The influence of turbulence on the power output of the mill will be discussed in Chapters 3-4.

Climatology of the site

The long-term measurements cover the period October 1977 to April 1979. In order to weigh the different seasonally influenced weather situations correctly, it is convenient to use only one full year, here the year of 1978.

Fig. 2.2 shows the probability distribution of the wind direction, subdivided into 8 sectors, each of 45 deg. The prevailing wind directions are east and southwest to northwest.

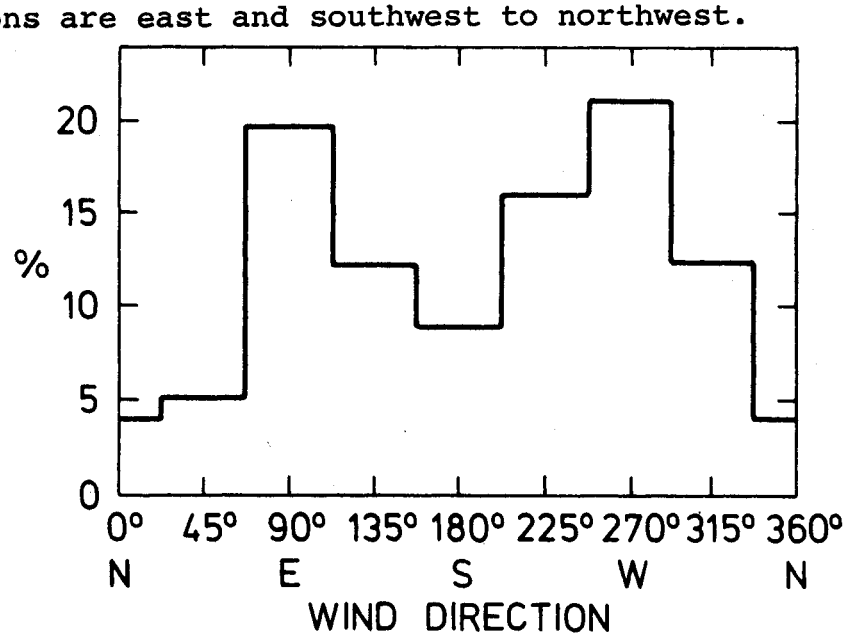

Fig. 2.2. Probability of wind directions for the year 1978 at the Gedser site.

The probability density function for wind speed measured at hub height in 1978 is shown in Fig. 2.3. The mean wind speed is calculated to be 6.3 m/s. Wind data measured at Risø during the same period are shown in the same figure. The Gedser density function has a somewhat higher average wind speed, and wind speeds higher than 8 m/s are more probable at Gedser than at Risø.

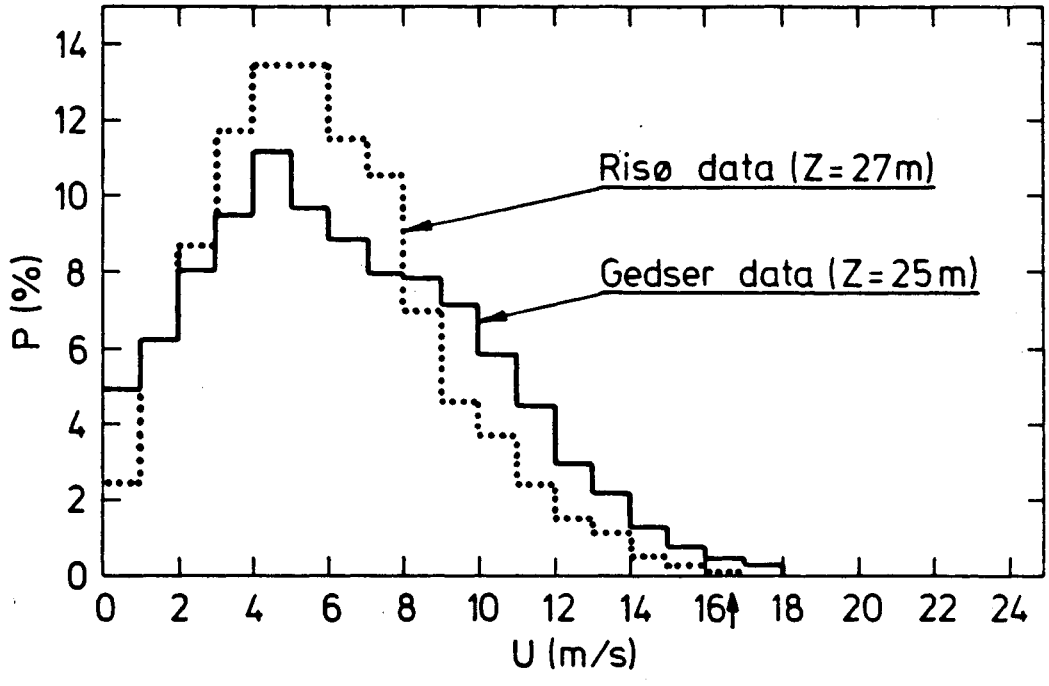

Fig. 2.3. Probability density function of wind speed at Gedser and Risø, 1978.

Using the statistics of the wind speed for Gedser, Fig. 2.3, the probability density function for the available energy within the area of the rotor can be determined, and the result is shown in Fig. 2.4. This figure shows that a maximum of wind energy is available between 10 m/s and 12 m/s, and that only a small fraction of the total energy production should be expected to be generated at wind speeds above 17 m/s. It can be shown that most of the available wind energy at the Gedser site (70%) is found at wind speeds between 8 m/s and 15 m/s. The total amount of energy is given by adding the columns in Fig. 2.4, and the total available energy current in the wind is $1.4 \cdot 10^6$ kWh/year within the rotor area.

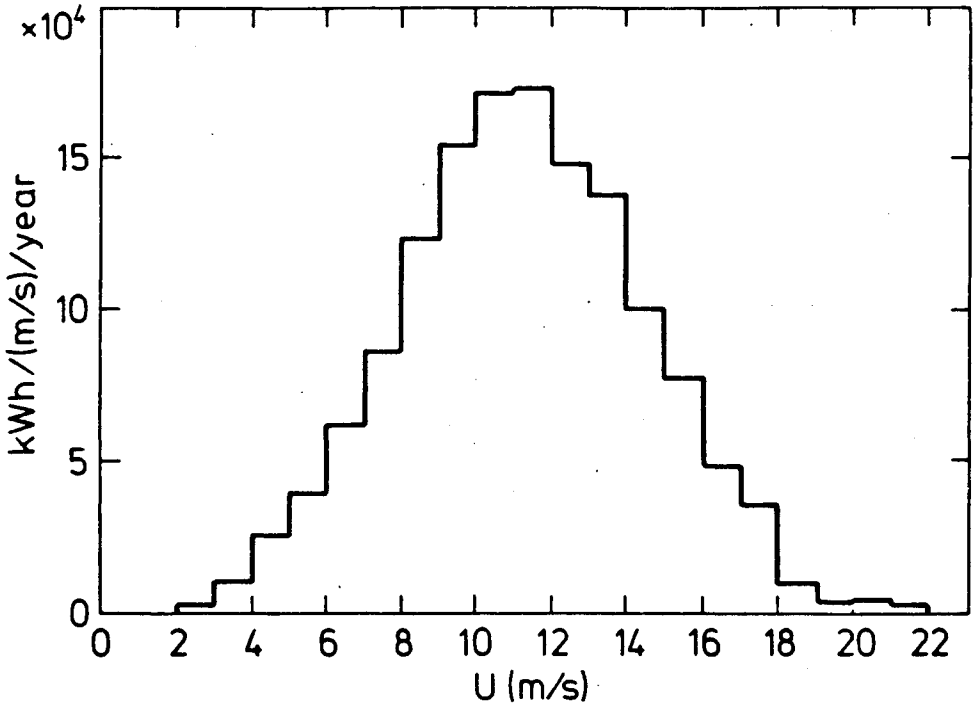

Fig. 2.4. Available energy within the rotor area at the Gedser site, 1978.

Power measurements

All available 10-min. averaged simultaneous wind speed and power measurements are shown in Fig. 2.5, where generated electric power is plotted vs. wind speed at hub height (24 m). The different signatures refer to four different wind direction sectors indicated in the figure.

Tests with skew wind was carried out during periods with wind from the sectors N-E to S-E, and the measurements from these periods cannot be used for the determination of the power curve. Measured values where $P > \frac{1}{2}\rho AU^3$ are neglected as erroneous, and so are points where the turbine was partly stopped during the averaging period. The remaining points represent wind speeds from N-W and S-W only and a power curve based on those points is shown in Fig. 2.6.

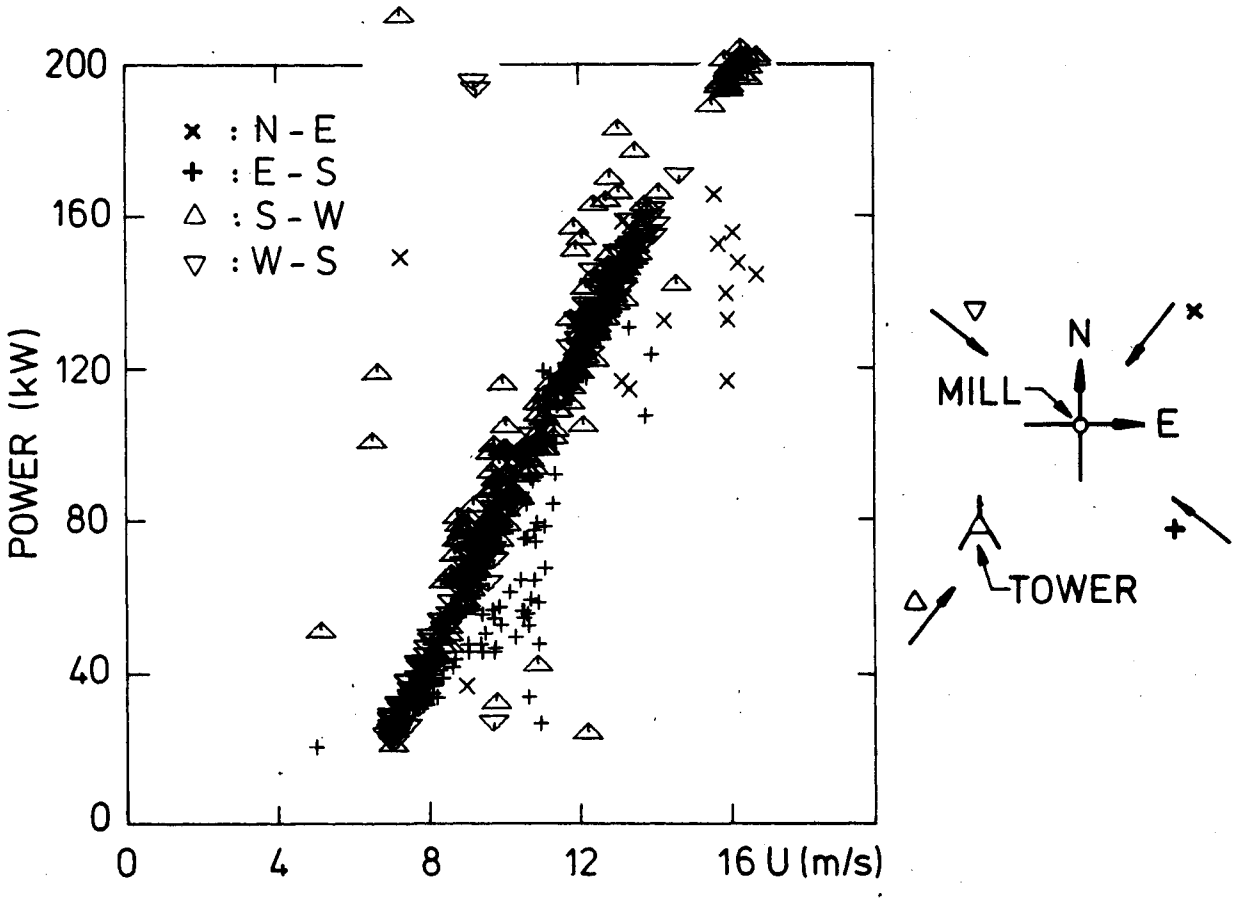

Fig. 2.5. Generated electric power as a function of wind speed at hub height (all available 10-min. averaged measurements). Wind direction is divided into four sectors indicated by different signatures.

Some points in Fig. 2.6 are significantly off the main group of points. In order to check if these points represent erroneous measurements caused by a periodic defect of the cup-anemometer, the power is also plotted vs. wind speed measured at 10 m height and 40 m height. The plots are shown in Fig. 2.7 and 2.8, and on these curves all points are uniformly grouped around the line. Therefore, points off the main group in Fig. 2.6 are probably erroneous, caused by a periodic defect of the cup-anemometer at hub height.

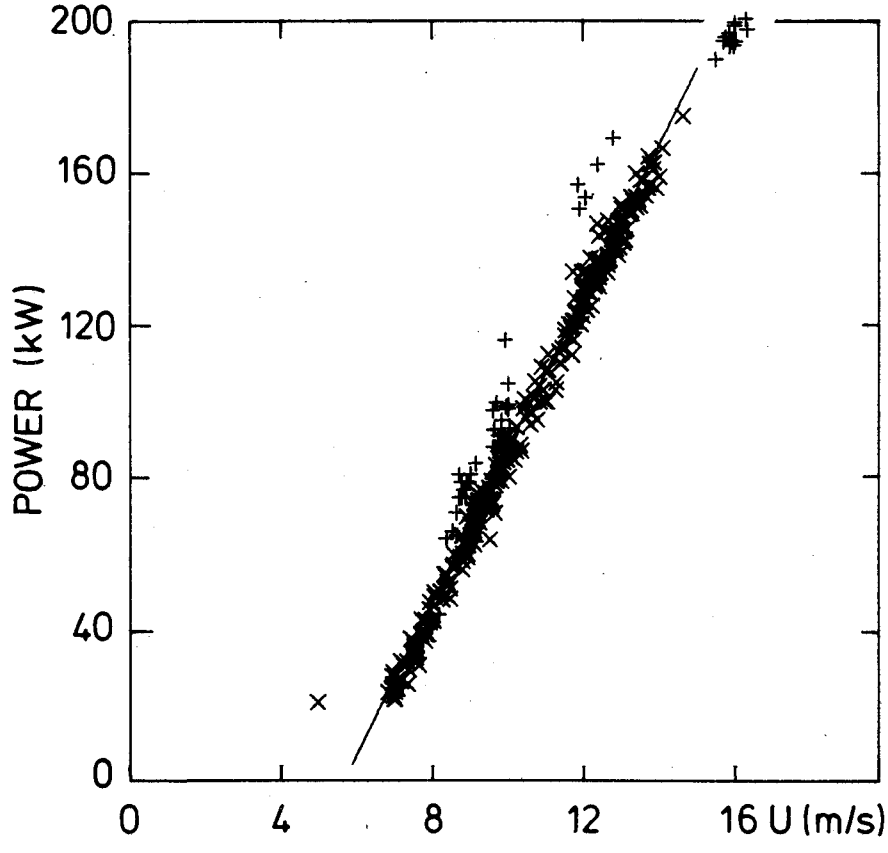

Fig. 2.6. Power curve based on the wind speed measured at hub height. Wind directions from the N-W and S-W sectors only. Correction is made for temperature variations.

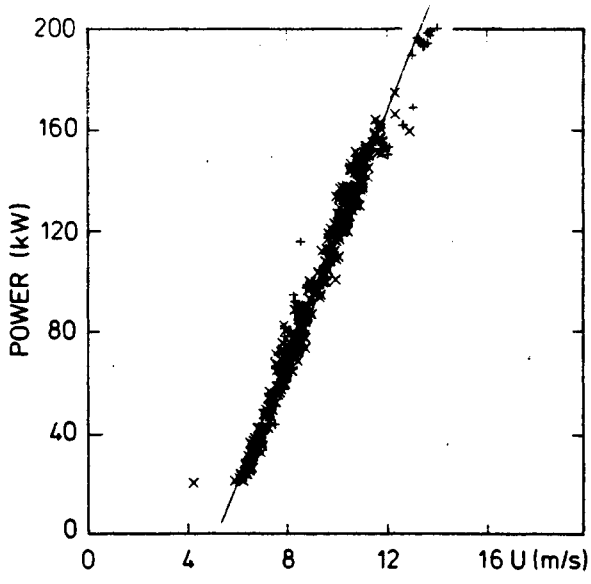

Fig. 2.7. Power curve based on measured wind speed at 10 m height.

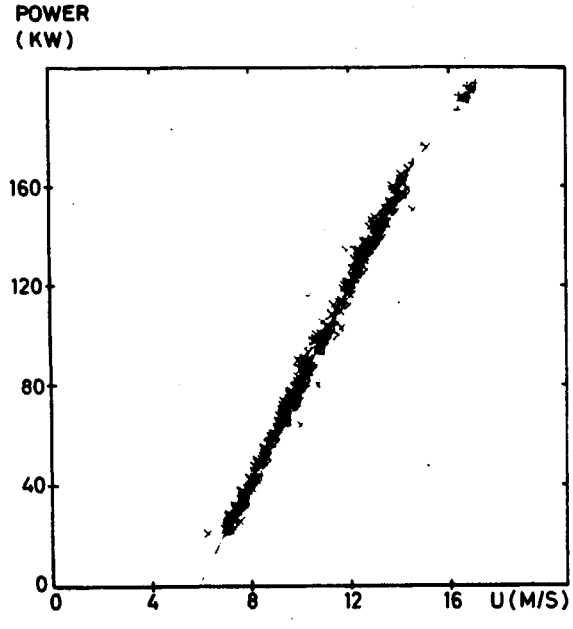

Fig. 2.8. Power curve based on measured windspeed at 40 m height.

The scatter in the power curve plots

The wind energy flow through the total rotor area (A) and thus the power production of the turbine depends on the wind speed distribution over the area A. One could assume

$$P \overset{\alpha}{\sim} \int_A U^3 dA \ .$$

It is obviously desirable to avoid measuring the area distribution, but rather to use just one point measurement. Both the power curve obtained and the scatter in the power curve plot, however, depend critically on the point chosen. A few examples of this difficulty are shown in the following, using the 10-min. average data available.

The scatter in the power curve plot is defined as the root mean square distance along the power axis from the experimental points to the line that minimizes this RMS

$$RMS = \sqrt{\frac{\Sigma (p_i - (\alpha U_i + \beta))^2}{N}}$$

where p_i and U_i are the measured electric power and the measured wind speed, respectively. $\alpha U+\beta$ is the regression line resulting from minimizing RMS.

Based on the plots in Figs. 2.6-2.8 the RMS values (the scatter) were calculated with the results

Anemometer height	RMS
10 m	7.14 kW
24 m	6.71 kW
40 m	4.40 kW

The wind speed on different parts of the rotor varies more or less independently of each other because of the small scale nature of turbulence. The extended rotor integrates the fluctuations over the rotor area. Therefore, one would expect that the

average wind speed seen by several anemometers could be a better representation of the area integration of wind speed that defines the power production. Fig. 2.9 shows an example where the average of the 10 m and 40 m cup-anemometers was used together with

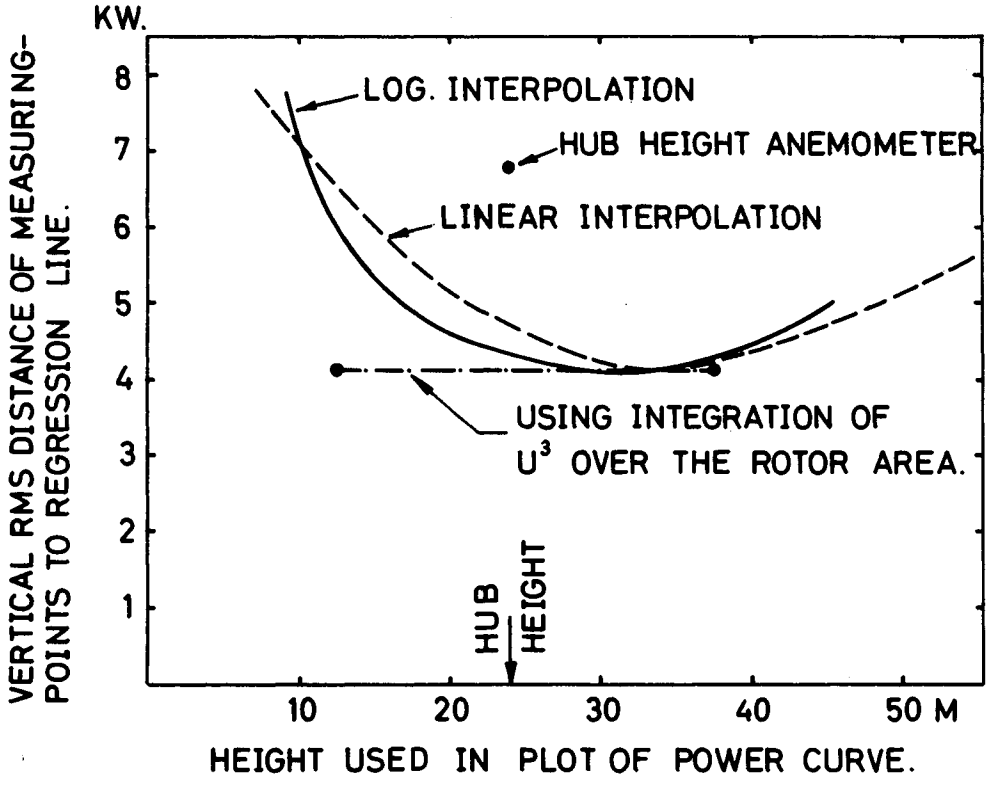

Fig. 2.9. Scatter of power curves as a function of the height, where wind speed is measured.

power. The resulting wind speed at various heights was calculated by interpolation between the two anemometers. Two wind profile shapes were tried (logarithmic and linear). In the same figure the point on the axis at 4.2 kW is the scatter when $\bar{U}$ is used representing a simplified area integration over the rotor area as described in the following section (p. 26). The equivalent height used as the abscissa of Fig. 2.9 defines the weighting between the fluctuations in the two heights. Minimum scatter is obtained at around 30 m height. It is also shown that the RMS value is distinctly higher when using the hub height anemometer than when using the two-anemometer interpolation. This difference is to be expected, but it could, however, be partly due to periodical errors in the hub height anemometer.

Power coefficient

The power coefficient of a wind turbine is defined as the ratio between power output from the rotor and the available wind power within the rotor area as a function of wind speed. It is not obvious that the hub height wind speed is the correct value to use when approximating $P = \int_A U^3 dA$ with $\bar{U}^3 A$ for constructing the power curve. $\bar{U}$ varies considerably with height. In Fig. 2.10 the maximum wind speed variation (rotor top-bottom) relative to the hub height wind speed is shown as a function of turbine

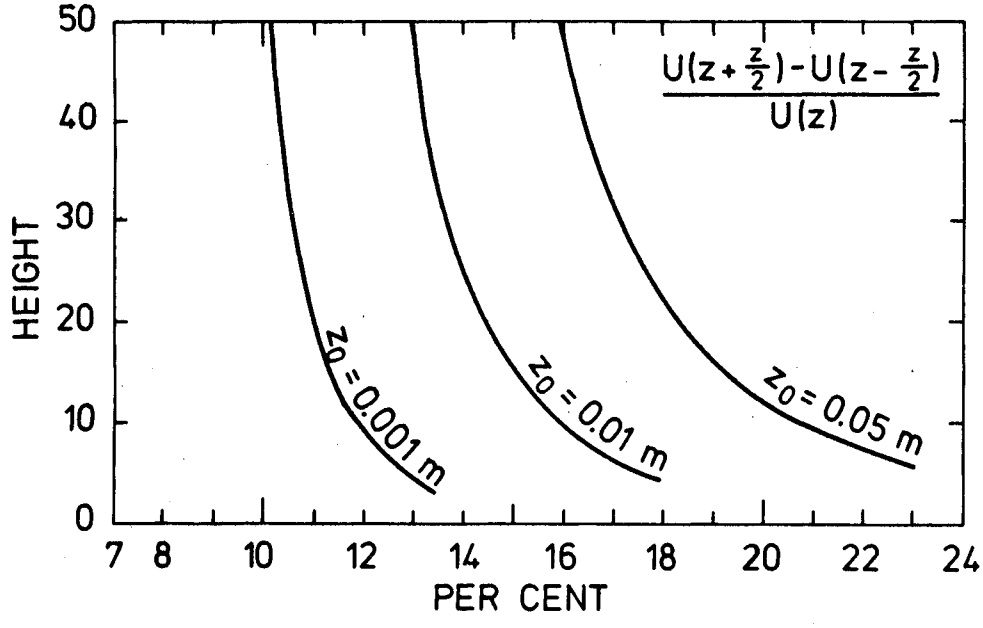

Fig. 2.10. Vertical variation of wind speed across rotor area for different hub heights and different types of terrain.

size (rotor diameter = hub height) for various landscapes as characterized by the roughness length z_o. A logarithmic profile

$$u(z) \propto \log(z/z_o) \qquad (2.2)$$

was assumed. For the Gedser turbine this maximum span is ~ 18%. z_o = 0.05 cm is the typical land roughness at the Gedser site, whereas z_o = 0.001 m is typical for water.

Assuming a linear wind profile between 10 m and 24 m, and between 24 m and 40 m, the wind power flow within the rotor area is found to be proportional to

$$P \sim U_N^3 \left\{1 + \frac{2}{\pi}(P_2-P_1) + \frac{3}{8}(P_2^2+P_1^2) + \frac{4}{15\pi}(P_2^3-P_1^3)\right\} \qquad (2.3)$$

where

$$P_1 = a_1 \frac{R}{U_N} \quad \text{and} \quad P_2 = a_2 \frac{R}{U_N} \qquad (2.4)$$

and where U_N is the wind speed at hub height. a_1 and a_2 are the slopes of the linear wind speed variation between 10 m and 24 m, and 24 m and 40 m. R is the radius of the rotor. In this case, the values of P_1 and P_2 in Eq.(2.3) are P_1 = 0.112 and P_2 = 0.066, and it is found that

$$\int_A U^3 dA = U_N^3(1-0.02) \ . \qquad (2.5)$$

This result means that the wind energy flow within the rotor area based on wind speed at hub height differs only little (+2%) from the energy flow based on $\int_A U^3 dA$.

The power coefficient curve based on the generated electric power and the wind speed measured at hub height for the Gedser mill is shown in Fig. 2.11, together with two predictions.

The measured power coefficient curve, derived by means of linear regression on the power curve, is compared with two estimated curves, which are described in Ref.2.2 and Ref.2.3. The calculated c_p-curves are greater than the measured values within the range of wind speeds of importance by ~ 30%. The maximum power coefficient is found at the same wind speed, 9 m/s, for the measured curve and for the estimated curves.

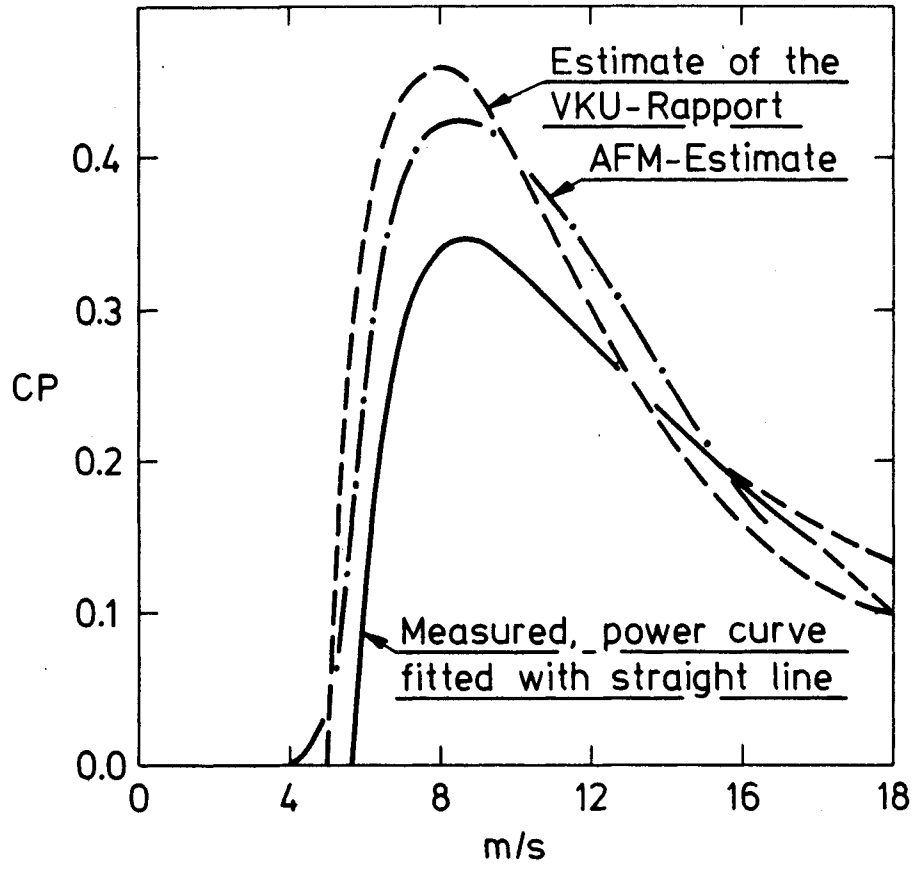

Fig. 2.11. Estimated and measured power coefficient curves for the Gedser wind mill.

In Fig. 2.12 the measured c_p-curve is shown. Each power measurement is divided by $\frac{1}{2}\rho U^3 \cdot A_R$, using the hub height wind speed, which is calculated by log. interpolation between the wind speed at 10 and 40 m height. The maximum c_p-value is 0.35 at a wind speed of 9.0 m/s.

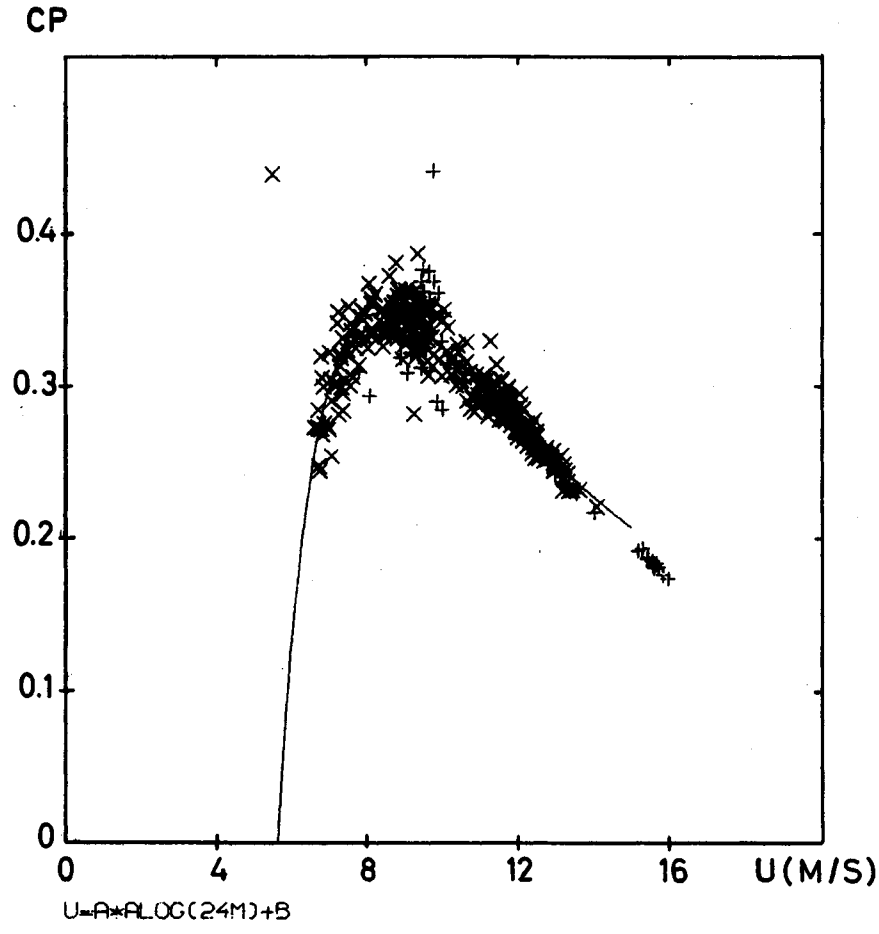

Fig. 2.12. Power coefficient curve measured (calculation from 10 and 40 anemometer).

Power production

As shown above, the wind speed at hub height is representative for the wind power flow through the rotor area, and using the statistics of the wind speed at hub height for 1978 and the power curve shown in Fig. 2.6, the power production during 1978 can be calculated after the Eq.

$$E = \int_{U_1}^{U_2} P(u) \cdot T \cdot f(U) du \qquad (2.6)$$

where P(u) is the fitted power curve, T is hours per year and f(U) is the probability distribution of the wind speed at hub height shown in Fig. 2.3. U_1 and U_2 limit the range of wind speeds, where the turbine is in operation. The 1978-production estimated by this method is app. 350,000 kWh, which is close to the production recorded during the years of regular operation, Ref.2.2. The mean power coefficient for the mill for 1978 was 0.24.

Conclusions

The main conclusions on the long-term measurements of wind speed and electric power are:

- The power curve for the Gedser wind turbine is close to being linear in a wide range of wind speeds. The use of 10-min. averages to a large extent eliminates the scatter in the measured data. The determination of the power coefficient is much dependent on the height at which the reference wind speed is measured. However, simple considerations seem to indicate that the hub height wind speed is a proper reference.

- The power curve for the Gedser turbine is app. linear and given by the form:

  $P(u) = 0$

  $P(u) = 20.20(U-5.75)$ kW for 5.75 m/s $< U <$ 15 m/s

  $P(u) = 200$ kW for $15 < U$

  where U is the 10-minute averaged wind speed at hub height. The maximum power coefficient of the mill is 0.34 at a wind speed of 9.0 m/s.

- The power production for an annual mean wind speed of 6.3 m/s at hub height is app. 350,000 kWh and the turbine will produce power app. 50 per cent of the time.

REFERENCES

2.1. P. Lundsager, C.J. Christensen and S. Frandsen, The measurements on the Gedser Wind Mill 1977-79, Gedser test group 771.105-3, The wind power program of the Ministry of Commerce and the Electric Utilities in Denmark (Nov. 1979).

2.2. Danish Electric Utilities: "Report from the Wind Power Committee", (Vindkraftudvalgets Betænkning), Union of Danish Electric Utilities. (1962) (In Danish).

2.3. K.S. Hansen, Theoretic calculation of power and blade loads on the Gedser Mill, (Teoretisk beregning af effekt og bladbelastning for Gedsermøllen, Notat VG-01-790312, AFM, DtH. (In Danish).

3. SHORT-TERM POWER MEASUREMENTS

Atmospheric turbulence and wind turbines

In a simplified description of turbulence one can visualize a steady air flow with a velocity $\overline{U}$ (average wind speed) with eddies of different sizes embedded, floating along with the air (so-called "frozen turbulence"). Assume that a cup-anemometer is located at a distance D upstream of the turbine. A large eddy will cause a slow fluctuation usually experienced both by the wind sensor and by the total rotor area. The resulting fluctuations are called coherent. A small eddy (fast, high frequency fluctuation) will be seen first by the wind sensor, but later by a time $D/\overline{U}$ by only a part of the rotor plane. It may either miss the wind sensor but hit part of the rotor (or vice versa), or it may die out before reaching the rotor. In this case the wind speed and the power output have low coherence which gives rise to scatter in the power curve plots. These effects are discussed in the following sections. The eddies themselves cause load and power fluctuations, which will be discussed in Chapter 4 from a statistical point of view. In Chapter 4 the wind sensor is used for measuring a general, statistical character of the wind field rather than a deterministic connection between the wind speed and the wind turbine response.

Power curve scatter. Timing of wind and power signal

We often thinkof a wind turbine power curve as the connection between the electric power output P and the velocity U of a steady, uniform (laminar) air flow that drives the turbine. This is an oversimplified view, as nature almost never supplies a completely smooth flow.

When studying the effects of low coherence, Fourier analysis is a powerful tool. The discussion of frozen turbulence above in-

dicated that a disturbance would show up at time $D/\bar{U}$ later at the rotor than at the anemometer. In a frequency analysis this delay transforms into a phase lag. Assume that the eddies which produce velocity peaks are a distance λ apart. As the eddies are drifting from the anemometer to the turbine with a velocity $\bar{U}$, they will be seen by the anemometer separated in time by $T = \lambda/\bar{U}$, and likewise by the rotor. They will be delayed by $\Delta t = D/\bar{U}$ between sensor and rotor. This is readily converted into a phase difference

$$\phi = 2\pi \Delta t/T = 2\pi Dn/\bar{U}$$

where $n = 1/T$ is the frequency of the disturbance. This effect is illustrated in Fig. 3.1 from a cross spectral Fourier analysis of a run with the Gedser turbine. Fig. 3.1b shows the resulting phase difference between the wind and the power signals. The calculated phase using the above expression is also shown. The measured and calculated values fit well up to 0.2 Hz. Above 0.2 Hz coherence has dropped off as illustrated in Fig. 3.1a. Therefore the fluctuations in the wind velocity and the power have little to do with each other and the phase difference is consequently poorly determined. In Fig. 3.1c the wind velocity was delayed by $D/\bar{U}$ (= 2.4 secs, D = 30 m, $\bar{U}$ = 12.5 m/s) before the Fourier analysis. This delay removes the phase change and should also be used when measuring short time averaged power curves.

Power curve scatter. Low coherence

The low coherence between fast fluctuations that was illustrated in Fig. 3.1a will lead to scatter in the power curve plots. This connection between low coherence and scatter will be discussed in the following in order to illustrate the influence of time averaging.

We will assume that the correct time delay $D/\bar{U}$ has been applied to U(t). Furthermore, we will use time averaged values of U and P:

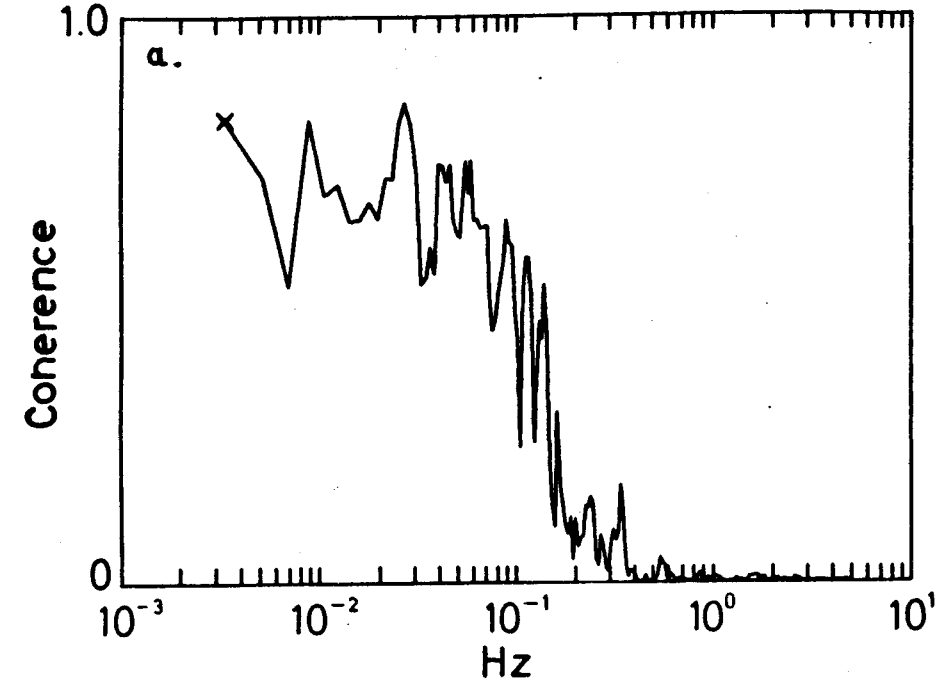

Fig. 3.1. Cross spectral analysis of wind speed versus power for a Gedser run of 1800 sec recording time, a) coherence, b) phase lag power - wind speed, c) like b), but wind signal delayed by $D/\overline{U}$ secs.

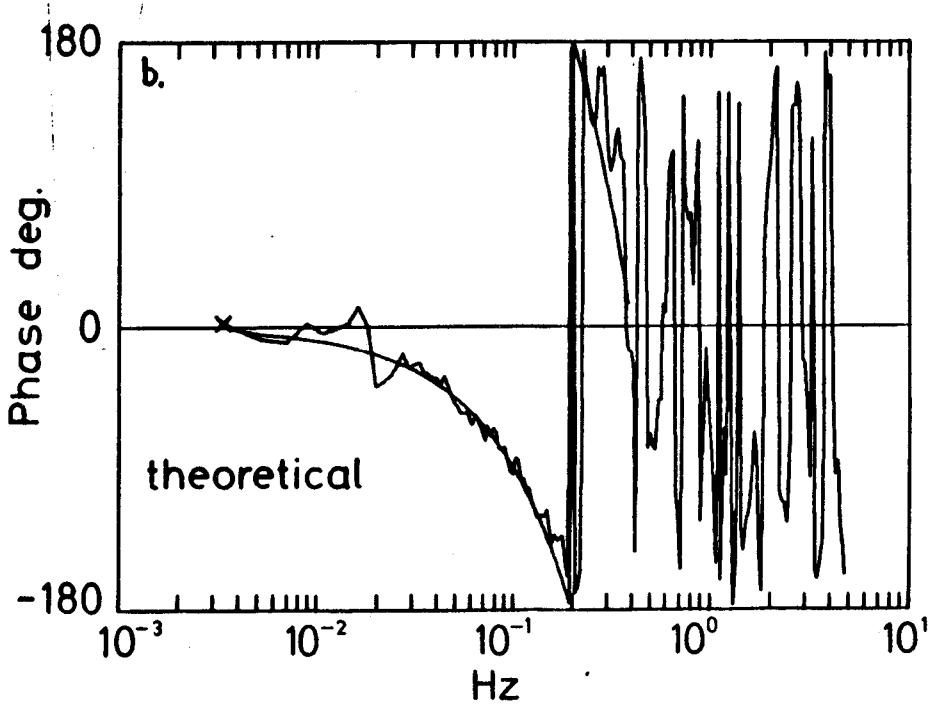

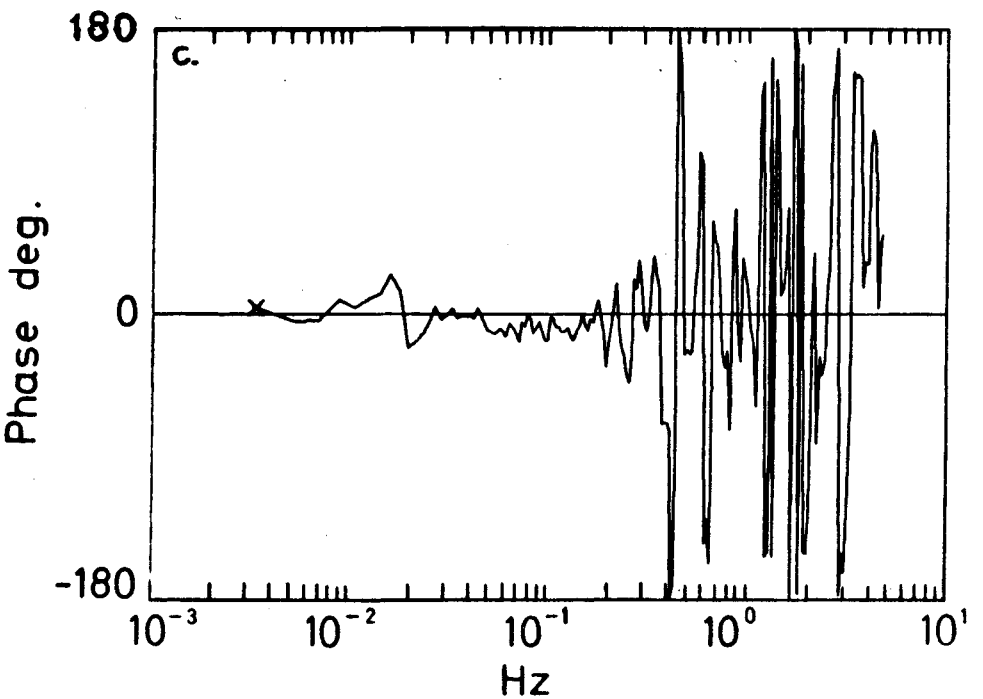

$$U = \frac{1}{\tau}\int_{t}^{t+\tau} U(t')dt' \; ; \quad P = \frac{1}{\tau}\int_{t}^{t+\tau} P(t')dt' \tag{3.1}$$

The averaging time chosen when plotting simultaneous time averaged U and P values has a strong influence on the scatter in the resulting (U,P) diagram as illustrated in Figs. 3.2a and b. The scatter will be compared to a cross spectral analysis in the following in order to elucidate the influence of averaging time on the scatter.

The analysis will be limited to linear processes. This is a serious limitation, but the analysis still allows us to gain insight into the influence of turbulence on power curve scatter. When fitting a series of (U,P)-points to a straight line, one minimizes the rms-distance to the best line. But the distance can be defined in various ways. One can take distance parallel to either of the U and P axes. Or one can take distance perpendicular to the line sought. These three definitions are illustrated in Fig. 3.2a.

If we assume that U(t) and P(t) are two correlated Gaussian random functions, the resulting two-dimensional (U,P) probability distribution will have elliptical isoprobability curves as also sketched in Fig. 3.2a.

Two new variables (X,Y) can be defined:

$$X = a(U-\overline{U})\cos\theta + b(P-\overline{P})\sin\theta \tag{3.2}$$

$$Y = -a(U-\overline{U})\sin\theta + b(P-\overline{P})\cos\theta \tag{3.3}$$

An overbar (like in $\overline{U}$, $\overline{P}$) signifies the average of all the τ-averaged measurements and

$$\mathrm{tg}2\theta = \frac{2\overline{(U-\overline{U})(P-\overline{P})}ab}{a^2\overline{(U-\overline{U})^2} - b^2\overline{(P-\overline{P})^2}} \tag{3.4}$$

a and b are the scales chosen for the (U,P) plot in cm sec/m and cm/kW, respectively.

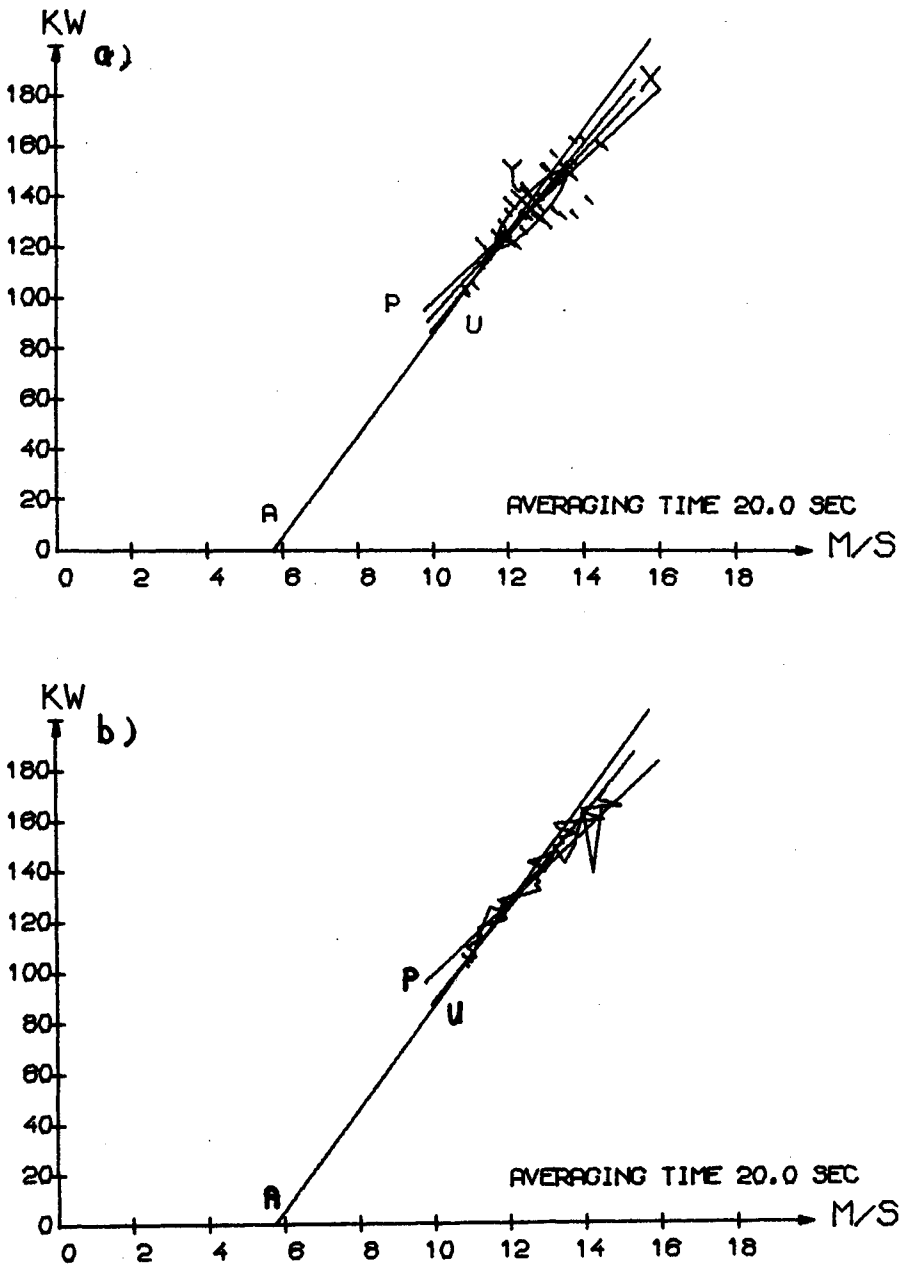

Fig. 3.2. Example of time averaged power vs. wind speed measurements and results of various statistical analyses. a) A is the 10-min. average power curve of section 2. P and U are linear regression fits using the method of bins with the uncertainty associated with power (P) or wind speed (U), respectively. The X and Y main axes in the correlation ellipse is also shown. b) The direct results of methods of bins (P and U) together with the fitted linear regression lines.

The definition, Eqs. 3.2-4, of X and Y is chosen, as

$$\overline{XY} = (\overline{(P-\bar{P})^2} - \overline{(U-\bar{U})^2}) \cdot \frac{1}{2} \sin 2\theta + \overline{(U-\bar{U})(P-\bar{P})} \cos 2\theta = 0 \tag{3.5}$$

As $\overline{XY}$ is zero, it is easy to show that the X-axis thus defined is the line that minimizes the root-mean-square distance from the (U,P)-points perpendicular to the line itself. As U and P were assumed to be Gaussian, so X and Y will be Gaussian. As $\overline{XY} = 0$, X and Y will be both uncorrelated and independent of each other.

It is therefore natural to interpret X and Y as follows:

X represents fully coherent variations of U and P along the deterministic function P = P(U).

Y represents incoherent disturbances in U or P perpendicular to the P = P(U) inducing scatter around the true power curve.

In order to simplify the formulas in this chapter, it is practical to realise that the statistical arguments are really of a geometrical nature referring to a (U,P)-plot. Thus instead of using the wind velocity and power (U and P) it is practical to express these parameters in units of cm as plotted on the (U-P)-plot, i.e.

$$u = a(U-\bar{U}) \quad , \quad p = b(P-\bar{P})$$

Using these definitions, Eqs. 3.2-4 simplify to

$$X = u \cos\theta + p \sin\theta \tag{3.2a}$$

$$Y = -u \sin\theta + p \cos\theta \tag{3.3a}$$

$$\operatorname{tg} 2\theta = \frac{2\overline{up}}{\overline{u^2} - \overline{p^2}} \tag{3.4a}$$

To gain insight into the nature of the X and Y variations, we

will look at the scatter problem in the frequency domain by means of Fourier transformation. The averages involved in Eq. 3.4 for the transformation angle θ can be evaluated as follows:

$$\rho\sigma_u\sigma_p \equiv \overline{(U-\bar{U})(P-\bar{P})} = \overline{up} \simeq \frac{1}{\tau^2} < \int_t^{t+\tau} u(t')dt' \int_t^{t+\tau} p(t")dt" > \tag{3.6}$$

Here the time averaging over τ secs from Eq. 3.1 has been introduced. Furthermore, we assume that the number of (u,p) sets is large enough, that the averaging over many points can be approximately treated as ensemble averages (indicated by <>). Then

$$\rho\sigma_u\sigma_p = \frac{1}{\tau^2} \int_t^{t+\tau} dt' \int_t^{t+\tau} dt" <u(t')p(t")> \tag{3.7}$$

as t' and t" are independent and as the order of ensemble averaging and time integration can be exchanged. By definition

$$<u(t')p(t")> \equiv R_{up}(t'-t") = \int_{-\infty}^{+\infty} e^{i\omega(t'-t")} S_{up}(\omega)d\omega \tag{3.8}$$

where R_{up} and S_{up} are the cross covariance and the cross spectrum, respectively. Introducing this in Eq. 3.7 and exchanging the order of ω- and t -integrations, we get

$$\rho\sigma_u\sigma_p = \int_{-\infty}^{+\infty} S_{up}(\omega)F(\omega,\tau)d\omega \tag{3.9}$$

with

$$F(\omega,\tau) = \frac{1}{\tau^2} \int_t^{t+\tau} dt' \int_t^{t+\tau} dt" e^{i\omega(t'-t")} \tag{3.10}$$

$F(\omega,\tau)$ is a frequency filter due to the averaging over the time τ. It is evaluated simply as:

$$F(\omega,\tau) = \frac{1}{\tau^2} \int_t^{t+\tau} dt' \int_t^{t+\tau} dt" e^{i\omega(t'-t")}$$

$$= \frac{1}{\tau^2} \int_{-\tau/2}^{+\tau/2} dt' \int_{-\tau/2}^{+\tau/2} dt" e^{i\omega(t'-t")}$$

$$= \frac{1}{\tau^2} \int_{-\tau/2}^{+\tau/2} dt' \, \frac{2}{\omega} \sin(\tfrac{\omega\tau}{2}) e^{i\omega t'} = \frac{\sin^2(\frac{\omega\tau}{2})}{(\frac{\omega\tau}{2})^2} \qquad (3.11)$$

Eqs. 3.9-10 can be reduced further to

$$\rho\sigma_u\sigma_p = 2 \int_o^\infty Co_{up}(\omega) \, \frac{\sin^2(\frac{\omega\tau}{2})}{(\frac{\omega\tau}{2})^2} \, d\omega \qquad (3.12)$$

as $S_{up}(-\omega) = Co_{up}(\omega) + iQ_{up}(\omega) = S^*_{up}(\omega)$ where $Co(\omega)$ and $Q(\omega)$ denote Co- and Quadrature spectra, respectively.

Through similar calculations, the remaining averages of Eq. 3.4 can be evaluated with the results

$$\rho\sigma_u\sigma_p = \overline{up} \simeq 2 \int_o^\infty Co_{up}(\omega) F(\omega,\tau) d\omega \qquad (3.13)$$

$$\sigma_u^2 = \overline{u^2} \simeq 2 \int_o^\infty S_u(\omega) F(\omega,\tau) d\omega \qquad (3.14)$$

$$\sigma_p^2 = \overline{p^2} \simeq 2 \int_o^\infty S_p(\omega) F(\omega,\tau) d\omega \qquad (3.15)$$

$$F(\omega,\tau) = \frac{\sin^2(\frac{\omega\tau}{2})}{(\frac{\omega\tau}{2})^2} \qquad (3.16)$$

In the evaluation so far we have assumed that $\overline{U} = \langle U \rangle$, i.e. that we obtain the ensemble average during a limited (T secs) run. This is not the case. It can be shown, however, that this weakness can be removed by taking into account the uncertainty in $\overline{U}$ and that the only influence on Eqs. 3.13-16 is a modification of 3.16 to

$$F(\omega,\tau,T) \equiv F(\omega,\tau) - F(\omega,T) \qquad (3.16a)$$

meaning that besides the high frequency cut-off at frequency $\sim 2\overline{u}/\tau$ is supplemented with a low frequency cut-off at $\sim 2\pi/T$, i.e. determined by the total measuring time T.

The correlation coefficient ρ used above is defined according to usual statistical practice. Using the derived Eqs. 3.13-16 we get

$$\rho = \left(\int_o^\infty Co_{up} F d\omega\right) / \left(\int_o^\infty S_u F d\omega \int_o^\infty S_p F d\omega\right)^{\frac{1}{2}} \tag{3.17}$$

σ_y can be found in the following manner

$$\sigma_y^2 = \overline{(-u \sin\theta + p \cos\theta)^2} = \overline{u^2} \sin^2\theta + \overline{p^2} \cos^2\theta - \overline{up} \sin^2\theta$$

which through simple trigonometric manipulations using Eqs. 3.4, 3.13-16 reduces to

$$\sigma_y^2 = \frac{\sigma_u^2+\sigma_p^2}{2} - \sqrt{\frac{(\sigma_u^2-\sigma_p^2)^2}{4} + (\rho\sigma_u\sigma_p)^2} \tag{3.18}$$

$$\sigma_x^2 = \frac{\sigma_u^2+\sigma_p^2}{2} + \sqrt{\frac{(\sigma_u^2-\sigma_p^2)}{4} + (\rho\sigma_u\sigma_p)^2} \tag{3.19}$$

σ_x was found in a similar manner. If the scales a and b are chosen such that $\sigma_u^2 = \sigma_p^2$, these expressions reduce further to ($\phi_o = 45^o$)

$$\sigma_x^2 = \sigma_u^2(1+\rho) \tag{3.20}$$

$$\sigma_y^2 = \sigma_u^2(1-\rho) \tag{3.21}$$

$$\frac{\sigma_y}{\sigma_x} = \sqrt{\frac{1-\rho}{1+\rho}} \tag{3.22}$$

As Y was interpreted as the incoherent variations of (u,p) perpendicular to the power curve, σ_y is a suitable measure of the width of the (u,p)-point plot. Eqs. 3.13-16 and 3.18 thus allow us to calculate the scatter from a spectral analysis. This elucidates the question of the effect of averaging time τ. The filter F (Eq. 3.9) has a sharp high frequency cut-off with the cut-off frequency inversely proportional to τ. In Fig. 3.3 a wind spectrum is shown together with the Co-spectrum. Eqs. 3.17 and 3.21 show that σ_y^2 is the area between the two spectra. Choos-

ing larger τ, one chops off this area from the high frequency ens, thus decreasing the difference area and thus σ_y.

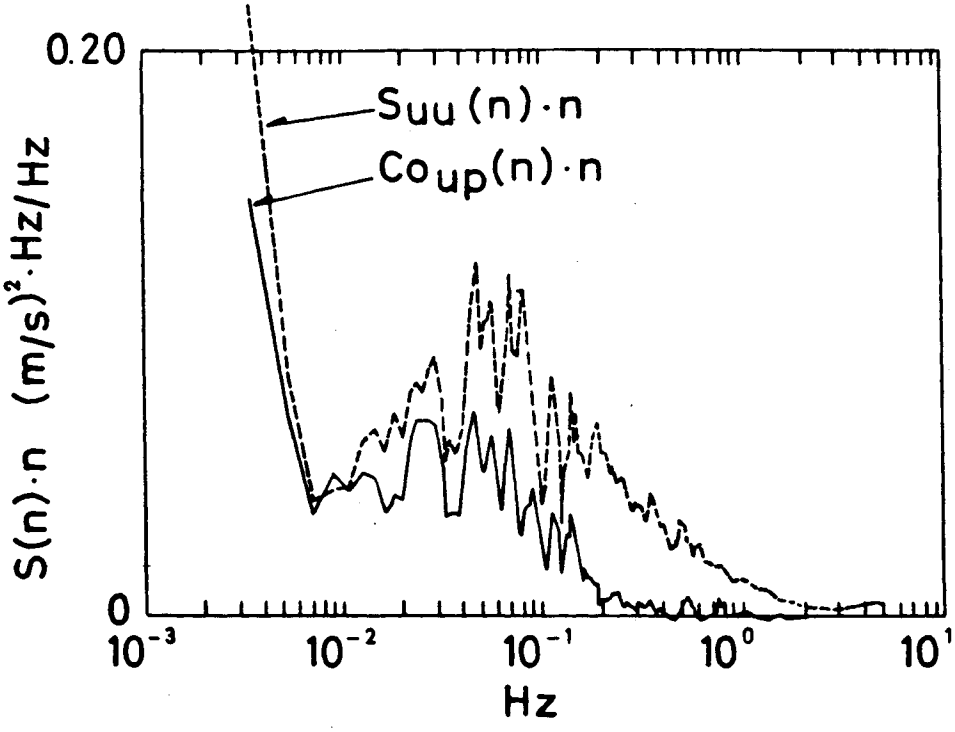

Fig. 3.3. Measured wind spectrum and Co-spectrum between wind speed and power for the data also used in Figs. 3.1-2.

This interpretation is illustrated in the simplified Fig. 3.4. Here a theoretical (Kaimal) spectrum (Ref. 3.1) is shown together with the Co-spectrum. The hatched area is equal to $\sigma_u^2(1-\rho)$. S_uF shows the effect of time averaging on the spectrum. If the averaging time is chosen longer, S_uF will move to the left, chopping off the $\sigma_u^2(1-\rho)$ area, thus decreasing σ_y-scatter.

Table 3.1.

	σ_u	σ_p	σ_x	σ_y	ϕ	σ_y/σ_x
Spectrum analysis	1.06	0.84	1.32	0.31	37.8°	4.2
Scatter in $(\overline{u},\overline{P})$-plot	1.02	0.82	1.27	0.34	37.7°	3.7

In Table 3.1, the results of the scatter calculations are compared with corresponding results derived from spectrum analysis both using experimental data from the same run.

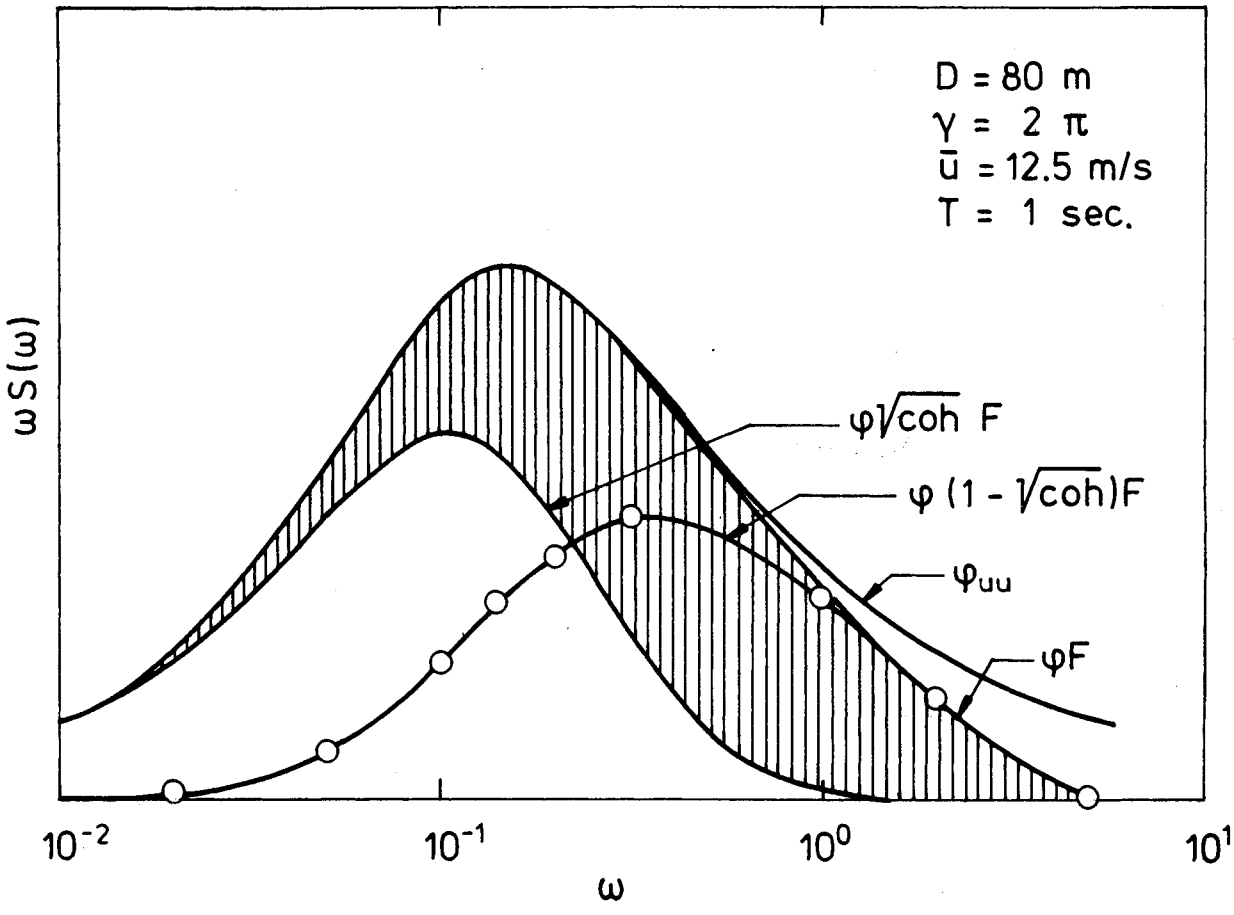

Fig. 3.4. Simplified version of Fig. 3.3. The theoretical wind speed (Kaimal) spectrum $S_n(\omega)$ is shown together with theoretical Co-spectrum using coh = $\exp(-\gamma D\omega/\bar{u})$. $S_n \cdot F$ shows the filter effect on S_n of averaging over T sec.

To illustrate the effect of averaging time, Fig. 3.5 shows the standard deviation of power within each velocity bin when using the usual method of bins, as a function of averaging time. Here we have assumed an exponentially decaying coherence of the form $\exp(-3Dn/\bar{u})$.

In Fig. 3.2 the resulting X-Y coordinate system is shown. The X-axis represents a segment of the power curve. Also shown are two "methods of bins", dividing into wind velocity intervals with subsequent power averaging and dividing into power intervals with subsequent wind velocity averaging, respectively. That the two "methods of bins" give different results is well known in statistics. It is connected to the least square fitting of a line to a series of points. This fitting can assume that one of the parameters (U or P) is accurately known, where-

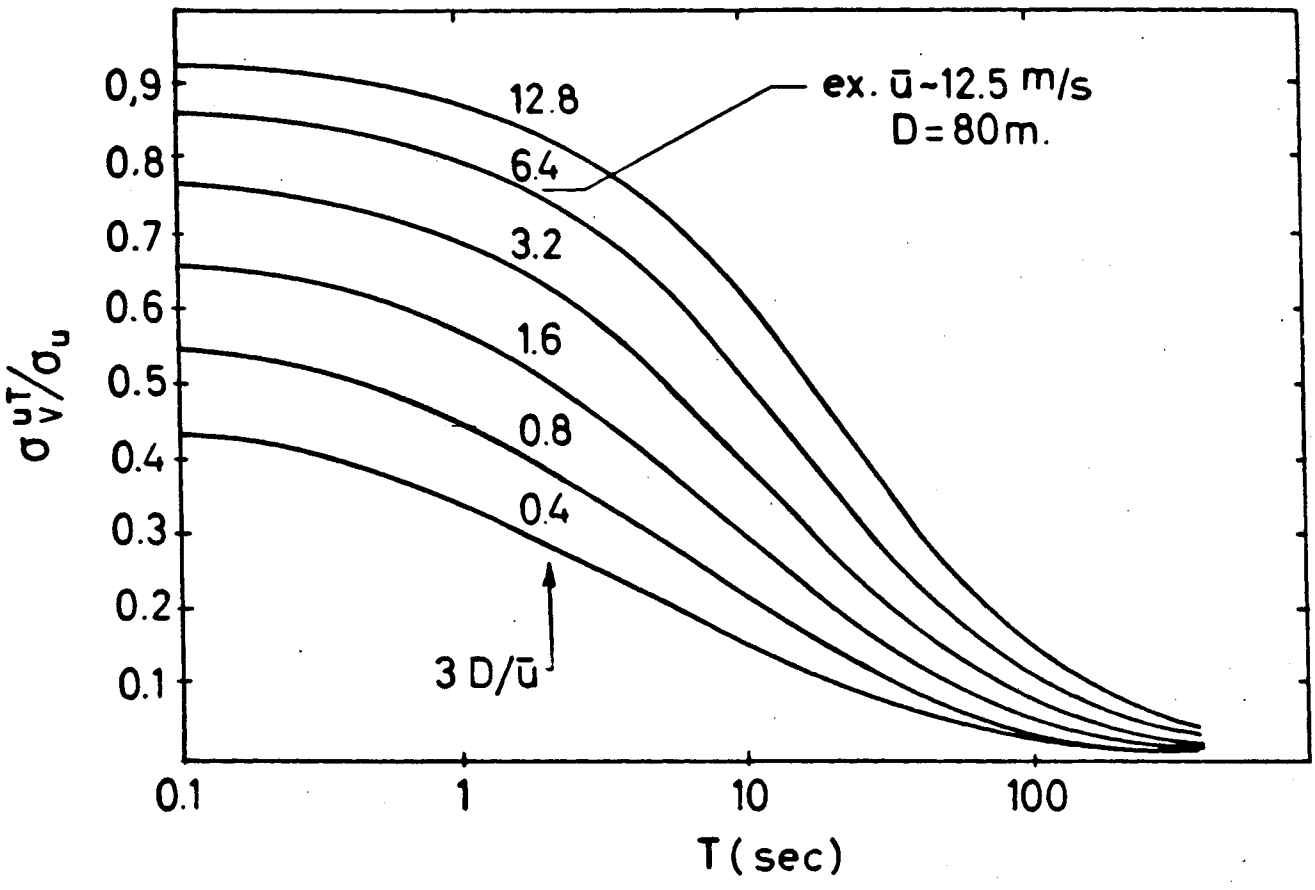

Fig. 3.5. Scatter as a function of averaging time. The parameter $3D/\bar{u}$ of coh = $\exp(-3Dn/\bar{u})$ allows for the effect of mast to mill distance and wind speed. Only valid for longitudinal correlation, i.e. wind from mast to mill.

as the other one is uncertain. The accurately known parameter is used as the basis for class dividing the data points and the rms distance of the uncertain parameter from the line sought is minimized in Fig. 3.2b.

It is not clear when one of these methods of bins or the correlation ellipse should be used. If the scatter is primarily on either wind velocity or power (e.g. high frequency oscillations in power introduced from the grid as discussed in Section . (> ½ Hz) a method of bins would be favoured. If such variations are filtered out (here τ > 2s), and only turbulence induced fluctuations are present, the correlation method should be preferred.

We would suggest that a combination, where an averaging time is

used, that is long enough to remove the power fluctuations resulting from the structural dynamic of the turbine ($\tau > 2s$). Then the correlation ellipse presumably is the best answer.

The correlation ellipse derived so far is not the final answer to the power curve question. The resulting parameters, axis angle θ and axis centre position $\bar{u},\bar{p}$ are only determined with a certain uncertainty, which has to do with the statistical nature of turbulence. A spectral analysis of the uncertainties in these parameters is in progress and will be published later. As some preliminary conclusions of interest can be drawn, we shall quote the derived uncertainty in θ:

$$\sigma_\theta^2 \cdot (8\left[\int_o^\infty Co_{up}(\omega)F(\omega,\tau)d\omega\right]^2 =$$

$$\sum_n S_{pn}^2 + \frac{2\pi}{T}\int_o^\infty d\omega([S_u^2(\omega)+S_p^2(\omega)-2coh(\omega)S_u(\omega)S_p(\omega)]F^2(\omega,T) \tag{3.23}$$

In this expression the spectrum of electric power has been expressed as

$$S_p(\omega) + \sum_n S_{pn}\delta(\omega-\omega_n) \tag{3.24}$$

where the sum is a series of sharp peaks at the frequencies ω_n each containing a total variance S_{pn}, whereas the remainder $S_p(\omega)$ is the continuous part of the spectrum left over, when the peaks are removed, so total variance in the electric power is

$$\sigma_p^2 = \int_o^\infty S_p(\omega)d\omega + \sum_n S_{pn} \tag{3.25}$$

The second (main) term in Eq. 3.23 is inversely proportional to the total record length (measuring time) T. But it also depends on the averaging time τ through the factor $F^2(\omega,\tau)$ in the integral. The longer the averaging time, the smaller the value of σ_θ^2. Especially improved accuracy is gained so long as a larger τ cuts off uncoherent parts of the spectra.

The first term in Eq. 3.25 does not depend on the record length, but it does depend on averaging time τ. If the averaging time is long enough that dynamical resonance fluctuations in the electric power are averaged aout ($\tau > 2$ secs), the term disappears.

A complete analysis of the σ_θ^2 is not finished. It does appear, however, at a quick glance that the τ-dependence influences numerator and denominator in the σ_θ^2-expression in similar ways. The T-dependence would therefore seem to be of more importance than the τ-dependence. This would suggest the following conclusion: If only the averaging time is long enough, that the dynamical turbine resonances are averaged out, it is not very important what τ-value is finally used. The essential parameter determining the quality of the data is the total measuring time. Only by spending sufficiently long measuring time can high quality be ensured. Therefore we must also conclude that the relatively short runs with extensive instrument coverage available from the Gedser experiment are too short for power curve determination. The power curve determination on the basis of weeks of 10-min. average measurements (discussed in Chapter 2) is much to be preferred.

It has been seen in the developments in this chapter that the degree of coherence is extremely important. This importance is illustrated in Figs. 3.6-7 which show the difference between power curves determined from two different runs. Fig. 3.6 was a good wind situation, where the wind direction was precisely from mast to mill. Fig. 3.7 had the wind turned away by 50 degrees. In the latter case the coherence falls off at a much lower frequency. As illustrated in Eq. 3.21 σ_y is increased very much when there is little coherence. This is seen on the broad ellipses in Fig. 3.7. In each of the Figs. 3.6-7 three different averaging times were used. It is seen that longer averaging time leads to smaller power curve scatter.

Fig. 3.8 finally shows the same data as Fig. 3.7, but here the time series were subdivided into 3 short series, which were treated with the same averaging time.

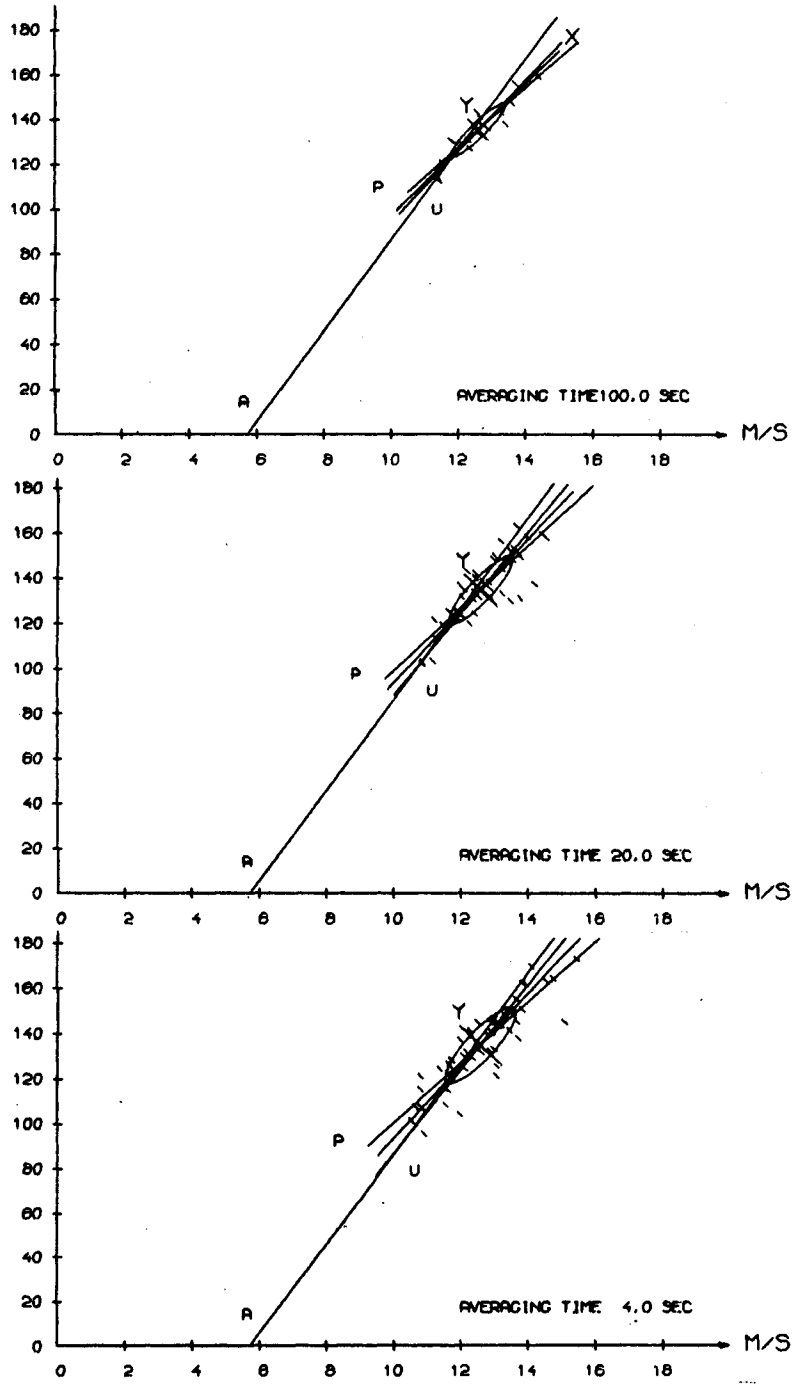

Fig. 3.6. Statistical analysis of (U,P)-plot. Three different averaging times. Good correlation case (wind mast → mill. Same data as in Figs. 3.1-3). The correlation ellipse with X and Y axes is shown. Also the method of bins classified according to U (line P) and P (line U) is shown.

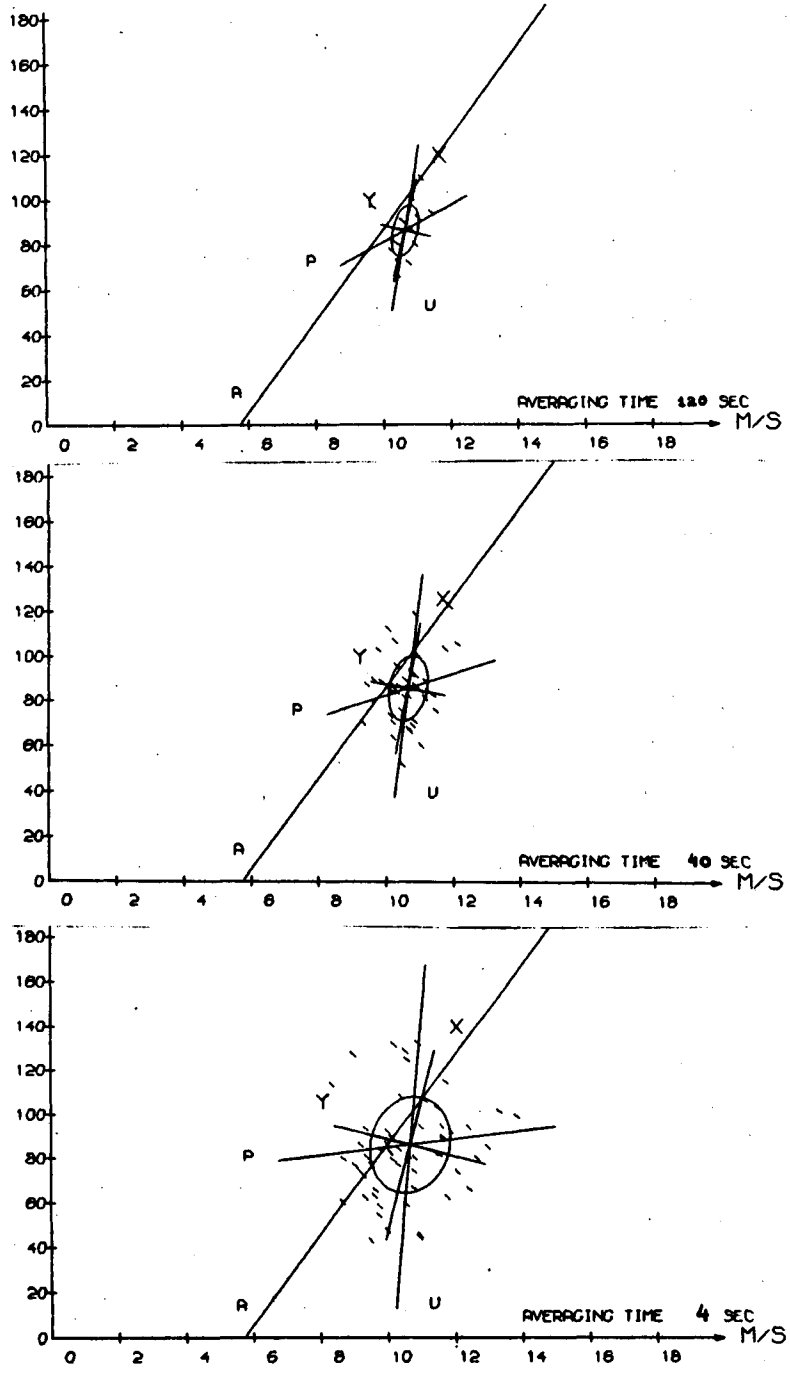

Fig. 3.7. As Fig. 3.6. But bad correlation case (wind 50^{o} off mast → mill direction).

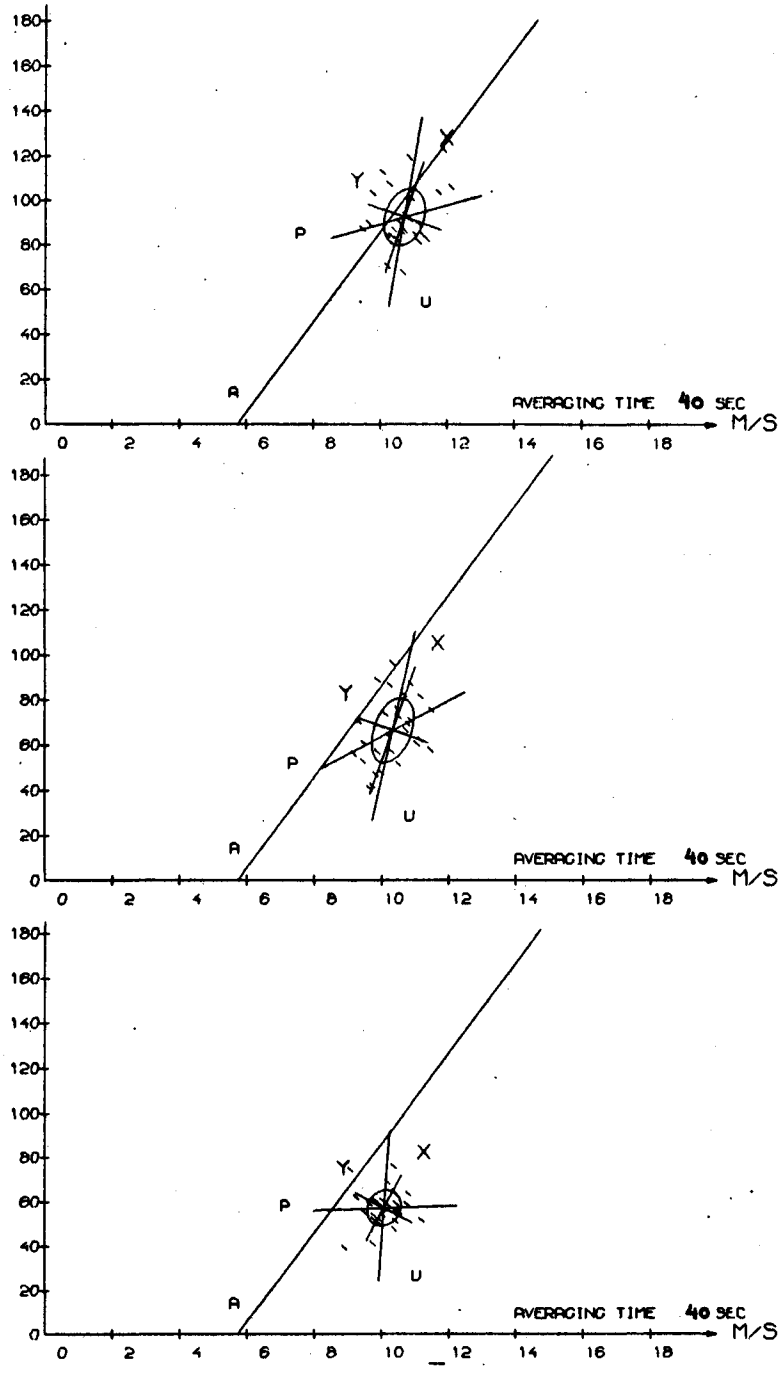

Fig. 3.8. Same as Fig. 3.7. But same averaging time for all three cases, which each covers only one third of the data.

The analysis of power curves given here does not solve the problems, but does indicate some important, tentative conclusions:

- Turbulence does account for a major part of the usually experienced difficulties in obtaining reliable power curve measurements.

- It is extremely important to have the anemometer and the wind turbine lined up correctly and close to each other as longitudinal coherence remains large at much higher frequencies (shorter times) than lateral coherence.

- The correct time delay $D/\bar{u}$ should be applied to the data at short averaging times.

- Dynamical resonance fluctuations should be averaged out, i.e. averaging times > $1/\nu_o$, where ν_o is the lowest resonance frequency, should be used.

- Long measurement periods are very important.

- Apart from averaging out dynamical fluctuations, total measurement time is more important than the question of averaging time. A reasonable averaging time would be one that gives a limiting frequency $1/\tau$ which is about equal to the coherence cut-off frequency.

REFERENCES

3.1. J.C. Kaimal, J.C. Wyngaard, Y. Izumi and O.R. Coté, Spectral characteristics of surface layer turbulence, Quart. J. Roy. Meteorol. Soc. 98, 563-589, (1972).

4. FLUCTUATIONS IN POWER OUTPUT

Introduction

While testing the Gedser turbine in 1957 significant fluctuations in the power output were observed. Fig. 4.1 shows a typical time history plot of power, clearly displaying the phenomenon The recognition of the problem resulted in an investigation of the transmission system in order to estimate the eigenfrequency and the damping. The eigenfrequency was measured to be 0.8 Hz.

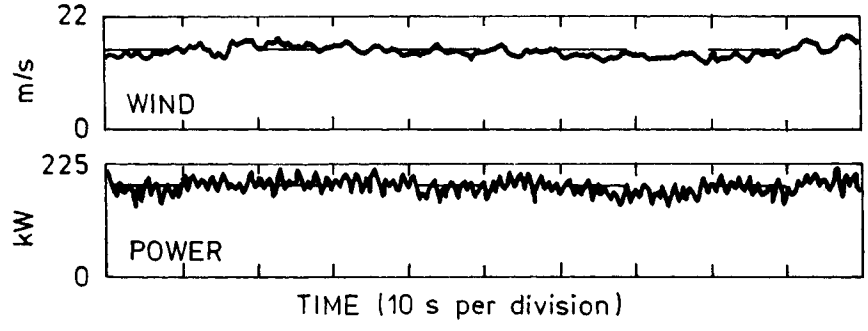

Fig. 4.1. Plot of wind speed and electric power output made during the resumed measurements.

The investigation, Ref. 4.1, concluded that no severe resonance should appear at high wind speed since the damping (disregarding structural damping) was considerably due to the fact that the generator "dissipates" energy.

This chapter will deal with the task of setting up a complete - though in many respects simplified - model of the total rotor.

The results are expressed in terms of spectra, which are compared with measurements achieved during the measuring campaigns at the Gedser wind turbine, 1977-1979.

Modelling the transmission system

Fig. 4.2 shows a frequency spectrum of the electric power output fluctuations taken at a mean wind speed of 13 m/s. Two important characteristics of the spectrum are 1) the broad hump at 0.01-0.3 Hz and 2) the three peaks at 0.4-1.0 Hz on top of

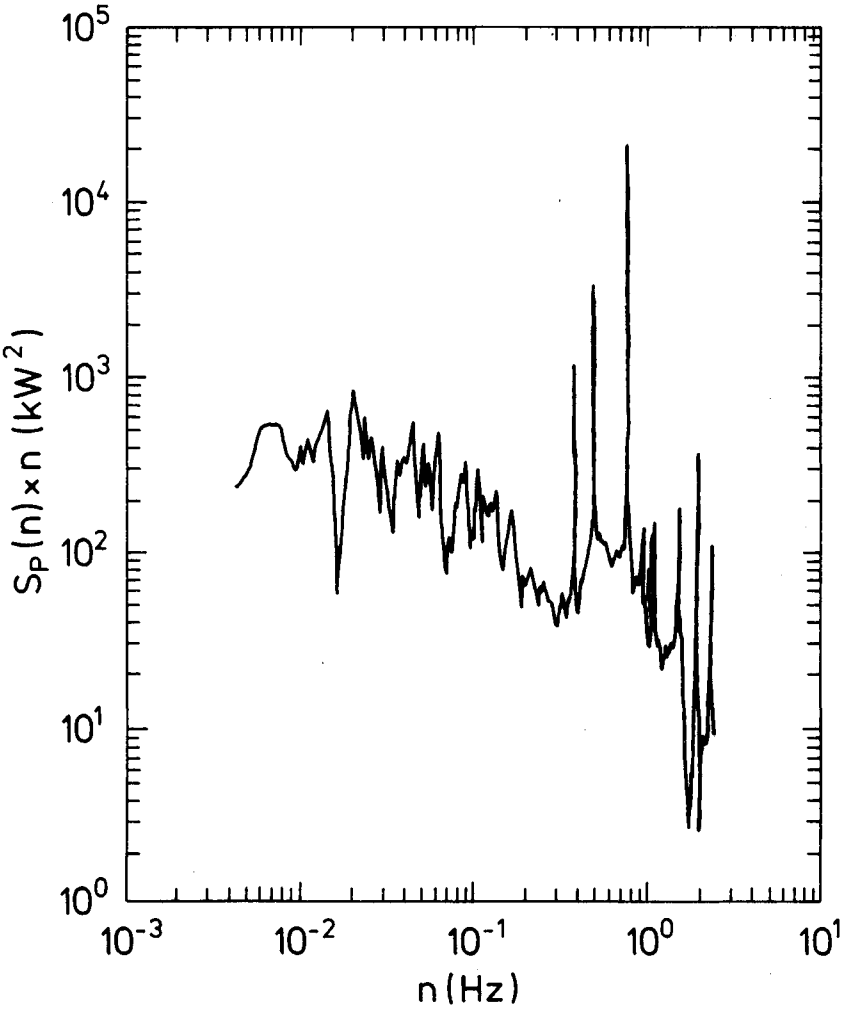

Fig. 4.2. Energy spectrum of electric power output, the Gedser wind turbine. The mean wind speed is 13 m/s.

a smaller hump. It is reasonable to believe that the low frequency hump is caused by the background turbulence and that the peaks follow from some kind of structural oscillations. However, analysis of the rotor structure shows that the lowest eigenfrequency found in the rotor itself is ~ 2.3 Hz, while the eigenfrequency of the concrete tower, on which the nacelle is mounted, is 2.4 Hz. Assuming that the combined structure acts linearly, only two frequencies remain important, namely 0.8 Hz (transmission) and the rotational frequency of the rotor.

Fig. 4.3 shows a schematic diagram of the transmission of the Gedser wind turbine. The transmission consists of two chain drive gears and three shafts, the total gearing ratio being 25 (the rotor shaft is actually not existing since one of the sprocket wheels is mounted directly on the rotor).

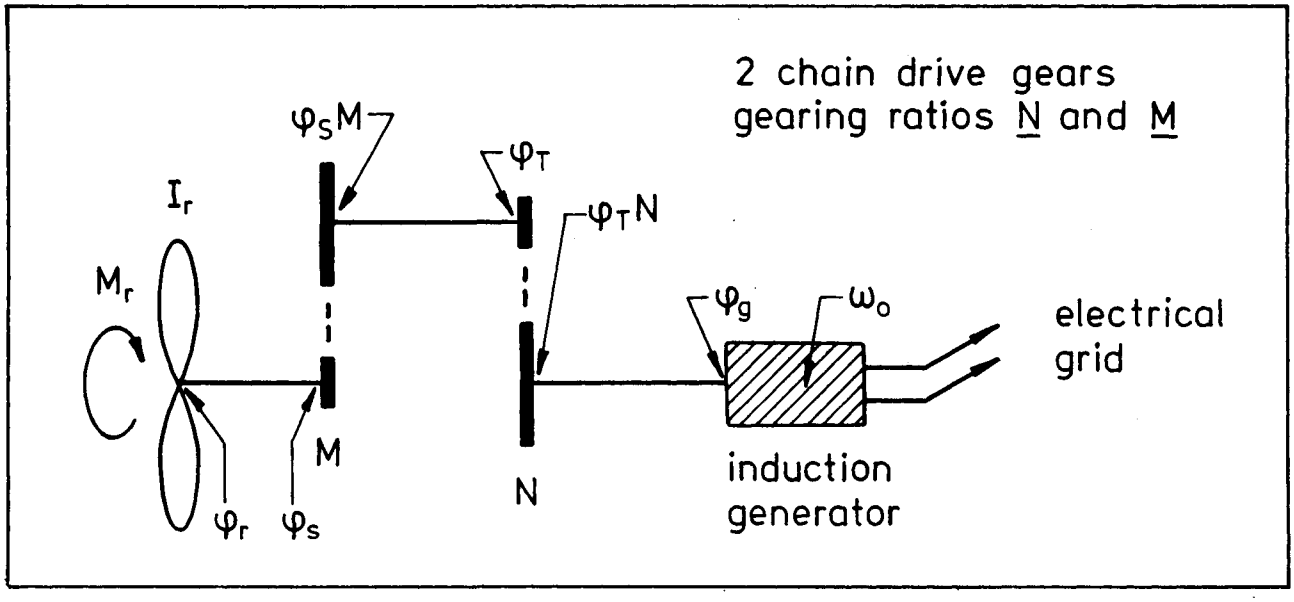

Fig. 4.3. Schematic diagram, showing the transmission of the Gedser wind turbine.

The induction generator locks the angular speed of the generator onto the electrical grid, i.e. the angular speed of the rotor is nearly constant. The ϕ's denote the angular position of the indicated parts of the shafts. ω_o is the angular speed of the magnetic stator field, for this generator $\omega_o = 2\pi f_g/4$, where f_g is the utility grid frequency (~ 50 Hz).

Assuming that the chain-drive gears are very rigid compared with the shafts and that the chains are constantly stretched, we get the following equations of torque for the shafts

$$M_v = I_r\ddot{\phi}_r - k_r(\phi_r-\phi_s) \tag{4.1}$$

$$k_r(\phi_r-\phi_s) = Mk_s(M\phi_s-\phi_t) \tag{4.2}$$

$$k_s(M\phi_s-\phi_t) = Nk_g(N\phi_t-\phi_g) \tag{4.3}$$

Since the masses of the shafts and the sprockets are considered to be negligible, the torque reaction of the generator expressed by electric power output will be

$$k_g(N\cdot\phi_t-\phi_g) = \frac{P}{\omega_o} \tag{4.4}$$

The power generation of an induction type generator can be expressed by

$$P = c'\left(\frac{\dot{\phi}_g-\omega_o}{\omega_o}\right)$$

where the dot denotes time derivative. $(\dot{\phi}_g-\omega_o)/\omega_o$ is specified for this particular generator to be 1 per cent when P = 200 kW. Usually ω_o is considered to be constant, however, allowing ω_o to vary, P can be written as (with $c = c'/\bar{\omega}_o^2$)

$$P = \bar{\omega}_o\cdot c\cdot(\dot{\phi}_g-\omega_o) \tag{4.5}$$

Through some trivial calculations Eqs. 4.1-4.5 reduce to a second order, differential equation in P:

$$\ddot{P} + \left(\frac{K_E}{c(MN)^2}\right)\dot{P} + \omega_e^2 P = \omega_e^2\left\{M_u\omega_o/(MN) - C_\omega\dot{f}_g\right\} \tag{4.6}$$

K_E is the equivalent torsional stiffness of the transmission system, $\omega_e = \sqrt{I_r/K_E}$ is the eigenfrequency, $M_u = M_u(t)$ is the windload on the rotor, $C_\omega = (K_E\cdot\omega_o\cdot 2\pi)/(\omega_e^2(MN)^2\cdot 4)$ and f_g is the derivative of the electrical grid frequency. The frequency response function of Eq. 4.6 is

$$|H(n)| = \left\{\left((1-\left(\frac{n}{n_e}\right)^2)^2 + (2\xi)^2\left(\frac{n}{n_e}\right)^2\right)\cdot\omega_e^2\right\}^{-\frac{1}{2}} \tag{4.7}$$

where $n_e = \omega_e/2\pi$ and $2\xi = K_E/(c(NM)^2\cdot\omega_e)$. $|H(n)|^2$ is shown in Fig. 4.4.

The various constants above can be calculated or derived from structural data, and the measured eigenfrequency, ω_e:

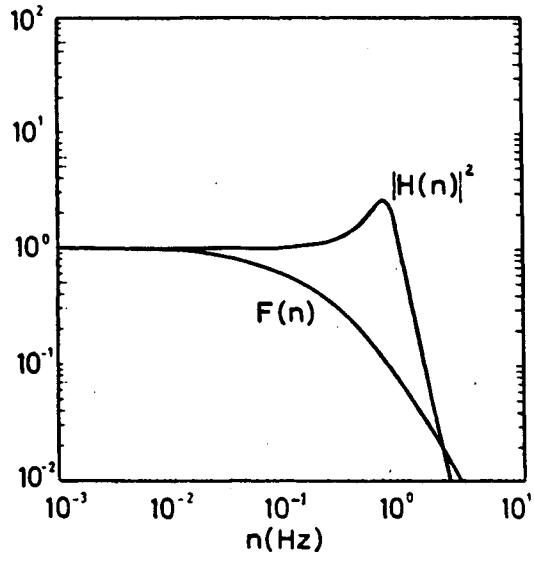

Fig. 4.4. The squared frequency response function for the transmission and the turbulence "filter" function F(n), which is explained later.

$$I_r = 3.0 \cdot 10^5 \text{ kg m}^2$$

$$\omega_e^2 = 0.8 \cdot 2\pi \text{ rad/s}$$

$$K_E = \omega_e^2 \cdot I_r = 7.58 \cdot 10^6 \text{ kg m}^2\text{s}^{-2}$$

$$2\xi = \left(\frac{1}{\omega_e}\right) \cdot \left(\frac{K_E}{c\,(NM)^2}\right) = 0.59 \quad \text{and}$$

$$C_\omega = \left(\frac{I_r \cdot \omega}{NM}\right) \frac{2\pi}{4} = 5.92 \cdot 10^4 \text{ Nms}$$

To produce a solution to Eq. 4.6 it will be necessary to estimate the wind load which drives the rotor and the load caused by a non-constant grid frequency f_g.

Windload

For very slow variations (low frequencies) in wind speed it is found to a very good approximation that P is a linear function of wind speed in the range 6-15 m/s, i.e.

$$\bar{M}_u = k_u \cdot \bar{U} + b \ , \quad \bar{P} = \bar{\dot{\phi}}_r \cdot M_u \tag{4.8}$$

where k_u and b are constants. Fig. 4.5 shows the power curve determined by means of 10-min. averaged values of wind speeds at hub height and of electric power output. The plot shows that the deviations from a straight line is small, at least locally. The power curve is fitted by the line $\bar{P} = 20.2 \cdot (\bar{U} - 5.75)$ kW in

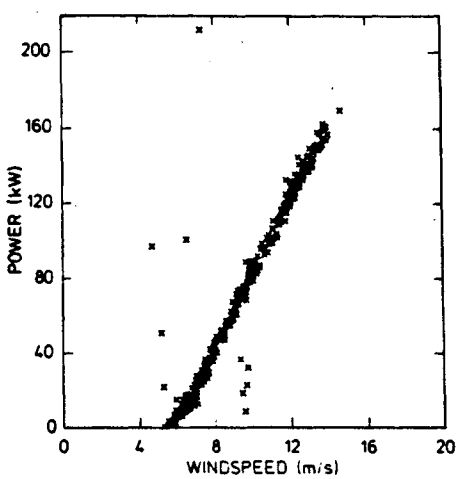

Fig. 4.5. Power curve made on basis of 10-min. average measurements.

the wind speed range $5.75 < U < 15.0$ m/s. This approximation leads to the determination of the constants in Eq. 4.8

$$k_u = 6.39 \cdot 10^3 \text{ Ns} \quad \text{and} \quad b = 5.75 \text{ m/s} \ .$$

We now assume that the contribution to the total torque from a small area dA on the rotor can be expressed as

$$dM_u(t,x,y) = (k_u \cdot U(t,x,y) + b)\,dA = d\bar{M}_u + k_u \cdot U'(t,x,y)\,dA \tag{4.9}$$

where $U(t,x,y) = \bar{U}(x,y) + U'(t,x,y)$ and x and y are the coordinates of the small area. By integrating over the rotor, we get the total torque at the time t:

$$M_v(t) = \iint k_u \cdot U'(t,x,y)\,dxdy + \bar{M}_v \tag{4.10}$$

Assuming that the wind velocity is vertically and horizontally homegeneous, the spectrum of M_u can be derived

$$S_{M_u}(n) = \iiiint S_m(x,x',y,y',n)\,dxdx'dydy'$$

$$= S_u(n) \cdot k_u^2 \iiiint R(x,x',y,y',n)\,dxdx'dydy' \qquad (4.11)$$

which holds when the phase spectrum is identically zero. Using Davenport's suggestion, Ref. 4.2, the integral in Eq. 4.11 takes the following form:

$$F(n) = \iiiint R(x,x',y,y',n)\,dxdx'dydy'$$

$$\simeq \left\{\left(1 + \frac{8}{3}\frac{n \cdot h}{\overline{U}}\right)\left(1 + 4\,\frac{n \cdot b}{\overline{U}}\right)\right\}^{-1} \qquad (4.12)$$

b and h are the horizontal and vertical dimensions of the structure. It should be noted that the final expression (Eq. 4.12) is an approximation since the rotor is actually a circular structure, while the expression was derived for rectangular structures.

Eq. 4.9 assumes that each area dA contributes equally to the driving moment. This very crude approximation facilitates the derivations. The load on the airfoil, however, increases with the distance to the axis, and so does the lever arm. Comments will be made later.

The filter function F(n) is shown in Fig. 4.4, h and b being 24 m, which is the diameter of the rotor, together with the frequency response function.

Utility grid frequency variations

Slow grid frequency variations will cause the generator and the rotor speed to vary in such a way that the electrical slip and the power production at constant wind speed is kept constant. For fast variations, however, the inertia of the rotor will keep the generator speed constant, and therefore fast grid fre-

quency variations will go directly into slip variations and therefore into power variations.

Fig. 4.6 shows a typical example of grid frequency variations as a function of time. The amplitude of the fluctuations is of the order of 0.01 Hz, which corresponds to a 4-7 kW variation in power output at constant generator speed. The frequency variations were not measured during the experiment. For an order of magnitude calculation, we will assume that the variance (energy) in the frequency fluctuations $\sigma_{f_g} = 0.01$ Hz is distributed according to

$$S_{f_g}(n) = \sigma_{fg}^2 \frac{1}{\sigma_o^2\sqrt{2\pi}} e^{-\frac{1}{2}\left(\frac{n-n_o}{\sigma_o}\right)^2} \qquad (4.13)$$

which is shown in Fig. 4.7 with $\sigma_o = 0.10$ Hz and $n_o = 0.8$ Hz, where n_o is the peak frequency. This spectrum will be used in the model, since the actual spectrum was not measured.

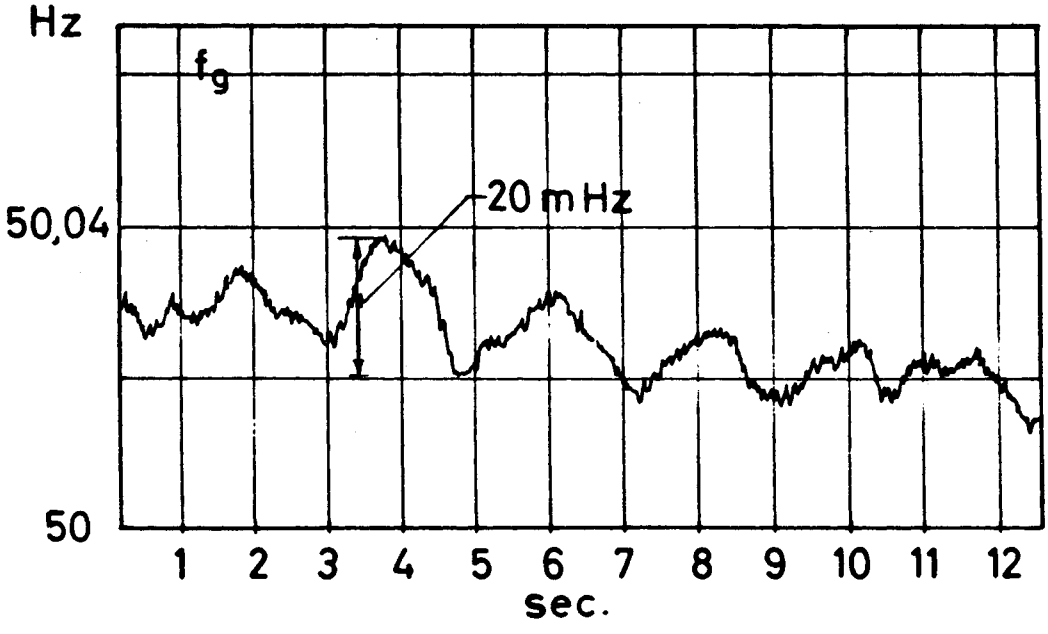

Fig. 4.6. Electrical grid work fluctuations recorded on Zealand.

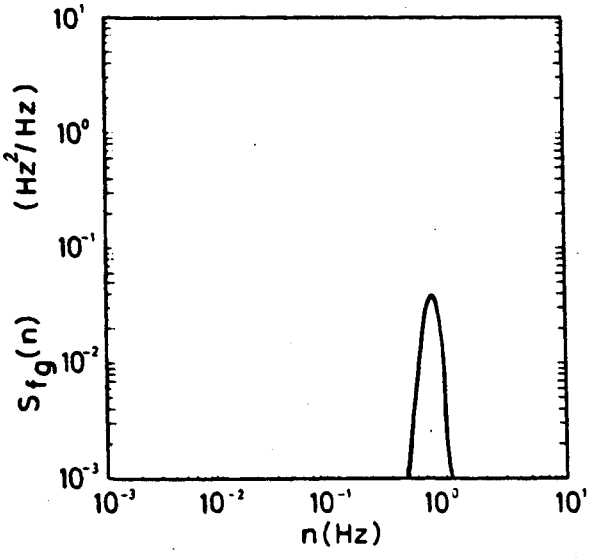

Fig. 4.7. Electrical network oscillations in its spectral representation, based on Eq. 4.13.

Comparison of model and measurements

Using the loads described above it is possible to achieve a spectral solution to Eq. 4.6. The only missing quantity is the spectrum of the longitudinal wind speed. The wind speed was recorded and a Kaimal-spectrum (Ref. 4.3) was fitted to the measured spectrum:

$$S_u(n) = \left(\frac{99}{2}\right)\left(\frac{H_h}{\bar{U}}\right)\sigma_u^2 \left\{1 + 33\left(\frac{H_h}{\bar{U}}\right)n\right\}^{-\frac{5}{3}} \qquad (4.14)$$

where H_h is hub height and σ_u^2 is the total variance of u. Eq. 4.14 together with a measured spectrum is shown in Fig. 4.8. Using the spectra $S_u(n)$ (4.14) and $S_{f_g}(n)$ (4.13), the spectral solution to Eq. 4.6 will be

$$S_p(n) = |H(\omega)|^2 \left\{C_u'^2 S_v(n) F(n) + C_\omega^2 n^2 S_{f_g}(n)\right\} \qquad (4.15)$$

where $C_u' = k_u(\bar{\omega}_o/NM)$. This solution holds when M_r and f_g are uncorrelated.

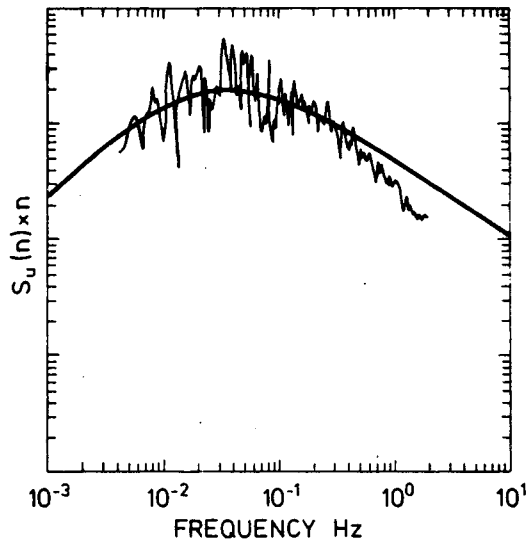

Fig. 4.8. Measured u-spectrum together with fitted Kaimal spectrum.

In Fig. 4.9 a measured spectrum is shown together with the results of the model. The solid curve corresponds to Eq. (4.15), while the dashed curve is Eq. 4.15 with F(n) = 1, i.e. that all eddy sizes are considered to extend over the whole rotor. The last curve (dash-dot) is the result of the model assuming that the grid frequency f_g is constant.

Fig. 4.9 shows that the energy spectrum of power output reflects the "background" turbulence directly. At higher frequencies the wind turbine will act as a filter to the turbulence since the individual eddies will only extend to a part of the rotor, while the eddies corresponding to lower frequencies cover the entire rotor. The filter function used for modelling, F(n), had a rather smooth characteristic, while the measured filter characteristic has a more pronounced cut-off (at 0.2 Hz). This can be explained by the fact that the wind load at different parts of the rotor does not contribute uniformly to the driving torque as assumed in the model: the outer part of the blades will usually be heavier loaded and the lever arm of the force will be longer than for the inner part. This means that it is more critical whether the eddies are smaller or larger than the rotor.

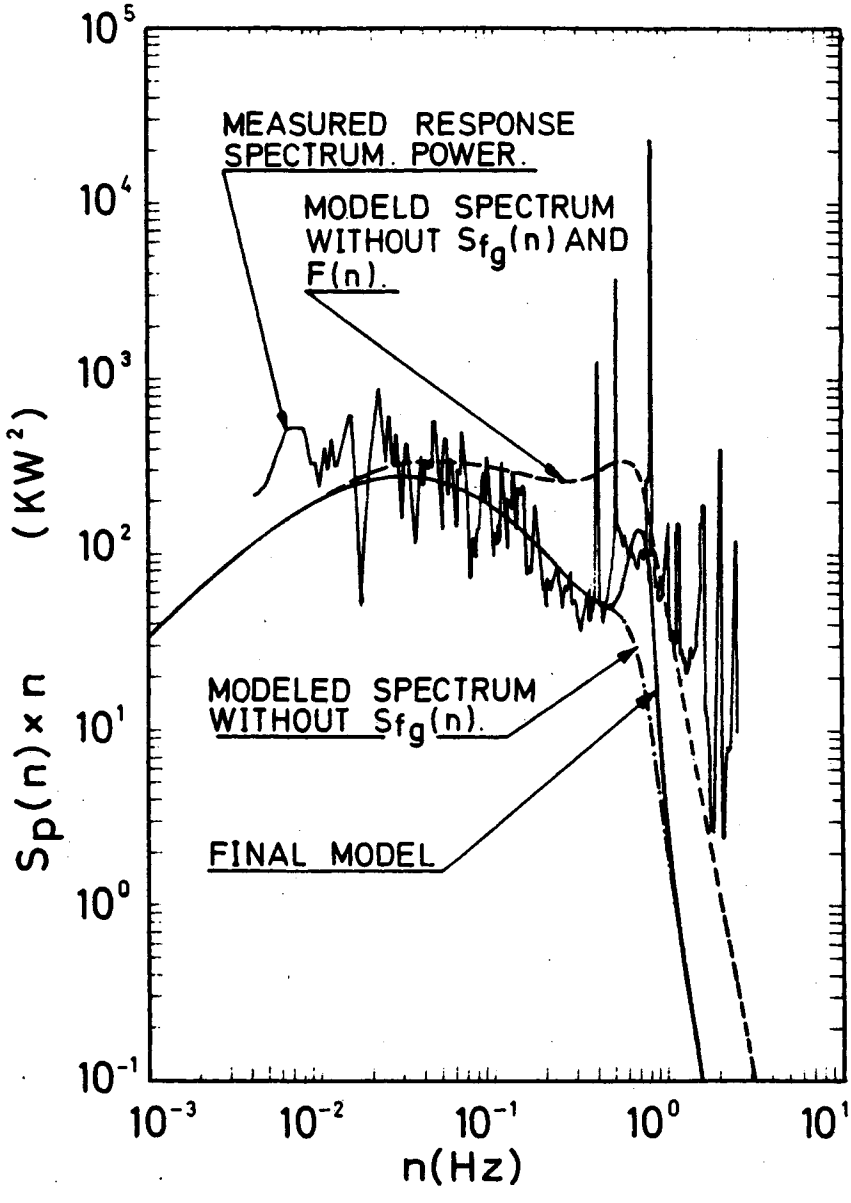

Fig. 4.9. Results of different combinations of the input to the model.

For the Gedser wind turbine the eigenfrequency of the transmission has been measured to be 0.8 Hz. The critical damping ratio as calculated from structural constants is 0.3 which indicates that the system is highly damped. Therefore the described power train model cannot explain the very energetic peaks in the spectrum. Furthermore, the lowest eigenfrequency of the rotor structure is ~ 2.3 Hz, while the three most energetic peaks in the spectrum is 0.4, 0.5 and 0.8 Hz. This seems to imply that the oscillations are not caused by internal oscillation in the rotor. For this reason the feature of a not completely steady grid frequency was included in the model. By do-

ing this it is possible to explain a part of the concentration of energy at 0.4-1.0 Hz, but since $S_{fg}(n)$ was not measured, it is not possible to get the true picture of the influence of the grid on the power output.

The result of the model shown in Fig. 4.9 was based on a "synthetic" spectrum of the grid frequency and the width of this spectrum is illustrated in Fig. 4.7. But since it was not measured, it might be very narrow. For instance, the 0.4 Hz peak could be the result of the non-constant grid frequency.

The rotational speed of the rotor is 0.5 Hz, which seems to coincide with one of the three most pronounced (and energetic) peaks in the response spectrum.

Another possible complication is the fact that the actual load on each rotor element consists of a stochastic and a periodic part, the last one caused by the blades moving up and down in the wind shear. The result is that the total load is not completely stationary. The implications of this are not obvious. Ref. 4.4 indicates that the load will be a series of narrowband peaks at frequencies governed by the rotational frequency and multiples hereof.

Conclusions

- An example of the fluctuations of the electric power output is shown in Fig. 4.1 in the form of a time history plot. The rms-value is app. 30 kW at an average power output of 200 kW. Fig. 4.2 displays the results of a spectral analysis of electric power, showing several important features. For lower frequencies ($n < 0.3$ Hz) the power output seems to reflect the background turbulence rather directly. Between 0.3 and 1.0 Hz there is a concentration of energy (app. 30% of the variance). Besides a slight increase in the overall spectral density in this range, most of the energy is concentrated at three very narrow peaks, $n = 0.4$, 0.5 and 0.8 Hz. The peaks at frequencies higher than 1 Hz are not very energetic.

- A model of the transmission system is derived and the predictions of the response are shown in Fig. 4.9. The model describes the transfer of background turbulent fluctuation into electric power quite well. The damping of the power train turns out to be very high, therefore the peaks cannot be caused by simple resonance (the damping considered is only the result of the generator, i.e. the structural damping can be neglected).

- The model shows that a part of the energy in the range 0.3-1.0 Hz can be explained as induced by utility grid frequency oscillations.

- The 0.5 Hz peak might be caused by a combination of an imperfect rotor and the wind shear effect. The fact that the rotor is not a fixed structure, will have the impact that the load on the rotor is non-stationary. It is therefore possible that the 0.5 and 0.8 Hz peaks are results of non-stationarity which also goes for some of the peaks between 1.0 and 1.5 Hz.

REFERENCES

4.1. Danish Electric Utilities: "Report from the Wind Power Committee", (Vindkraftudvalgets Betænkning), Union of Danish Electric Utilities. (1962) (In Danish).

4.2. A. Davenport, The prediction of response of structures to gustry wind, International research Seminar on Safety of structures under dynamic loading, June 23 - July 1, 1977, Trondheim, Norway.

4.3. J.C. Kaimal, J.C. Wyngaard, Y. Izumi and O.R. Coté, Spectral characteristics of surface layer turbulence, Quart. J. Roy Meteorol. Soc. 98, 563-589, 1972.

4.4. André Raab, Combined effects of periodic and stochastic loads on the fatigue of wind turbine parts, The Aeronautical Research Institute of Sweden, 1979, Stockholm.

5. ROTOR RESPONSE

In the measurement report, Ref. 5.1, some conclusions were drawn regarding the rotor behaviour, based on the inspection of time tracks and spectra of the data. These findings are summarized in the first part of this chapter, and they are mostly of a descriptive character.

In order to find explanations for some of the more interesting features identified in the first part, and to enable a utilization in future design work, a simple structural model has been developed for the calculation of the stationary response over one revolution due to forces varying with the rotor rotational frequency. The second part of this chapter contains a description of the theory of the model, which is chosen as a frequency domain formulation, thus facilitating an extension to stochastic loads.

The program demands very little computer time, and it is therefore suitable for parametric studies. The third part of this chapter contains some results from calculations, in which the stiffness of the wires interconnecting the blade tips and the angle to the blade cross section principal axis are varied. By comparison with representative time tracks for one revolution, effective values of the wire stiffness and principal axis direction are identified. Using these values the influence on the rotor response characteristics of the stay system and of various load types is estimated.

The fourth part of this chapter brings conclusions as to what mechanisms are the most important in the rotor response. The performance and potential of the theoretical rotor model are discussed, and the most imminent needs for future developments are identified.

Summary of measurement results

The instrumentation for the structural measurements comprised primary sensors, e.g. strain gauges on the rotor and the measuring cylinder, and secondary sensors, e.g. position indicators for rotor and nacelle. The instrumentation was operated in an essentially non-selective way, that is, the largest possible number of sensors were recorded during each run.

With few exceptions the available signals are clean and free from errors due to noise. The majority of the channels have been recorded with a satisfactory resolution, frequencies up to 25 Hz being adequately represented. The digital signals recorded are typically of the order of 50-200 units (counts). Thus the resolution (sensitivity to changes in signals) is of the order of 0.5-2%.

Fig. 5.1 shows representative time tracks for a few revolutions during various operational conditions, while Fig. 5.2 shows a part of the stop sequence, including the instant when the generator is taken off the grid and the braking flaps are extended.

The time histories do not show any significant dependence on the operating conditions. Since the channels shown represent the majority of relevant phenomena, this means that the dependence, including gyral effects, is so small that a quantification demands rigorous analysis of the records.

During the stop sequence high frequency oscillations of small amplitudes are generated in the rotor during the first few revolutions with brake flaps extended. Only the outer stay force (NYS) does experience significant increases of amplitudes of both high and low frequency oscillations during stop, and they are to a lesser extent apparent in the bending moments near the blade tip. However, the force levels are far from representing any danger to the structure.

Table 5.1 shows average values for the entire run 17. The second part of the table gives rotor results in the form of forces

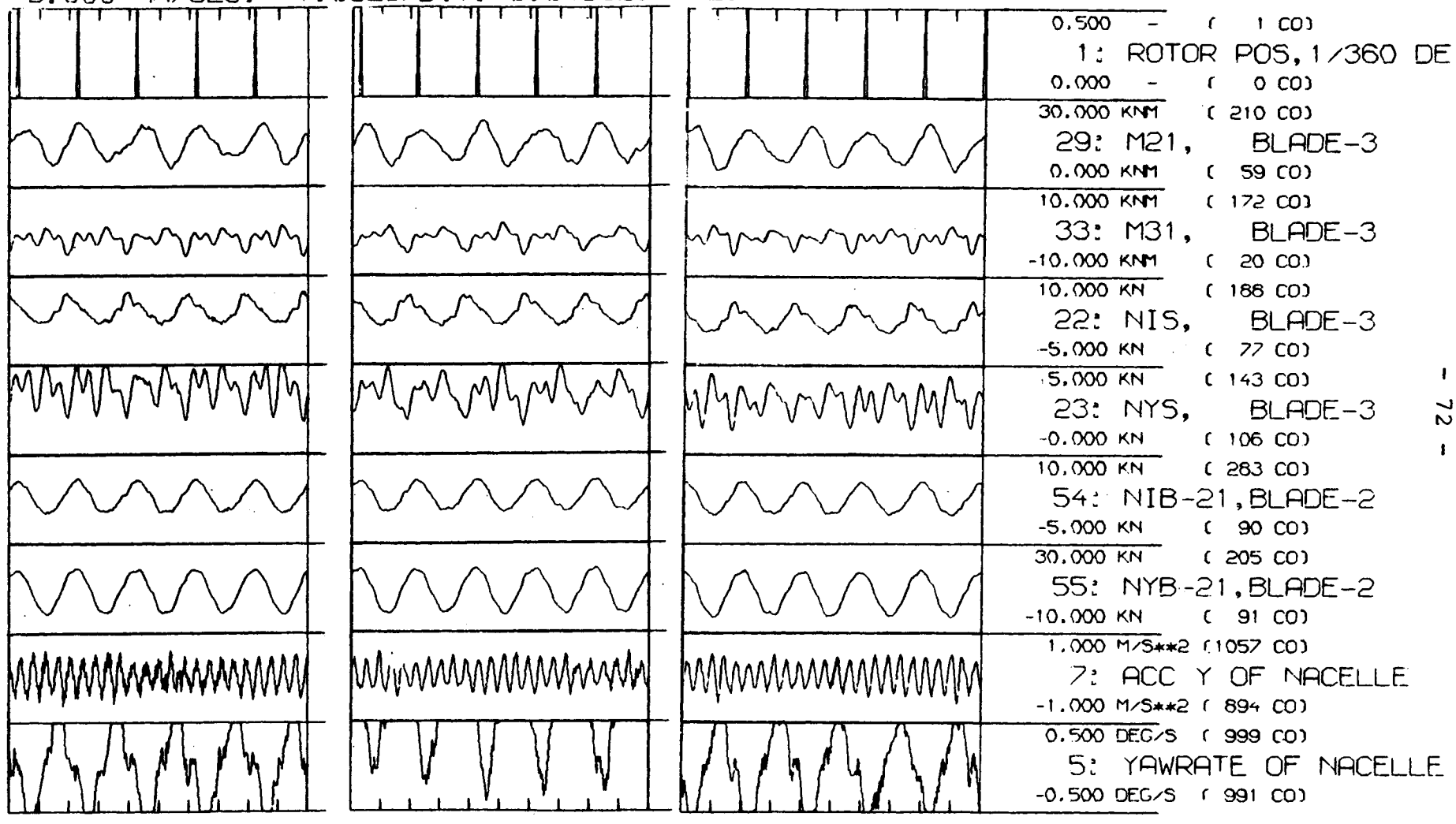

Fig. 5.1. Time history from run 16. a) normal running, b) yawing, c) skew wind.

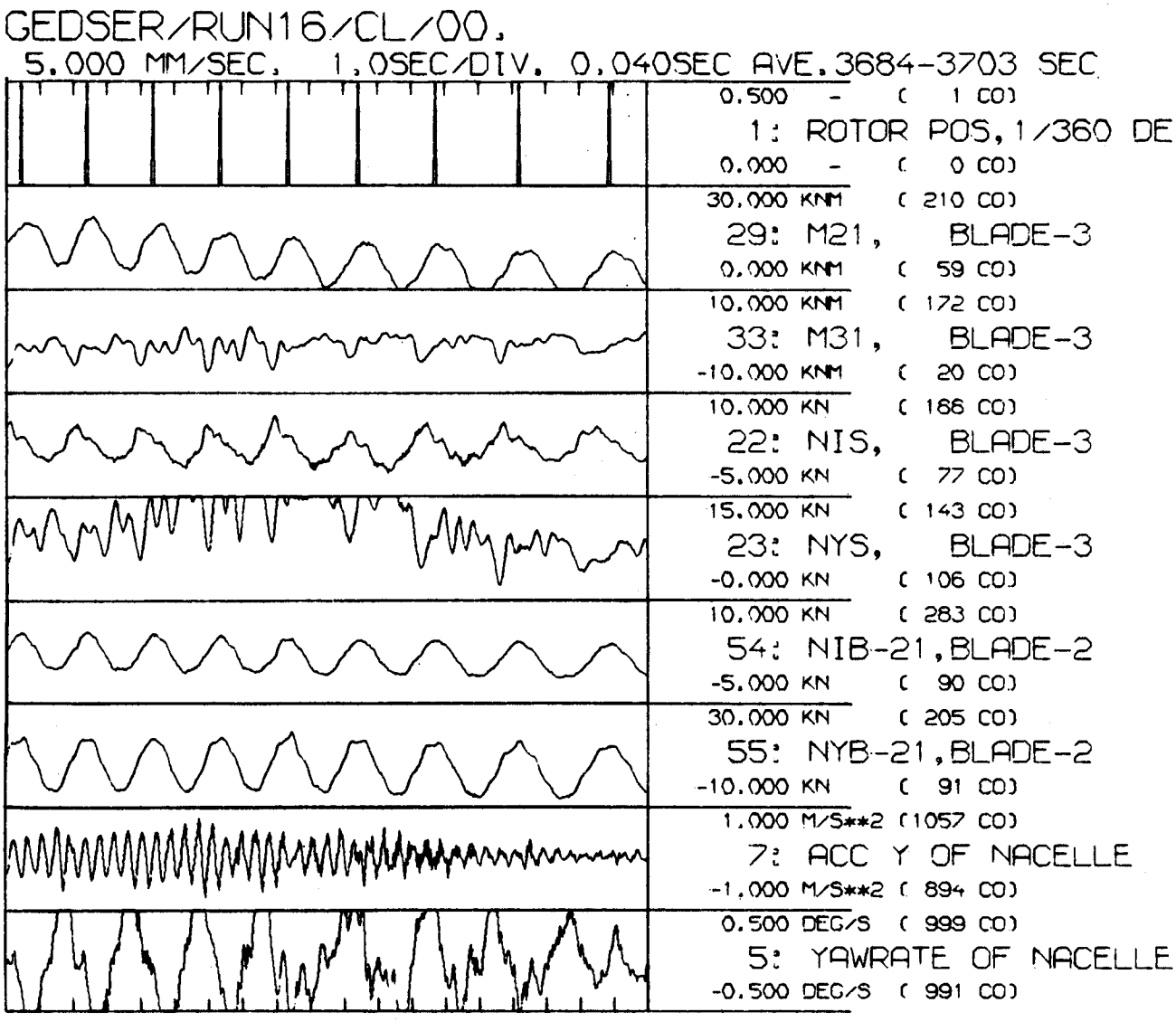

Fig. 5.2. Stop sequence.

TABLE: RESPONSE AVERAGES, TOWER CHANNELS

FILE:(CUC)GEOSEA/RUN17/CL/01. MAIN = RUN

AVERAGES FROM SCAN 100 TO SCAN 172100

SENSOR	UNIT	START AMPLITUDE	RUN MEAN	MIN	MAX	RMS
ROTPOS	-	0.00	0.01	0.00	1.00	0.10
ROTVEL	RAD/S	0.06	3.18	0.41	3.75	0.08
SHAMOM	KNM	0.00	0.00	0.00	0.00	0.00
AZIMUT	RAD	16.59	174.62	77.04	242.02	23.88
YAW	DEG/S	0.14	0.06	-2.96	3.18	0.52
ACC X	M/S**2	0.00	-0.00	-1.34	1.53	0.41
ACC Y	M/S**2	0.00	0.01	-1.43	1.57	0.35
ACC W	RAD/S2	0.00	-0.00	-0.81	1.02	0.18
P1	KN	0.86	1.97	-31.48	26.47	6.76
P2	KN	1.46	0.30	-15.72	24.80	4.58
M1	KNM	3.15	-73.54	-128.13	11.48	17.78
M2	KNM	5.12	45.27	-68.61	145.53	24.18
M3	KNM	2.89	4.35	-47.14	42.04	8.26
KVAR	KVA	0.01	12.42	3.19	13.95	1.58
KW	KWATT	0.01	71.67	-8.27	198.90	28.12
VOLT	VOLT	0.33	403.19	399.57	406.79	0.99
WVEL11	M/S	1.30	10.37	6.34	16.49	1.30
WVEL21	M/S	0.00	0.00	0.00	0.00	0.00
WDIR 1	DEG	7.56	180.60	154.00	208.00	6.67
WVEL22	M/S	0.00	0.00	0.00	0.00	0.00
WDIR 2	DEG	6.02	186.87	137.00	257.00	7.21

TABLE: RESPONSE AVERAGES, ROTOR CHANNELS

SENSOR	UNIT	START AMPLITUDE	RUN MEAN	MIN	MAX	RMS
NIS-3	KN	2.09	3.27	-2.02	10.13	2.02
NYS-3	KN	1.97	13.57	-2.01	30.63	3.89
NI1-3	KN	25.68	56.25	11.61	98.16	18.18
MI1-3	KNM	0.00	0.00	0.00	0.00	0.00
MI2-3	KNM	0.00	0.00	0.00	0.00	0.00
MI3-3	KNM	0.00	0.00	0.00	0.00	0.00
MI4-3	KNM	0.00	0.00	0.00	0.00	0.00
MI21-3	KNM	6.14	17.27	5.35	32.42	4.79
MI22-3	KNM	1.48	8.97	5.00	13.82	1.54
MI23-3	KNM	0.32	4.86	3.58	6.35	0.36
MI24-3	KNM	0.87	3.37	1.49	5.83	0.81
MI31-3	KNM	1.61	-0.81	-8.93	15.49	2.07
MI32-3	KNM	0.64	0.67	-0.51	1.75	0.32
MI33-3	KNM	1.19	-1.56	-3.30	4.16	0.75
MI34-3	KNM	0.03	0.53	0.13	1.01	0.09
NIB-31	KN	0.63	0.84	-0.52	2.73	0.28
NIB-32	KN	2.43	2.52	-0.85	6.62	1.75
NYB-31	KN	9.62	10.12	-2.68	24.93	7.17
NYB-32	KN	10.56	9.65	-4.26	25.89	7.76
NBS-31	KN	0.00	0.00	0.00	0.00	0.00
NBS-32	KN	0.00	0.00	0.00	0.00	0.00
PA	N/M**2	0.00	0.00	0.00	0.00	0.00
PB	N/M**2	0.00	0.00	0.00	0.00	0.00
PC	N/M**2	0.00	0.00	0.00	0.00	0.00
PD	N/M**2	0.00	0.00	0.00	0.00	0.00
PE	N/M**2	0.00	0.00	0.00	0.00	0.00
NIS-2	KN	2.78	2.87	-4.12	9.92	2.48
NYS-2	KN	1.70	14.68	0.27	32.10	3.63
MI21-2	KNM	5.72	18.74	6.65	43.31	4.64
MI23-2	KNM	0.27	3.98	2.57	5.45	0.40
MI31-2	KNM	2.18	-0.72	-8.26	22.56	2.70
MI33-2	KNM	1.13	-1.23	-1.75	2.84	0.40
NIB-21	KN	2.47	3.39	-0.48	7.61	1.78
NYB-21	KN	9.56	9.20	-3.83	24.25	7.23

TABLE: STRESS AVERAGES, ROTOR CHANNELS

SENSOR	UNIT	START AMPLITUDE	RUN MEAN	MIN	MAX	RMS
NIS-3	MN/M**2	1.60	2.49	-1.54	7.73	1.54
NYS-3	MN/M**2	1.22	8.43	-1.25	19.02	2.41
MI1-3	MN/M**2	1.80	3.94	0.81	6.87	1.27
MI1-3	MN/M**2	0.00	0.00	0.00	0.00	0.00
MI2-3	MN/M**2	0.00	0.00	0.00	0.00	0.00
MI3-3	MN/M**2	0.00	0.00	0.00	0.00	0.00
MI4-3	MN/M**2	0.00	0.00	0.00	0.00	0.00
MI21-3	MN/M**2	5.53	15.56	4.62	29.21	4.32
MI22-3	MN/M**2	0.73	4.39	2.45	6.77	0.75
MI23-3	MN/M**2	0.19	2.96	2.18	3.87	0.22
MI24-3	MN/M**2	0.58	2.26	0.99	3.90	0.54
MI31-3	MN/M**2	1.80	-0.91	-10.00	17.35	2.32
MI32-3	MN/M**2	0.17	0.80	-0.62	2.10	0.38
MI33-3	MN/M**2	2.50	-3.28	-6.92	8.73	1.53
MI34-3	MN/M**2	0.47	1.22	0.31	2.32	0.21
NIB-31	MN/M**2	2.58	3.42	-2.12	11.14	1.16
NIB-32	MN/M**2	7.96	8.27	-2.80	21.70	5.75
NYB-31	MN/M**2	6.92	7.28	-1.93	17.93	5.15
NYB-32	MN/M**2	7.54	6.89	-3.04	18.49	5.54
NBS-31	MN/M**2	0.00	0.00	0.00	0.00	0.00
NBS-32	MN/M**2	0.00	0.00	0.00	0.00	0.00
NIS-2	MN/M**2	2.12	2.19	-3.15	7.57	1.89
NYS-2	MN/M**2	1.66	8.12	-0.17	19.63	2.25
MI21-2	MN/M**2	5.16	16.88	5.69	39.02	4.18
MI23-2	MN/M**2	0.16	2.42	1.56	3.32	0.24
MI31-2	MN/M**2	2.44	-0.81	-9.25	25.27	3.03
MI33-2	MN/M**2	2.37	-2.59	-3.68	5.96	0.84
NIB-21	MN/M**2	8.11	11.11	-1.59	24.95	5.84
NYB-21	MN/M**2	6.98	6.72	-2.80	17.70	5.27

Table 5.1. Run 17. Averaged over total run.

and moments. The third part gives stresses derived from forces and moments. The stress values are based on measured cross sectional areas for the stays, Ref. 5.2, and on cross sectional properties calculated for the blades using the program SECTIO, Ref. 5.3. This was done as a part of the establishment of a beam finite element model of the blades and the rotor, cf. Appendix II. Stresses given for the blades are maximum stresses in the steel main spar as laboratory tests, Ref. 5.2, indicate that the skin does not carry load to any significant extent.

Based on values for the kinematic degrees of freedom (yaw rate and accelerations) the amplitudes in the motions may be estimated from the RMS values by assuming harmonic motions. The estimates become:

$x_{max} \sim 0.003$ m, axis direction and

$y_{max} \sim 0.002$ m, perpendicular to the axis.

These values are only indicative of the true values, because the signals are not purely harmonic signals. However, the values indicate that the orders of magnitude are small.

The gyral effects originating from the yaw movements may be estimated by computing the maximum gyral force P on the centre of gravity on a single blade

$$P = 2 \cdot m \cdot r \cdot \Omega \cdot Y$$

where m is the mass (1600 kg), r is the distance from the rotor axis to the mass centre (6 m), Ω is the angular velocity of the rotor (3.14 rad/s) and Y is the yaw rate. Based on yaw rate values 0.0116 rad/s and 0.05 rad/s (average during yaw and max. yaw rate, respectively), the following values are found

Max P $\sim$ 3.5 kN

RMS P $\sim$ 0.7 kN during yaw.

These values are sufficiently small to be difficult to detect in the time histories. It appears that the average values during yaw do not differ from the values for normal and skew wind operation in a way that permits an identification of special yaw effects. The RMS values do not differ significantly from normal operation values neither during yaw maneuvres nor during skew wind operation.

The rotor channel tables show that stresses are very low throughout the structure. Exceptions are the root cross section of the main beam of the blades, the outer stay and the wires interconnecting the blades. However, even here the average stresses are hardly more than 20% of the design limit 60 MN/m^2 (600 kp/cm^2), and the cyclic variations are small also, following the above-mentioned pattern.

The forces measured in the rotor assembly show that the stays and wires play an important role carrying considerable loads, especially gravity forces. By comparing the values for blade 2 and blade 3 it appears that the internal force system in the rotor has a high degree of symmetry.

As can be seen from Table 5.1 there is little difference between rotor signals during upstart and under run conditions. This indicates that gravity forces play a dominant role in the rotor assembly, which is supported by the time history plot, Fig. 5.1, that shows most of the rotor signals to have a strong harmonic 0.5 Hz component. Exceptions from this are the outer stays (NYS) and the out-of-plane bending moments (M3) that seem to have significant dependence on wind loading.

Fig. 5.3 shows examples of recorded moment distributions in blade 3. The distribution of driving moments (M2) is only slightly influenced by the mode of operation (in the wind, skew wind, yaw), while a marked dependence on wind speed is apparent. The out-of-plane bending moments (M3) are kept low by the stays and they depend stronger on the operating conditions, especially near the blade tip. Also the wind speed is of significance to the out-of-plane bending moments.

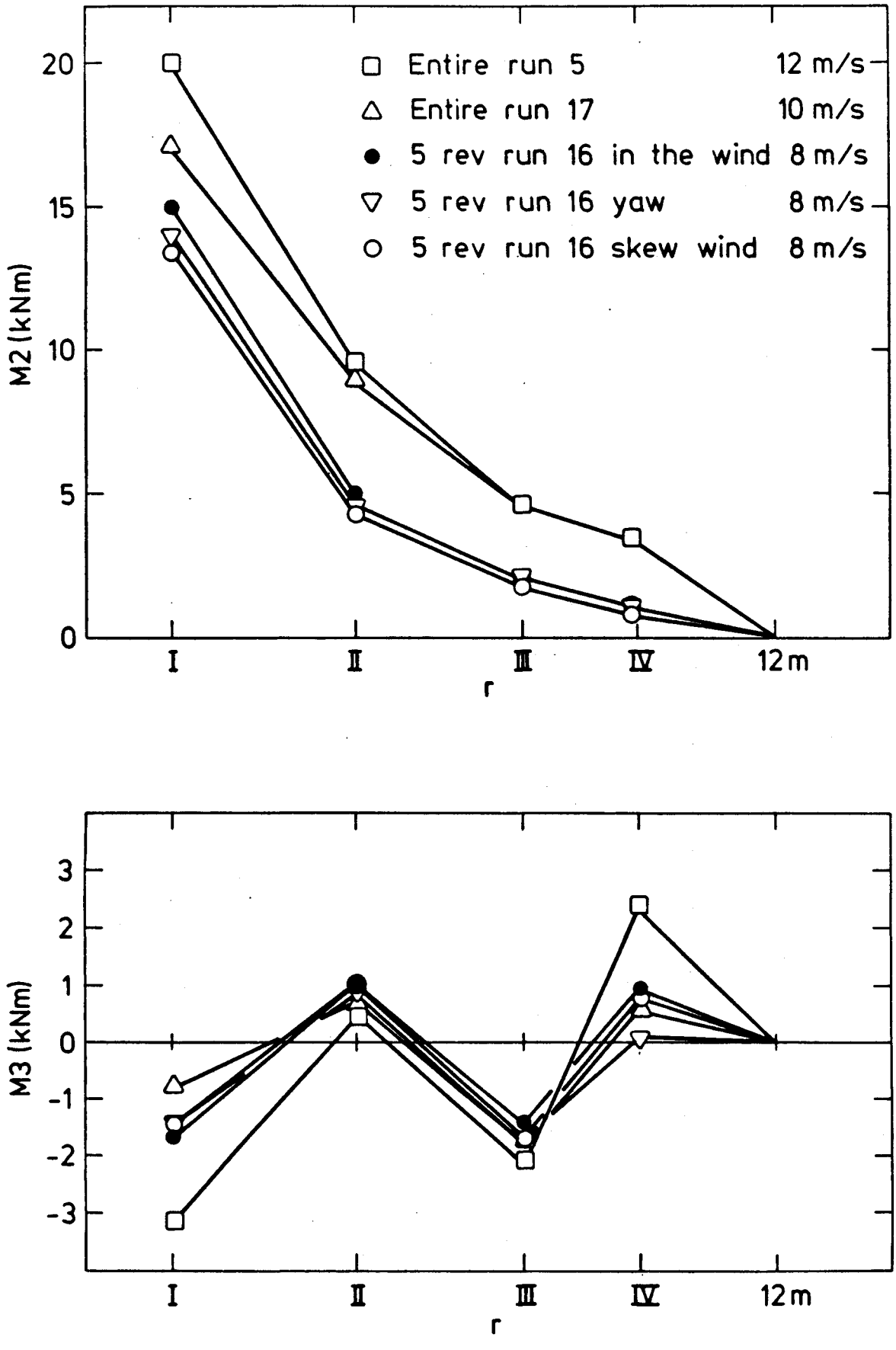

Fig. 5.3. Average moment distributions.

Average moments and forces are generally found to be linear functions of the electric power output of the turbine, as shown in Fig. 5.4. This figure shows M21 and N11, i.e. the wing root in-plane bending moment and the normal force together with the driving moment M_D as derived from

$$M_D = M21 - a \cdot N11 \ , \qquad (5.1)$$

where the term a•N11 is the contribution to the driving moment resulting from the normal force (the wing is mounted such that N11 will produce a resulting driving moment with the lever arm a). M_D^o, which is the resulting driving moment necessary to produce the electric power P, is shown for comparison. The linear dependence of power means that the average forces in the rotor assembly consist of constant forces due to the rotation of the rotor and contributions that are roughly proportional to the power output. (N11 decreases at increasing power as the outer stay NYS takes over the increased flapping moment but at the same times relaxes the blade normal force).

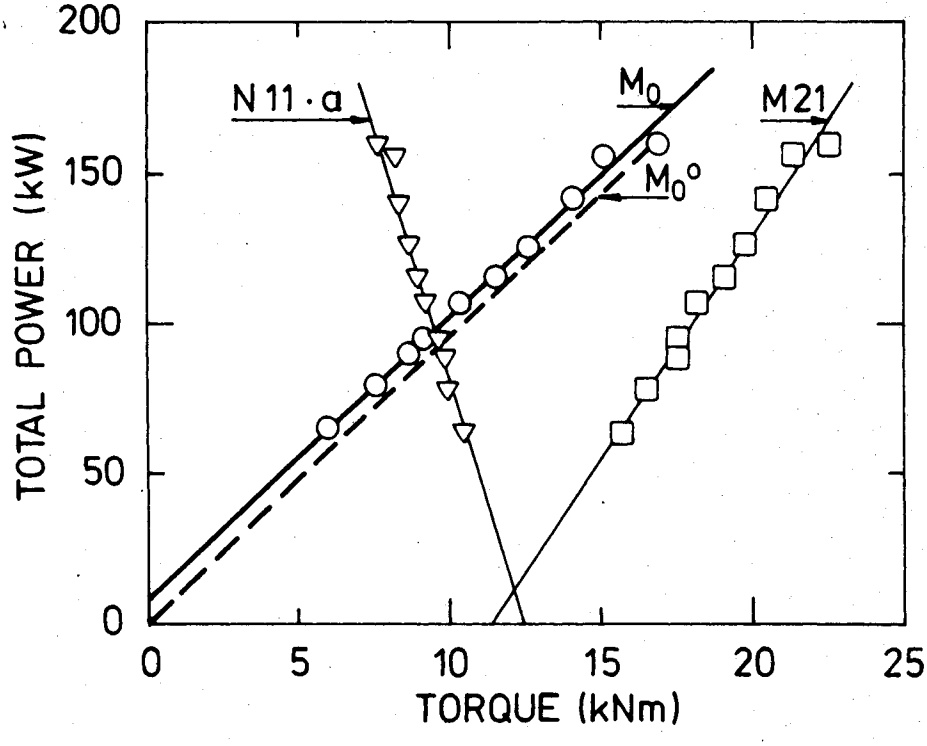

Fig. 5.4. Electric power versus measured root driving moment (M21) and corrected moment M_D.

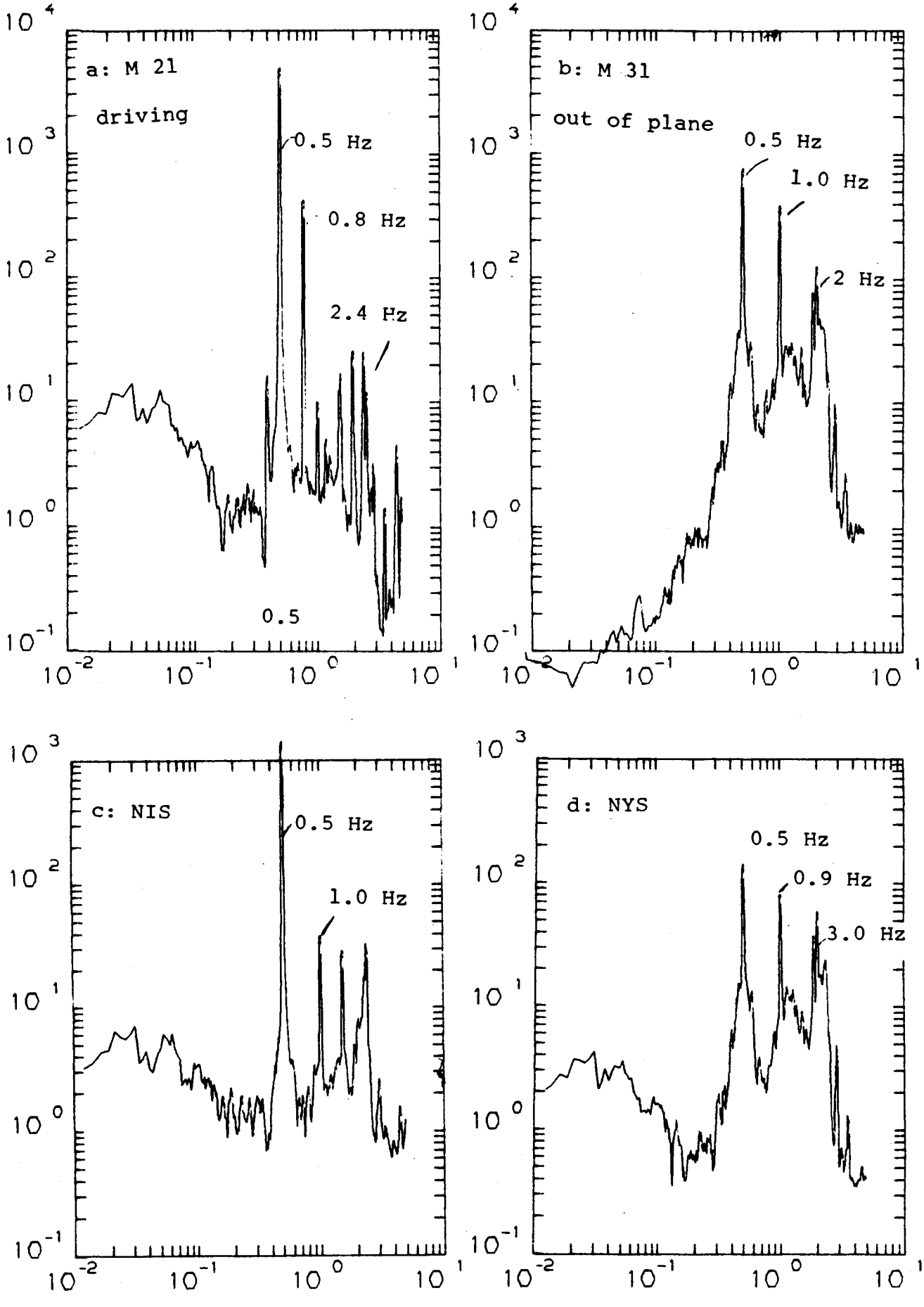

Fig. 5.5. Representative Fourier spectra (a-d).

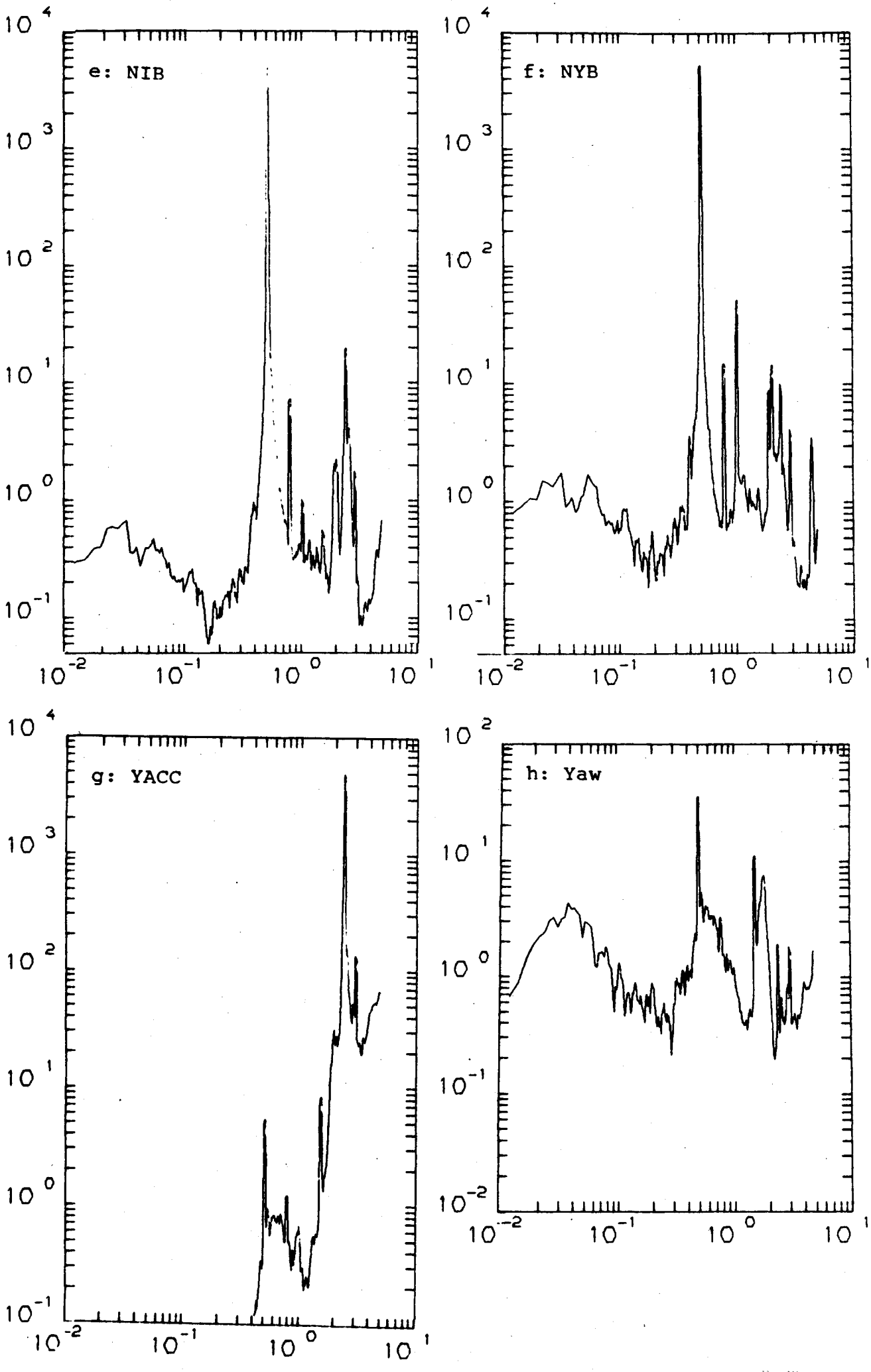

Fig. 5.5. Representative Fourier spectra (e-h).

The figures 5.5a to 5.5h show some examples on response spectra, covering the structural response types. The dominating frequencies in each channel are summarized in Table 5.2, but the spectra show many sharp peaks. Three peaks at frequencies known to exist are repeated in the spectra, namely

- 0.5 Hz Rotational frequency of the mill.

- ca. 0.8 Hz Frequency of power fluctuations.

- ca. 2.4 Hz Edgewise blade bending eigenfrequency.

In addition the frequency series 0.8 - 1.2 - 1.6 - 2.0 - 2.4 Hz and 0.5 - 1.0 - 1.5 - 2.0 Hz are present. They may be harmonics of 0.8 and 0.5 Hz, respectively, showing that these basic frequencies do not represent purely harmonic motion.

Sensor	Frequency, decreasing prominence				
M21-3	0.5	0.8	2.3/2.4	2.0	1.0
M31-3	0.5	1.9/2.1	1.0	1.6	-
NIS-3	0.5	2.3	1.6	1.0	(0.8)
NYS-3	0.5	1.0	2.1	2.4	(0.8)
NIB-21	0.5	1.0	2.0	2.4	0.8
NYB-21	0.5	2.4	0.8	2.0	1.0
Y-Acc	2.4	2.0	1.6	0.5	0.8
Yaw rate	0.5	1.6	2.0	2.0	0.8

Table 5.2. Summary of approximate prominent frequencies.

Spectra for the in-plane bending moment M21 (driving) moment and the out-of-plane bending moment M31 are shown in Figs. 5.5a and 5.5b, respectively. Both spectra are dominated by the rotational frequency 0.5 Hz, the driving moment spectrum having also 0.8 Hz and 2.4 Hz as energetic frequencies.

Spectra for NIS-3 and NYS-3 (inner and outer stay, respectively, restricting the out-of-plane bending) and for NIB-21 and NYB-21

(inner and outer wire interconnecting blades) are shown in Figs. 5.5c to 5.5f. Again the rotor frequency 0.5 Hz is the most prominent frequency, least pronounced in NYS-3. The spectra seem to indicate that the in-plane motions corresponding to the three known frequencies are transferred to both the stays and the wires in somewhat distorted patterns, indicated by the strong representation of the harmonic series. The peaks at 0.8 Hz and 2.4 Hz which are clearly seen in all the sensors that measure in-plane forces (M21, NYB, NIB) are not visible in the out-of-plane sensors (M31, NYS, NIS). This indicates that these frequencies are in-plane motions which are transferred only very weakly to out-of-plane motion. A striking feature which clearly distinguishes M31 (root flapping moment) from NIS and NYS is that the low frequency turbulence induced part (< 0.3 Hz) is suppressed markedly in M31. This fact is not fully understood but a suggestion could be: The large eddies (low freqiencies) cover all the rotor plane, giving a symmetric load, which allows the stays to relieve the wing beams of forces better than the unsymmetrical loads that can result from smaller eddies which hit only one blade. The transfer of in-plane motions into out-of-plane response may be caused by kinematic couplings due to nacelle movements and blade pretwist. Both mechanisms will cause the coupling to be largest at the blade tips, cf. NYS and NYB.

Spectra for the yaw rate and the Y direction acceleration (oblique to the rotor axis) are shown in Figs. 5.5g to 5.5h. The yaw rate spectrum is dominated by the 0.5 Hz rotor frequency, reflecting a continuous yawing movement. Since only few of the harmonics of the 0.5 Hz movement are pronounced this yaw movement seems to be within the slack of the yaw drive. The power fluctuation and blade vibration frequencies of 0.8 Hz and 2.4 Hz are visible in the spectrum, but the mechanisms for their transfer to the yaw rate are not obvious.

The y-acceleration spectrum is being dominated by 0.5 and 2.4 Hz. Since the x-acceleration spectrum resembles the y-acceleration spectrum, except that the 0.5 Hz peak as expected is missing, the 2.4 Hz peak most probably has its origin in tower eigen-

frequency.

By inspecting the spectra dealt with above, it has been found that three physically explainable frequencies dominate the entire rotor assembly. The 0.5 Hz induced by gravity or wind shear is the most prominent frequency in almost all channels, including the yaw rate. The presence of this frequency in the yaw rate spectrum indicates some unbalance of the rotor. The 0.8 Hz of the power fluctuations are most prominent in edgewise bending (M21 and NYB), indicating torsional oscillations of the rotor angular speed around the rotor axis. This also goes for the 2.4 Hz associated with the in-plane eigenfrequency of the blades. On the other hand, the 0.8 Hz peak is definitely weaker in the NYB and NIB-spectra than in M21, by a factor of app. 30 relative to the 0.5 Hz and 2.4 Hz peaks. This suggests that the 0.8 Hz corresponds to a sloshing mode of the rotor (blade movements in phase) whereas the 0.5 Hz and 2.4 Hz corresponds to more individual movements of the blade in different phases.

The most significant findings of this part are listed below:

- The stress levels in the rotor assembly are generally low, typical values at about 100 kW power being:

  Blade root ~ 20±10 MN/m^2

  Blade tip ~ 2±1 MN/m^2

  Stays ~ 12±4 MN/m^2 out-of-plane

  Wires ~ 10±10 MN/m^2 in-plane

  None of the stresses are close to the design stress 60 MN/m^2, and they are not drastically increased when the generator couples to the grid and when the mill is stopped.

- The stay forces are important. The forces on stays connecting the blade tips with each other are of a considerable magnitude, and these stays having force amplitudes of the order of 10 kN play a significant role in balancing the gravity

component of the driving moment. Similarly the stay connecting the blade tip with the hub seems to carry a considerable part of both average and fluctuating wind load. The force system in the rotor assembly has a high degree of symmetry.

- Gravity forces seem to be the most important loads on the rotor in terms of stresses related to the load. At both low and high wind speeds the rotor signals contain a strong harmonic component with the rotor frequency 0.5 Hz. In addition to this the frequencies 0.8 Hz (power fluctuations) and 2.4 Hz (in-plane bending eigenfrequency and possibly tower frequency) are prominent.

- The blade moment distributions seem to be little influenced by the mode of operation (yaw, skew wind) and wind speed, the out-of-plane bending moments being slightly more sensitive than the in-plane bending moments.

- The average forces in the rotor assembly are linear in the sense that they seem to consist of a constant part caused by the rotation of the rotor and a contribution from the wind load that is roughly proportional to the power output.

- The nacelle movements seem to be small, being considerably less than 1 deg. for yaw movements and a few millimeters for translational movements. The yaw movement is dominated by the rotor frequency 0.5 Hz while the accelerations are dominated by 2.4 Hz, possibly caused by tower vibrations.

- Gyral effects are too small to be clearly identified by inspection of the figures. However, the gyral tilting moment from one blade varies with the frequency 1 Hz, twice the rotor frequency, and this frequency is represented in the response spectra shown.

A simple rotor model

The findings of the previous part are descriptive of the features of this particular wind turbine. In order to further explain the fundamental mechanisms and thereby make the findings applicable in future design work, the development of a simple rotor model was initiated as a part of the analysis. It was considered essential that the model be simple in order to make parametric studies feasible, so that the effects of various parameters and load types could be identified.

The model described in this part is a model of a three-bladed, stayed rotor, in which each blade is represented by one beam element that is clamped in the root end. The principal axes of the beams may be rotated a prescribed angle relative to the rotor plane, and the stays are linear springs, connected to the free end of each beam. The masses are represented by concentrated masses in the free ends of the beams.

In view of the findings of the previous part, it was considered necessary to represent the following effects in the model:

1. Static coupling between the in-plane and out-of-plane stay systems. This is done by the rotation of the principal axes of the beams.

2. The effect on the blade eigenfrequencies of the centrifugal forces due to rotation. This is done by letting the centrifugal forces act on the deformed geometry of the model.

3. The effect of the blade coning angle.

4. The effect of in-plane offset of the blades. This is done by prescribing both translational and rotational offset of the blades.

The model as used for this analysis is symmetric, i.e. all blades are identical in mass and geometry. However, an extension of the analysis of a rotor that is unsymmetrical in both masses and

geometry (offset) is straightforward as is an extension to more than one element per blade.

The loads included in the analysis are those loads that are periodic with the rotor angular frequency of rotation. This means that the following loads are represented:

a. Wind load. The wind speed is prescribed as a speed, U_n, in hub height and a linear wind shear dU/dh. The wind is assumed to be a laminar flow parallel to the rotor axis.

b. Centrifugal forces. These forces cause axial and tangential displacements, if nonzero coning angle and in-plane offsets are prescribed.

c. Gravity forces.

d. Gyral forces caused by a constant yaw rate.

All these loads are deterministic loads, that are periodic with the rotor rotational frequency, and their phases relative to the rotor position are known. The previous part indicates that these loads are the most important on this specific wind turbine. The forces are calculated for the undeformed geometry, and all forces except the centrifugal forces act on the undeformed geometry.

Extension to additional stochastic loads prescribed by their spectra is straightforward. This is made possible by the technique adopted for the solution of the equations of motion. The stationary response for one rotor revolution is computed by means of the frequency response functions that also determine stochastic response for stochastic loads. Both structural and aerodynamic damping is represented.

The configuration of the structural model of the rotor is shown in Fig. 5.6a, and the rotation of the principal axes is shown in Fig. 5.6b. The wind is assumed to flow in the positive y direction. The principal system x_3y_3 is rotated the angle θ

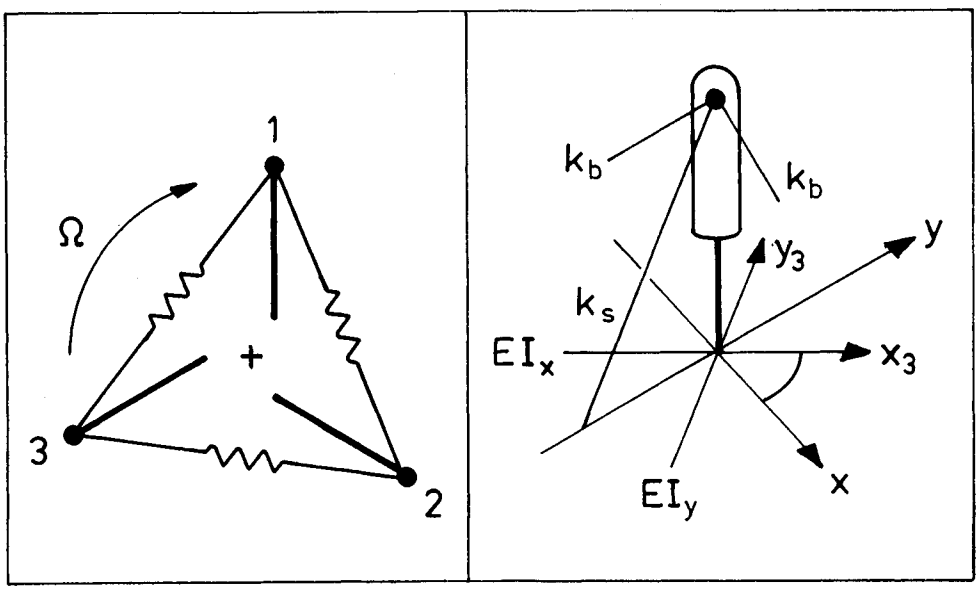

a. Rotor b. Blade

Fig. 5.6. Rotor model configuration.

counterclockwise from the rotor coordinate system xy. In Fig. 5.6b is furthermore shown a stay which with the stiffness k_s connects the mass m with a rigid point on the negative y-axis and 2 wires that with the stiffness k_w connects the mass with the masses on the two adjacent blades.

Denoting by S_{xy} the stiffness of the blade tip in direction x for a displacement in direction y, we find

$$S_{xx} = 3(EI_y\cos^2\theta + EI_x\sin^2\theta)/\ell$$

$$S_{yy} = 3(EI_y\sin^2\theta + EI_y\cos^2\theta)/\ell \qquad (5.2)$$

$$S_{xy} = 3(EI_x-EI_y)\sin\theta\cos\theta$$

where EI_x and EI_y are bending stiffnesses around the x and y axes, respectively.

Fig. 5.7 shows the forces acting on blade tip number 1. The forces are wind loads P_x and P_y, the centrifugal force C, the gravity force T, the gyral force G, the wire forces P_{12} and P_{13} and the stay force P_s. The stay and wires are assumed to be prestressed so that no slack occurs. The resulting equations of motion are shown in Fig. 5.8, and they are easily extended to

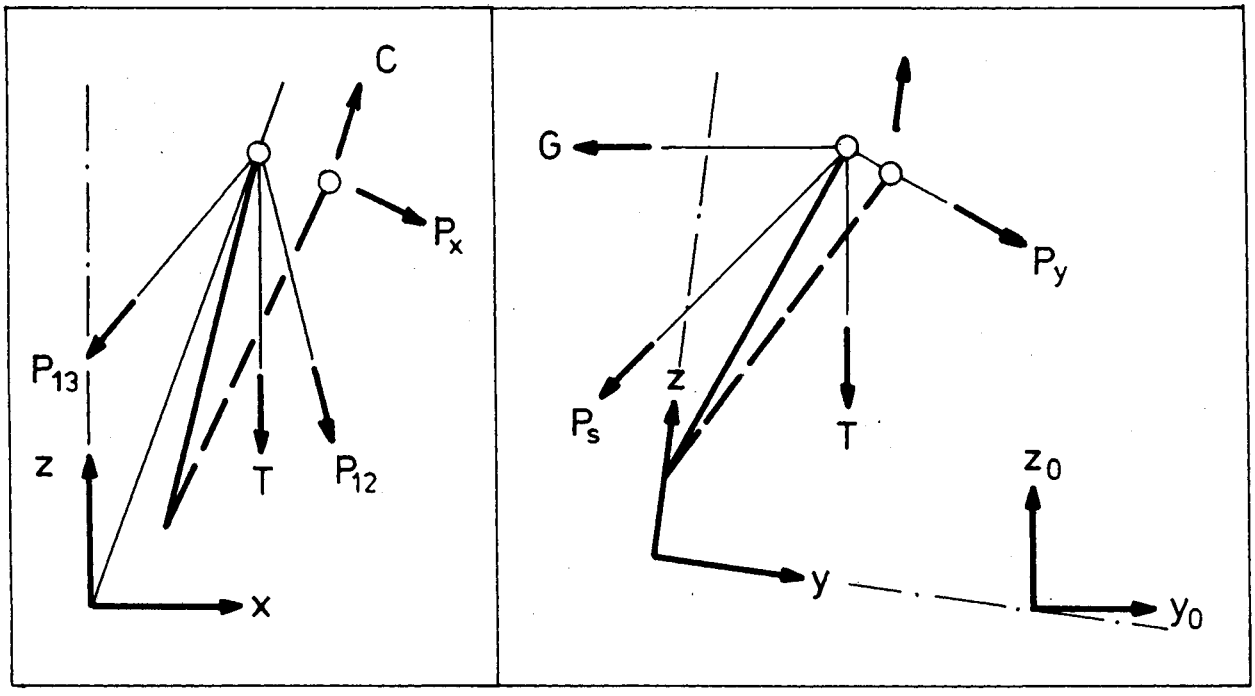

a. In-plane b. Out-of-plane

Fig. 5.7. Blade tip forces.

an unsymmetrical rotor by inserting values that are independent for each blade. The equations have the structure

$$\begin{Bmatrix} \underline{\underline{M}} & \underline{\underline{0}} \\ \underline{\underline{0}} & \underline{\underline{M}} \end{Bmatrix} \begin{Bmatrix} \ddot{\underline{u}} \\ \ddot{\underline{v}} \end{Bmatrix} + \begin{Bmatrix} \underline{\underline{K}}_{11} & \underline{\underline{K}}_{12} \\ \underline{\underline{K}}_{12} & \underline{\underline{K}}_{22} \end{Bmatrix} \begin{Bmatrix} \underline{u} \\ \underline{v} \end{Bmatrix} = \begin{Bmatrix} \underline{P}_x \\ \underline{P}_y \end{Bmatrix} + \begin{Bmatrix} \underline{\underline{C}}_x \\ \underline{\underline{C}}_y \end{Bmatrix} + \begin{Bmatrix} \underline{T}_x \\ \underline{T}_y \end{Bmatrix} + \begin{Bmatrix} \underline{\underline{0}} \\ G \end{Bmatrix}$$

where only $\underline{\underline{K}}_{11}$ is a full matrix, all other matrices are diagonal. The equations are coupled through the matrix $\underline{\underline{K}}_{12}$ that is $\underline{\underline{0}}$ if the angle θ to the principal axis is zero. The loads consist in principle of a constant part and a periodic part. Their phases relative to the rotor is shown in Fig. 5.8.

The equations of motions are solved in their complex form

$$\underline{\underline{m}}\,\ddot{\underline{Z}} + \underline{\underline{c}}\,\dot{\underline{Z}} + \underline{\underline{k}}\,\underline{Z} = \sum_{\ell}^{15} \underline{P}_{\ell} e^{i\Omega t} \qquad (5.4)$$

where lower and upper case symbols denote real and complex quantities, respectively. The complex solution $\underline{Z}$ is found for a periodic load that is the sum of 15 load cases $\underline{P}_{\ell}$, where each load case consists of one load type having one specific phase angle to the rotor. $\underline{P}_{\ell}$ being complex, the phase angle is represented by $\underline{P}_{\ell}$.

$$\begin{bmatrix} m & 0 & 0 & 0 & 0 & 0 \\ 0 & m & 0 & 0 & 0 & 0 \\ 0 & 0 & m & 0 & 0 & 0 \\ 0 & 0 & 0 & m & 0 & 0 \\ 0 & 0 & 0 & 0 & m & 0 \\ 0 & 0 & 0 & 0 & 0 & m \end{bmatrix} \begin{Bmatrix} \ddot{u}_1 \\ \ddot{u}_2 \\ \ddot{u}_3 \\ \ddot{v}_1 \\ \ddot{v}_2 \\ \ddot{v}_3 \end{Bmatrix} + \begin{bmatrix} k_x & -\frac{1}{4}k_w & -\frac{1}{4}k_w & S_{12} & 0 & 0 \\ -\frac{1}{4}k_w & k_x & -\frac{1}{4}k_w & 0 & S_{12} & 0 \\ -\frac{1}{4}k_w & -\frac{1}{4}k_w & k_x & 0 & 0 & S_{12} \\ S_{12} & 0 & 0 & k_y & 0 & 0 \\ 0 & S_{12} & 0 & 0 & k_y & 0 \\ 0 & 0 & S_{12} & 0 & 0 & k_y \end{bmatrix} \begin{Bmatrix} u_1 \\ u_2 \\ u_3 \\ v_1 \\ v_2 \\ v_3 \end{Bmatrix} =$$

$$\begin{Bmatrix} P_x \\ P_x \\ P_x \\ P_y \\ P_y \\ P_y \end{Bmatrix} + \Omega^2 Rm \begin{Bmatrix} \sin\delta_c \\ \sin\delta_c \\ \sin\delta_c \\ -v_o \\ -v_o \\ -v_o \end{Bmatrix} + mg \begin{Bmatrix} \sin(\Omega t+\phi) \\ \sin(\Omega t+\phi+\frac{2}{3}\pi) \\ \sin(\Omega t+\phi-\frac{2}{3}\pi) \\ \sin\gamma_g\cos(\Omega t+\phi) \\ \sin\gamma_g\cos(\Omega t+\phi+\frac{2}{3}\pi) \\ \sin\gamma_g\cos(\Omega t+\phi-\frac{2}{3}\pi) \end{Bmatrix}$$

$$-2m\Omega\omega R \begin{Bmatrix} 0 \\ 0 \\ 0 \\ \cos(\Omega t+\beta) \\ \cos(\Omega t+\beta+\frac{2}{3}\pi) \\ \cos(\Omega t+\beta-\frac{2}{3}\pi) \end{Bmatrix}$$

u_i = In plane displacement blade i

v_i = Out of plane displacement blade i

$k_x = \frac{1}{2}k_w + S_{11} + \Omega^2 Rm/\ell$

$k_y = k_g \sin^2\delta_g + S_{22} + \Omega^2 Rm/\ell$

δ_c = Angle from blade to centrifugal force

γ_g = Angle from blade to gravity force

ϕ = Phase angle for gravity forces

β = Phase angle for gyral forces

Fig. 5.8. Equations of motion for symmetric rotor. The in-plane and out-of-plane tip deflections are denoted u and v, respectively.

The stationary solution may be expressed by

$$\underline{Z} = \underline{\underline{H}}(\Omega) \sum_{\ell}^{15} \underline{P}_{\ell} e^{i\Omega t} \tag{5.5}$$

where $\underline{\underline{H}}(\Omega)$ is the frequency response matrix. Using this representation an extension to stochastic loads is straightforward. The actual solution is the real part of $\underline{Z}$

$$\begin{Bmatrix} \underline{u} \\ \underline{v} \end{Bmatrix} = \mathrm{Re}(\underline{Z}) \ . \tag{5.6}$$

Due to the simplicity of the structural representation of the rotor, the absolute values of the results may not be correct. However, as already mentioned the model as it is programmed at present may in a straightforward manner be extended to a more detailed representation, and it is expected to give qualitatively valid answers concerning the effects of various parameters and load types and the effects of their variation. Furthermore, the model has a potential for extension to further development of both structural representation and load types of deterministic and stochastic nature, and this potential is easy and straightforward to bring in use.

Comparison of measured and computed results

A series of calculations of one rotor revolution has been made, in which the angle to the blade principal axis and the stiffness of the in-plane wires have been varied. The actual model used in the calculations was established on basis of known rotor frequencies in the following way:

The flapwise and edgewise fundamental eigenfrequencies for one blade without stays was determined during the laboratory tests, Ref. 5.2, as approx. 1.55 and 2.40 Hz, respectively, and the tip deflections due to a concentrated load in the tip were measured. From this the effective bending stiffness and the effective concentrated mass are determined.

The effective stiffness of the out-of-plane stay is then determined on basis of the flapwise eigenfrequency of the stayed blade. The frequency is known to be approx. 9 Hz from the field measurements, Ref. 5.1, and results from the detailed finite element model described in Appendix II and Ref. 5.4.

The effective stiffness of the in-plane wires cannot be determined in advance because of the unknown flexibility of the mechanisms used for adjusting the prestressing of the wires. Instead the stiffness of a wire without adjusting mechanisms are adopted as a reference. The effective wire stiffness and the angle to the blade principal axes are then determined by comparing the results from the parametric study with measured results. Fig. 5.9 shows the data for the reference rotor model.

ROTOR DATA:

R	RADIUS TO MASS	1.20E+01
BL	BLADE LENGTH	1.10E+01
RO	RADIAL OFFSET	1.00E+00
TO	TANGENTIAL OFFSET	1.80E-01
AT	AXIAL TILT	0.
TT	TANGENTIAL TILT	0.
SS	STAY STIFFNESS	1.85E+07
WS	WIRE STIFFNESS	5.00E+05
CM	CONCENTRATED MASS	4.53E+02
EIX	BENDING STIFFNESS	1.94E+07
EIY	BENDING STIFFNESS	4.72E+07
DC	ANGLE CENTR FORCE	1.50E-02
DS	ANGLE TO STAY	2.73E-01
BE	ANGLE TO MASS	1.50E-02

GA	ANGLE BLADE/VERTICAL	1.05E-01
PA	ANGLE TO PRINCIPAL AXIS	2.62E-01
TA	TILT OF AXIS	1.05E-01
OMR	ROTATIONAL ANGULAR VELOC	3.14E+00
OMY	YAW ANGULAR VELOC	1.16E-02
VN	WIND SPEED HUB HEIGTH	1.07E+01
DVN	WIND SHEAR GRADIENT	1.11E-01
XIS	PERCENT CRIT. DAMP.	5.00E-03

DETERMINISTIC LOADCASES	ACTIVE BLADE	1	2	3
01-03	WIND LOAD	1	1	1
04-06	CENTRIFUGAL FORCES	1	1	1
07-09	GRAVITY FORCES IN PLANE	1	1	1
10-12	GRAVITY FORCES OUT OF PLANE	1	1	1
13-15	GYRAL FORCES	1	1	1

Fig. 5.9. Printout listing the reference rotor model data.

The parameters to be varied are denoted θ (the angle from the rotor plane to the principal axes) and f_w (the ratio actual wire stiffness/reference wire stiffness). In Fig. 5.10 the calculated rotor frequencies are shown as functions of f_w. These results are almost independent of θ, and they indicate a wire stiffness of only 5% of that of a solid wire. The adjusting mechanisms seem to be decisive for the effective wire stiffness and to have a strong influence on the in-plane rotor behaviour. This is also apparent from Fig. 5.11 that shows the calculated ratio f between static average response of the edgewise driving moment M_y and the dynamic amplitude for varying f_w. Both f and 1/f are shown, and average values for a number of revolutions are shown as well. Again a value for f_w of approx. 0.05 is indicated, and the values of f are not strongly dependent on θ.

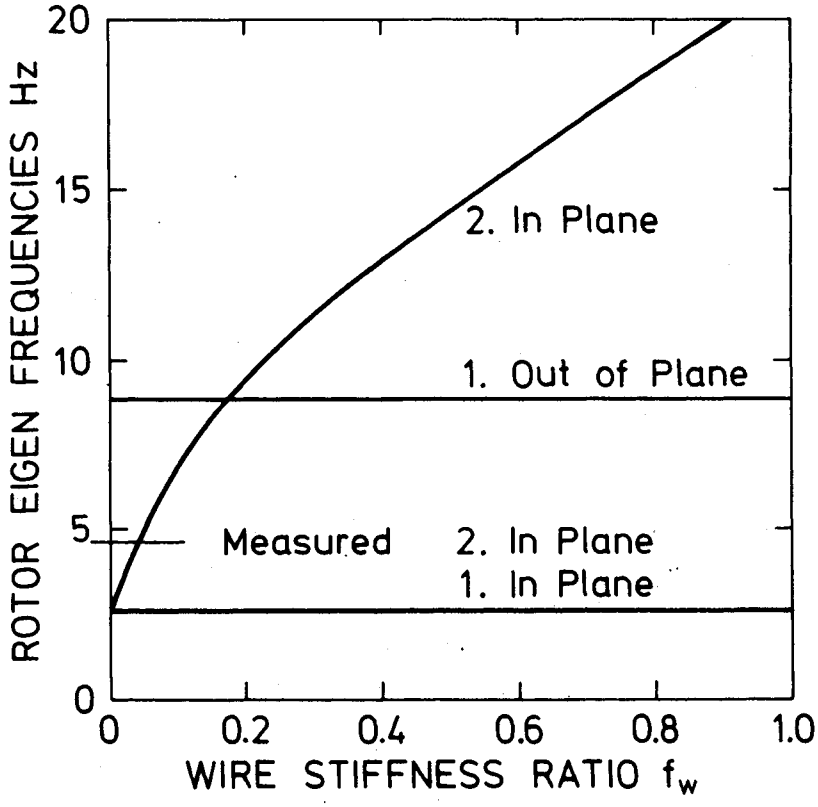

Fig. 5.10. Eigenfrequencies versus the ratio f_w.

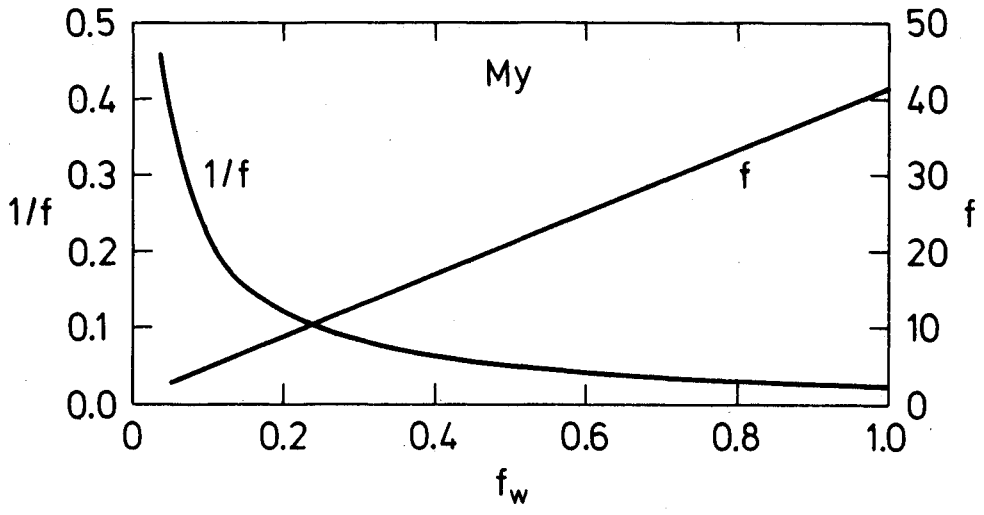

Fig. 5.11. Ratio f static average/dyn. amplitude for the edgewise driving moment. θ = 0 deg.

The dependence on θ is very pronounced for the out-of-plane bending moment M31 as shown in Fig. 5.12. This is due to the out-of-plane stay that through the force NYS keeps the tip in mostly in-plane deformations. This causes the static average to change sign at about θ = 5 deg.

The other forces shown do not depend strongly on θ, and therefore Fig. 5.12 indicates an effective angle θ of approx. 15 deg. to the principal axes. The ratio f for the in-plane wire forces NYB expresses the ratio between the dynamic amplitude of the driving moment and the corresponding contribution from the dynamic amplitude of NYB. The computed static average of NYB is zero.

The figures 5.10 to 5.12 show that the stays and wires to a large extent determine the overall rotor response, and that the stiffness properties of the blade itself is of minor importance except for the magnitude of the out-of-plane bending moment M31. However, due to the stay this moment is of a small magnitude.

The measured values shown in these figures for comparison with the calculated ones are the averaged values for blade 2 and

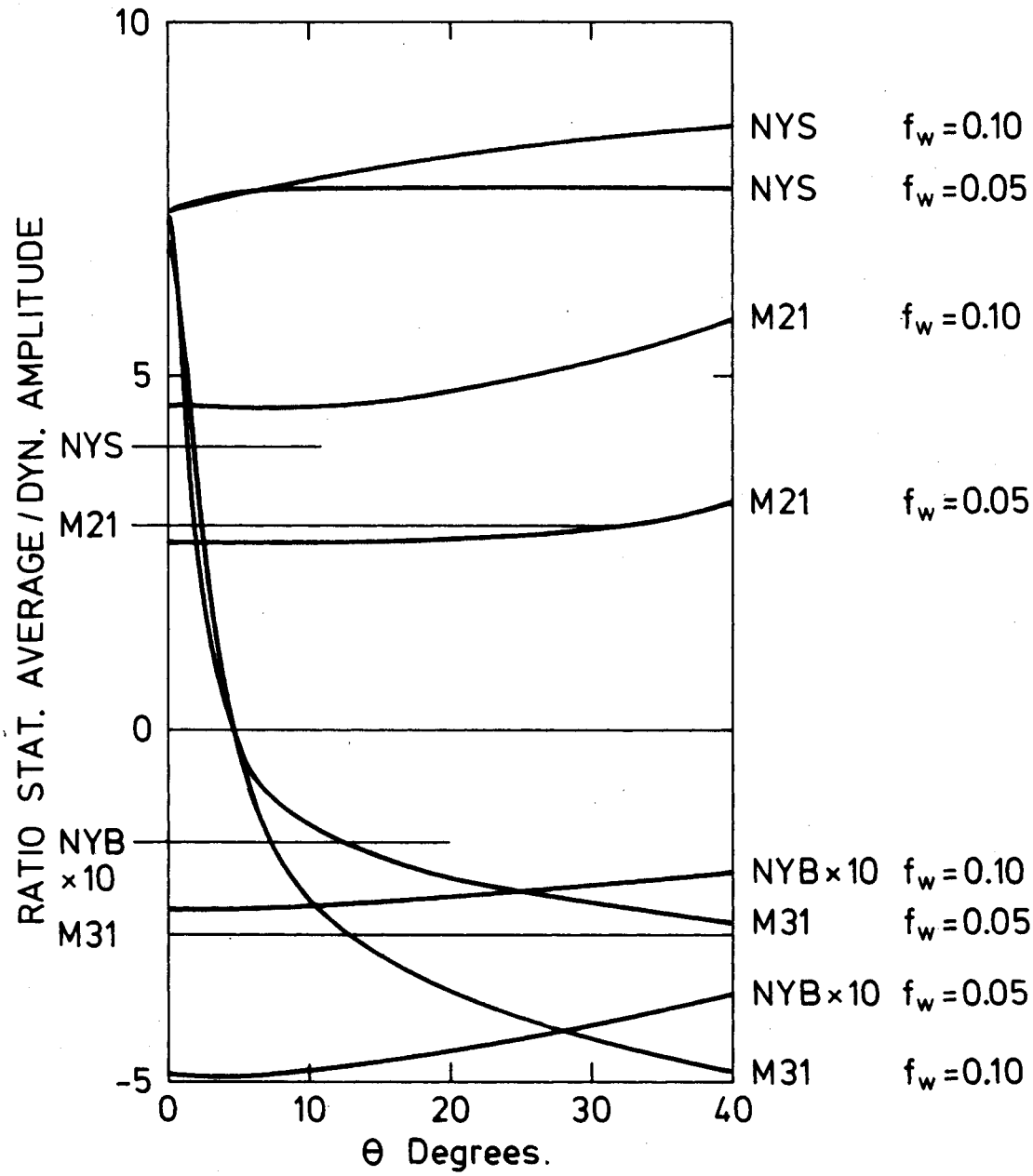

Fig. 5.12. Calculated values of the ratio f for forces and moments in the rotor. The ratio f for the forces NYB in the in-plane wires is explained in the text. Measured values are indicated by thin lines.

blade 3 during 75 revolutions of run 17. The figures 5.13 and 5.14 show the time histories during one averaged revolution of that period for blade 3. Fig. 5.15 shows wind speed and yaw rate during the same 75 revolutions.

Using the values $f_w = 0.05$ and $\theta = 15$ deg. a series of calculations were made in order to check the agreement with the measured results and to estimate the relative importance of the four rotor synchroneous loads indicated in Fig. 5.9.

The computed results are plotted in the figures 5.13 and 5.14. For the in-plane moment and wire force the sinusoidal shape inherent in the calculated response agrees with the measured response, while there are some disagreement in the phase of the response. This most probably is due to unsymmetries in the Gedser rotor. For the out-of-plane moment and stay force the computed sinusoidal response does not agree too well with the measured response that in addition to the period 1P shows the period 3P as well. The disagreement in phase due to unsymmetries is also present. As seen from Fig. 5.15 the wind speed does - as expected - not show any periodicy, while the yaw rate has the 3P period in phase with that of Fig. 5.14.

The 3P period cannot, however, be induced by forces or movements with period 1P. In a linear system such loads will give response with period 1P. It can be seen from Figs. 5.16 and 5.17 that the 3P period is more pronounced during forced jaw, although the yaw rate is fairly constant. During forced yaw of an unsymmetric 3-bladed rotor, the gyral forces may induce 3P response, but in stationary operation in the wind the 3P response may be amplified by coupling to the yaw movements in the slack of the yaw mechanism, but the driving forces must be wind forces, originating from either a nonlinear wind shear or from stagnation of the flow in front of the tower. This will cause a 3P response of moments and stay forces, but an excitation of a 3P jaw moment requires furthermore lack of symmetry either in the aerodynamic properties of the blades or in the effect of the flow stagnation. These effects cannot at present be represented by the model, but they should be included in order to

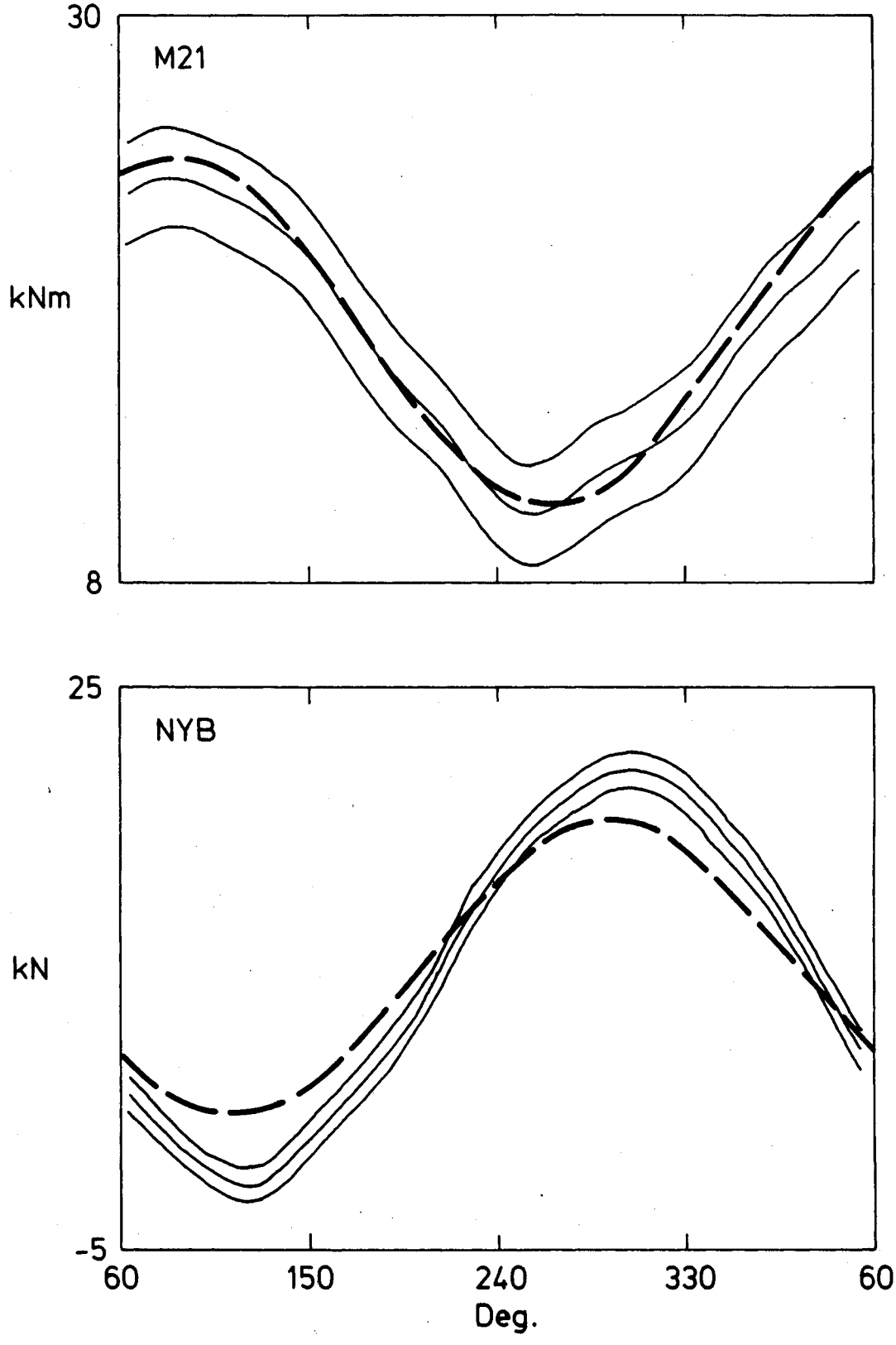

Fig. 5.13. Measured moment M21 and wire force NYB for 75 revolutions in the wind. Average and RMS values. Calculated values shown by dashed lines.

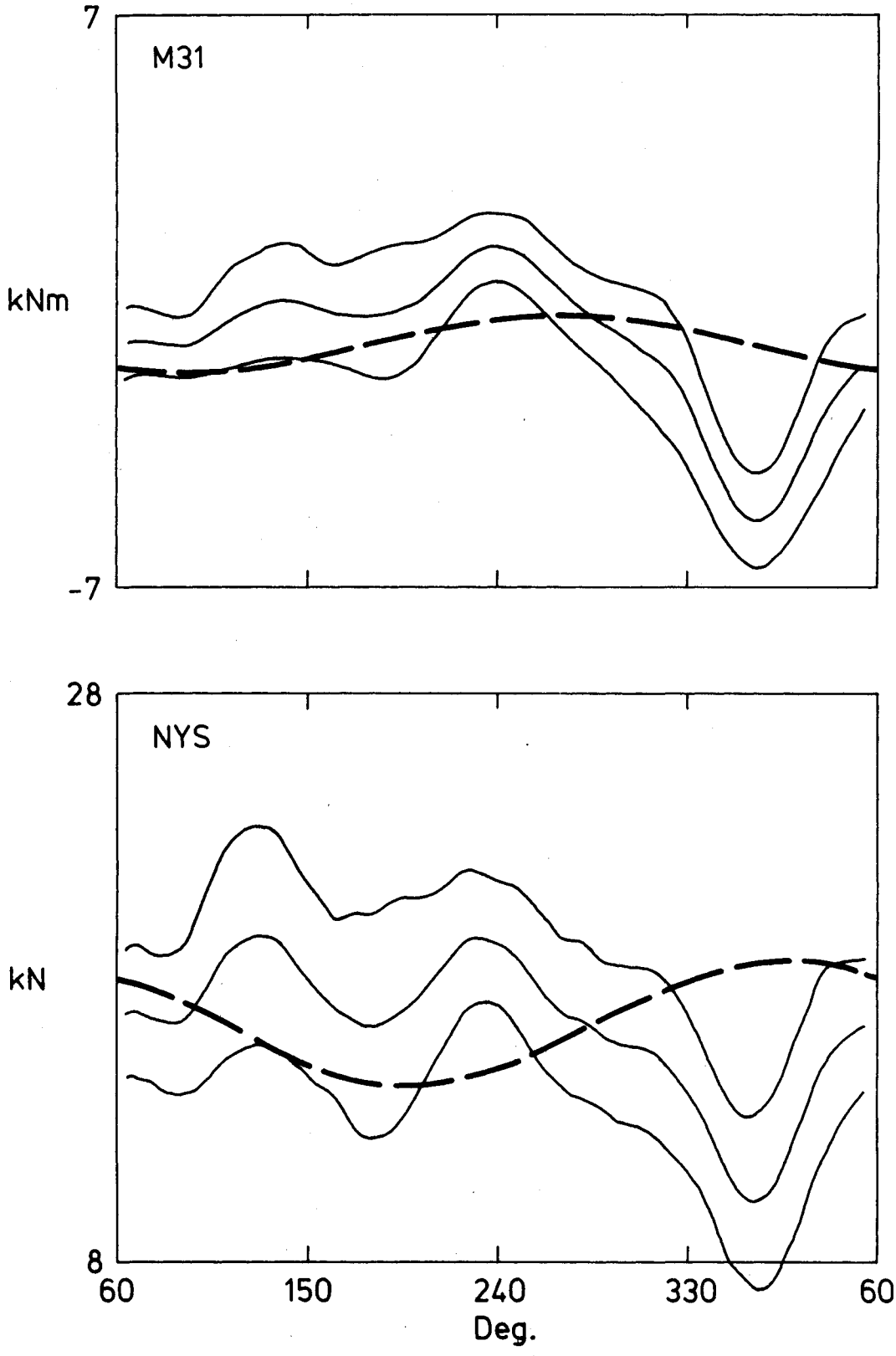

Fig. 5.14. Measured moment M31 and stay force NYS for 75 revolutions in the wind. Average and RMS values. Calculated values shown by dashed lines.

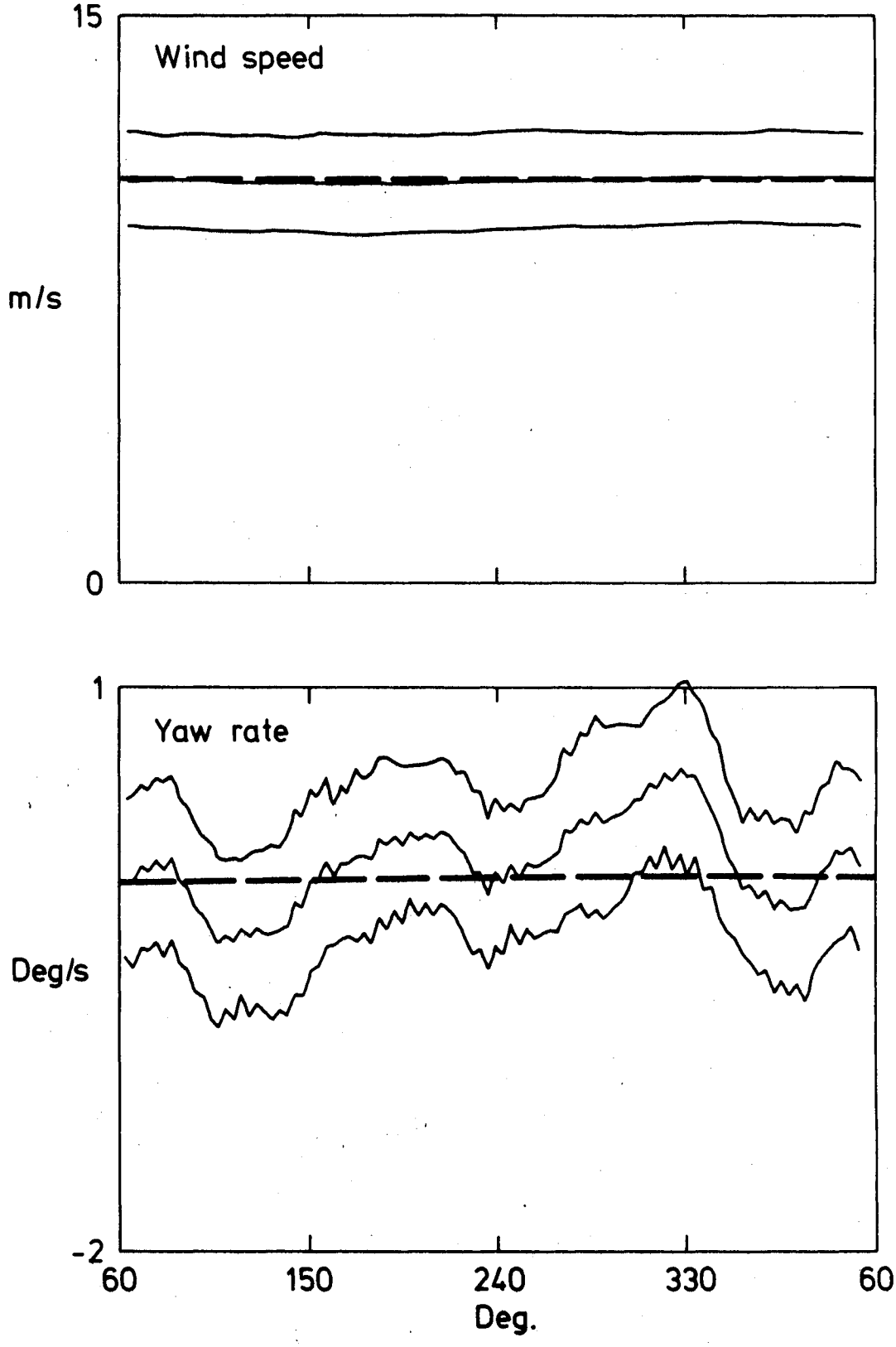

Fig. 5.15. Wind speed and yaw rate for 75 revolutions in the wind. Average and RMS values.

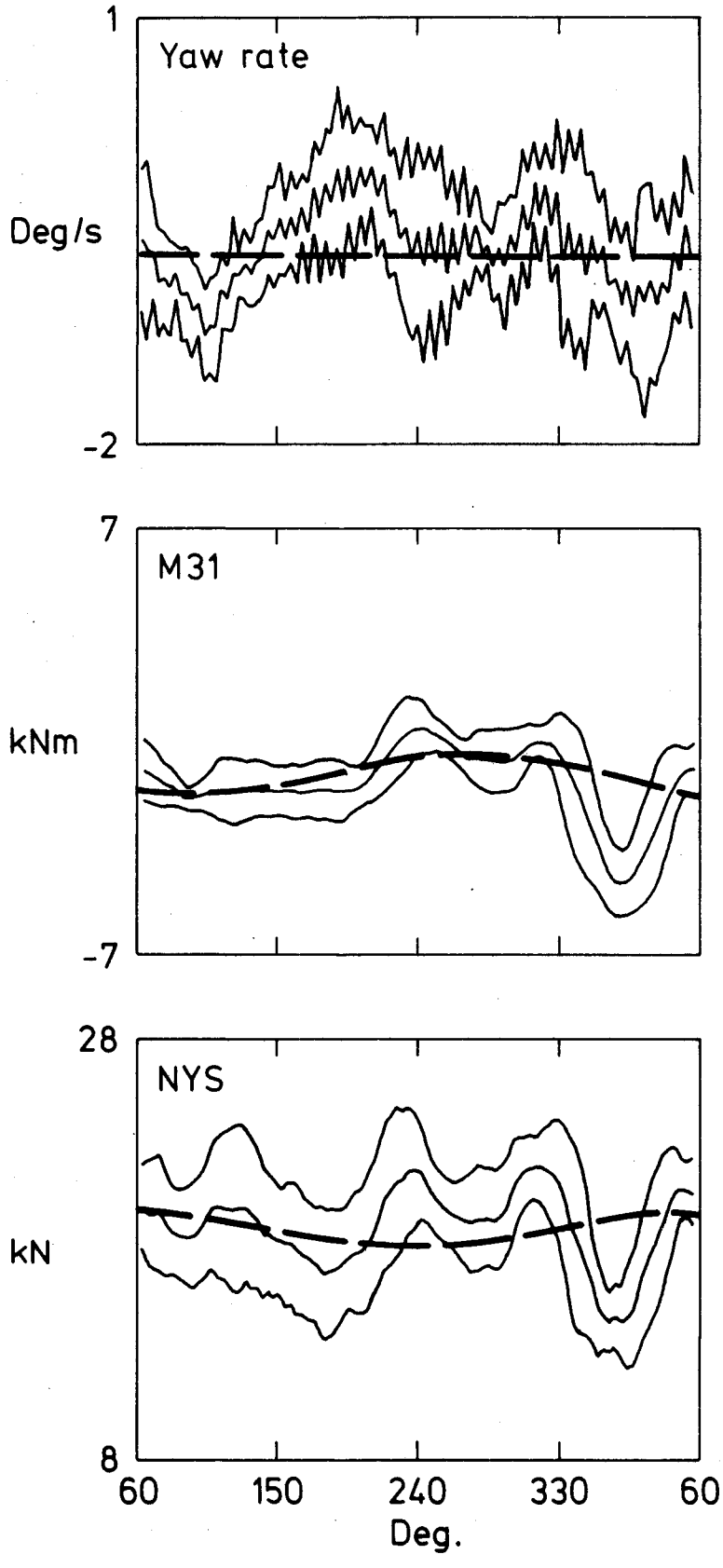

Fig. 5.16. Measured yaw rate, out-of-plane moment and stay forces during 5 revolutions during forced yaw. Average and RMS. Calculated response shown by dashed lines.

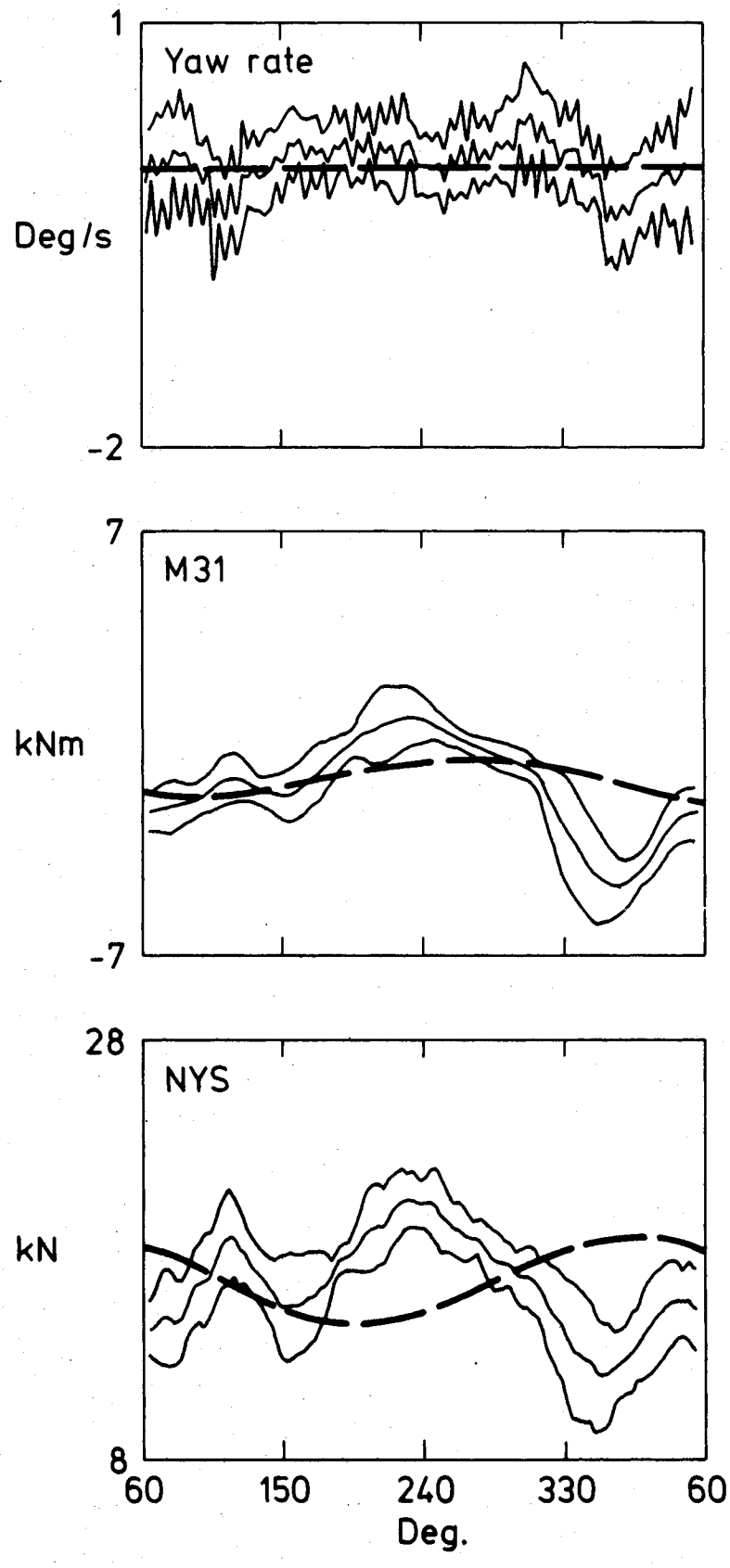

Fig. 5.17. Measured yaw rate, out-of-plane moment and stay force during 5 revolutions in the wind. Average and RMS. Calculated response shown with dashed lines.

represent the frequency content of the out-of-plane signals.

The significance of each load type is illustrated in Table 5.3 that lists calculated representative response relative to the most important contribution. The response for all load types acting together may be different from the sum of each contribution, because they do not act in phase with each other. This explains why it is difficult to extract the effect of gyral forces from the measured response. Table 5.3 indicates that the gyral forces during forced yaw induce oscillating movements of the same order of magnitude as the wind shear. This corresponds to the significantly different shape of the response with and without forced jaw, Figs. 5.16 and 5.17.

	M21		M31		NYS		NYB
	Stat.	Dyn.	Stat.	Dyn.	Stat.	Dyn.	Dyn.
Wind load	1.000	0.058	1.000	0.126	1.000	0.993	0.074
Centrifugal forces	0.435	0.000	0.643	0.000	0.042	0.000	0.000
Gravity forces	0.000	1.000	0.067	1.000	0.126	0.186	1.000
Gyral forces	0.000	0.015	0.000	0.203	0.000	1.000	0.001
All forces	1.433	1.003	1.578	1.003	1.167	0.916	1.000

Table 5.3. Calculated relative loads $\theta = 15^{\circ}$, $f_w = 0.05$, $v_n = 10.7$ m/s, yaw rate = 0.0116 rad/sec.

Conclusions

The static forces in the rotor are primarily due to the wind loads, but significant contributions to the bending moments are due to centrifugal forces acting through a radial offset of the blades.

Gravity forces are the main source for the oscillating part of both in-plane and out-of-plane bending moments and the in-plane wires. The gravity forces are transferred to the out-of-plane moment via the outer stay force because of the rotation of the principal axes of the blades. Wind shear and gyral forces during forced jaw seem to contribute equally to the oscillating part of the outer stay forces, but because of their different phase they do not add their amplitudes in the resulting total response.

In addition to the forces with period 1P, forces with period 3P are apparent in the out-of-plane response. The 1P and 3P deterministic forces seem to account for most of the energy in the response. The stochastic part of the load does not seem to dominate the response, except that the response at rotor eigenfrequencies may be partly excited by stochastic loads, the other source possibly being the higher harmonics in loads due to flow stagnation before the tower. The most important effect of stochastic wind variations may be the change of quasi static average loads due to low frequency wind variations.

The stay system connected to the blade tips are very important in determining the rotor response and in keeping the stresses low. The in-plane wires drastically reduce the oscillating part of the in-plane bending moment, although their adjusting mechanisms seem to reduce their stiffness to 5% compared to a solid wire. The out-of-plane stays keep the out-of-plane tip movements very small. This has a significant influence on the out-of-plane bending moment, and the small tip movements very much reduce the possibility of stall induced oscillations as well as couplings to the yaw movements.

The simple rotor model described in this chapter has, based on a frequency domain technique, given time histories that has served three purposes. It has identified the effective values of wire stiffnesses and angle to the principal axes, it has explained some significant mechanisms in the rotor assembly, and it has indicated the relative importance of the four deterministic, rotor synchroneous load types considered. There are, how-

ever, needs for improvements, and they are listed below:

- The addition of spectral input, at first restricted to the diagonal terms in the spectral matrix. It should be combined with a simple routine based on a linear damage accumulation law.

- The inclusion of higher harmonics of the rotational frequency of the rotor in the description of the wind load, thereby allowing for nonlinear wind shear and flow stagnation in front of the tower.

- The modification of the structural model by adding one or more nodes to each blade. This will improve the absolute values of the results. At this stage it will be natural to include the capability of analysing unsymmetric structures by allowing for different properties to be prescribed for each rotor component.

- The addition of off-diagonal terms in the spectral matrix, thus including the cross correlation of the wind field.

This priority seems appropriate in view of the primary feature of the model being its capability to combine stationary deterministic loads with stochastic loads in a frequency domain formulation.

REFERENCES

5.1. P. Lundsager, C.J. Christensen and S. Frandsen, The measurements on the Gedser Wind Mill 1977-79, Gedser test group 771.105-3, The wind power program of the Ministry of Commerce and the Electric Utilities in Denmark (Nov. 1979).

5.2. V. Askegaard, C. Dyrbye, S. Gravesen, Laboratory Tests on the Gedser Wind Turbines Blades. Technical University of Denmark, Report S28/77. November 1977.

5.3. P. Lundsager, SECTIO-A program for the determination of cross sectional properties of closed thin walled beams. Risø-M-2159, July 1979.

5.4. P. Lundsager, C.J. Christensen, Investigations of Structural Dynamics on the Gedser WTG and on New Danish Windmills. Risø-M-2146, December 1978.

6. COMPARISON OF THE CHARACTERISTICS OF THE GEDSER WIND TURBINE WITH THREE NEW DESIGNS

Survey of the design characteristics

In this chapter three horizontal-axis, propeller type wind turbines will be compared with the 23-year-old Gedser wind turbine. The three other turbines are: 1) one of the two turbines built by the Danish Ministry of Energy and the Electric Utility Companies, 2) the so-called "Mod-OA" built by the USA Department of Energy (ERDA) and 3) the wind turbine erected at Kalkugnen by the National Swedish Board for Energy Source Development. The turbines are shown in Figs. 6.1-6.4.

Although the turbines are basically alike, there are some differences which should be noted. The two Danish turbines have their rotors upwind and they are three-bladed, while the US and the Swedish turbines have 2 blades and the rotor downwind of the tower. The main advantage of a downwind rotor is that in principle yaw control is not needed. On the other hand, operating the rotor upwind eliminates the effects that arise when the blades pass through the tower shadow.

The Gedser turbine - like the Nibe turbines - has three blades. For a three-bladed rotor the moment of mass inertia around a vertical axis is independent of the angular position of the rotor and therefore the gyral forces do not oscillate. This is not true for the two-bladed turbine where the gyral forces are not constant even at constant yaw rate. This is some of the price for saving one blade. Furthermore, using 3 blades also provides the possibility of stiffening the rotor structure with stays, which has been done on the Gedser turbine with great success. The stays and wires are probably the basic reason that the turbine rotor survived 10 years of continuous operation without meeting ultimate load or fatigue problems.

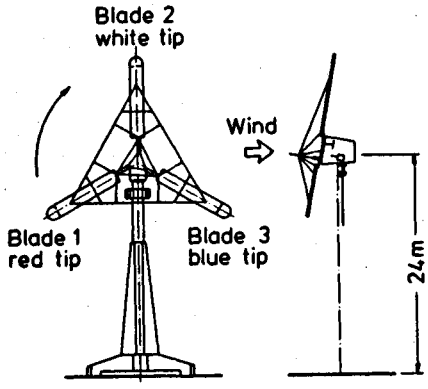

Fig. 6.1. Gedser

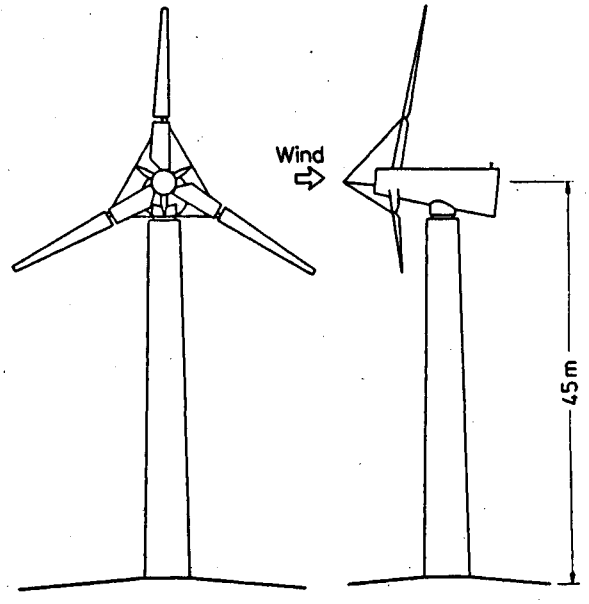

Fig. 6.2. Nibe A.

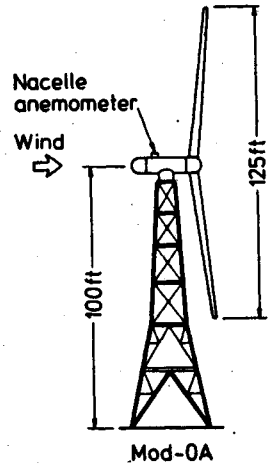

Fig. 6.3. Mod-0A.

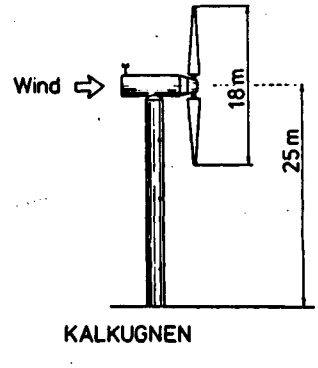

Fig. 6.4. Kalkugnen.

All figures: Scale 1:850.

Turbine	Hub height (m)	Rotor diameter (m)	Rated power (kW)	No. of blades Downwind/ upwind	Rotor area (m^2)	Maximum power coeffi-cient	Wind speed correspond. to max. power coef-ficient (m/s)	Rotor frequency (rpm)	Overspeed regulation	Blade profiles	Blade materials	Tip speed ratio at maximum power efficient X
Gedser	24	24	200	$\frac{3}{\text{upwind}}$	452	0.32	8.5	$\frac{\text{speed fixed}}{30}$	stall	Clark Y	steel and wood	4.4
Nibe A	45	40	630	$\frac{3}{\text{upwind}}$	1257	0.29	11.0	$\frac{\text{speed fixed}}{33}$	stall	NACA 44 series	reinforced fibre glass	6.3
MOD-O	30.5	38	100	$\frac{2}{\text{downwind}}$	1134	0.33	7.5	$\frac{\text{fixed speed}}{40}$	pitch	—	aluminium	10.6
Kalkugnen	25	18	60 (75)	$\frac{2}{\text{downwind}}$	254	0.32	9.5	$\frac{\text{fixed speed}}{76}$	pitch "feather-ing"	NACA 64_3-618	aluminium	7.5

Table 6.1. Data for the four turbines.

During the 20 years, which separate the Gedser turbine from the three other designs, a general development in technology has taken place. The Gedser turbine is operated at constant pitch angle and overload of the generator is avoided by so-called stall regulation, i.e. when a certain wind speed is exceeded the entire blade will be stalled. Under extreme wind conditions or after failures that cause nacelle vibrations, a mechanical device will release the braking flaps. On modern designs the operational strategy is very often controlled by microprocessors, whose versatility allows a rather free choice of yaw control mode, start-up and shut-down procedures etc. The Mod-OA and the Kalkugnen turbines are equipped with a continuous pitch angle control while the Nibe-A turbine has a stepwise pitch control, though the overload control is based on stalling of the airfoil flow as is the case for the Gedser turbine.

The main spar of the blades on the Gedser wind turbine is made of steel (Fig. 1.5), the ribs of wood, which are covered with aluminium plates. Mod-O and Kalkugnen are supplied with aluminium blades and Nibe-A has fibre glass reinforced plastic blades. The inner 8 m of the blades have load carrying beams of steel.

All four turbines, except for the Mod-O, have concrete towers. Table 6.1 gives a survey of the data for the turbines.

Blade bending moments and stresses

In this section some time histories for the blade root bending moments in the four turbines are compared. For the Nibe-A turbine, the moments at the root of the outer blade are shown. The edgewise and flapwise moments are shown in Fig. 6.5 and Fig. 6.6, respectively. They are given in a dimensionless form as the ratio between the moment at a given rotor position and the average moment over one revolution. The curves are taken from Refs. 6.1 to 6.4, and they correspond to the following percentages of full power:

Gedser	36% of full power
Nibe A	30% of full power
Mod-O	100% of full power
Kalkugnen	45% of full power

The curves for Gedser and Mod-O are averages of several revolutions, while the curves for Kalkugnen and Nibe A are based on one revolution. Blade position 0 degrees corresponds to the blade pointing vertically downwards.

By measuring the oscillating part of the moments by their constant part, one obtains an indication of the degree of smoothness of each turbine as compared to the others, whereas the curves do not indicate the magnitude of the forces of one turbine relative to the others. The curves that are based on several revolutions are smoother than those based on one single revolution, since random excitations to some extent are averaged out of the signals.

The pattern of the edgewise moment of the Gedser turbine is clearly different from the patterns of the three other turbines, which have patterns that are much alike. The average driving moment of the Gedser turbine is rather large, and it is made even larger by the in-plane offset of the blades. The moment amplitudes are kept low by the in-plane wire system, and therefore the dimensionless moment is almost constant over one revolution. The three other turbines have cantilevered blades (the Nibe A moment is measured just outside the stays), and in spite of the otherwise rather different designs the dimensionless moment amplitudes are similar. The Nibe A and Mod-O patterns are very close to each other, having a dominant oscillation due to gravity forces. This is also apparent for the Kalkugnen, but the moment is superposed by a 5P oscillation, that is not negligible. It is suggested in Ref. 6.3 that the 5P oscillation may be caused by a flexibility of the machinery supports, and it therefore seems to be a special feature of the

Kalkugnen turbine. The patterns of the edgewise moments in the Nibe A and the Mod-O turbines therefore most probably should be taken as typical for cantilevered two- or three-bladed rotors, and the significance of the in-plane stay system appears from a comparison with the Gedser curve.

The patterns of the flapwise bending moments differ notably from the edgewise moments. The moment in the Gedser turbine is not particularly smooth, but because of the out-of-plane stays

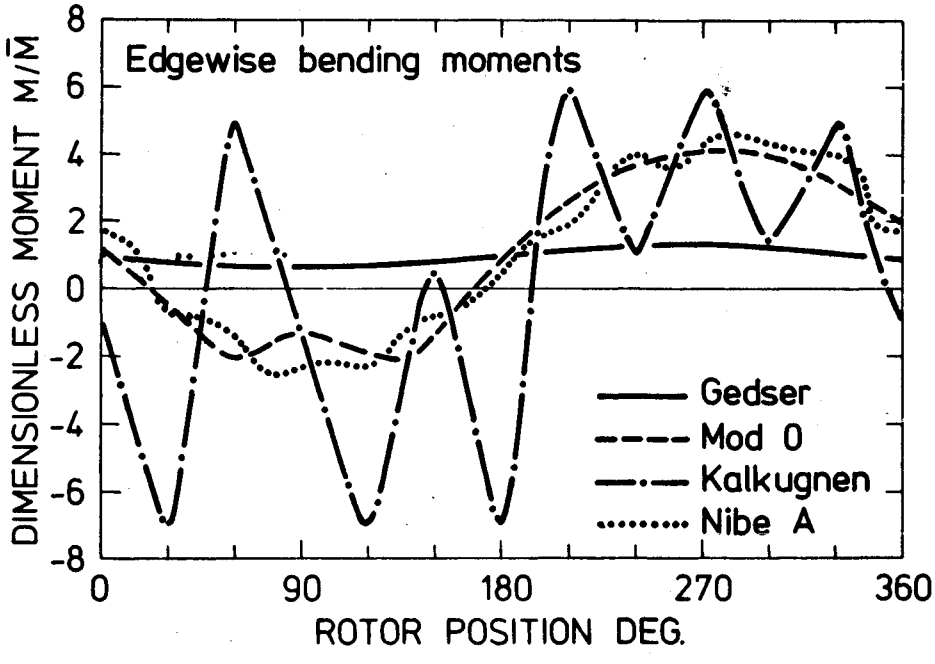

Fig. 6.5. Edgewise bending moments.

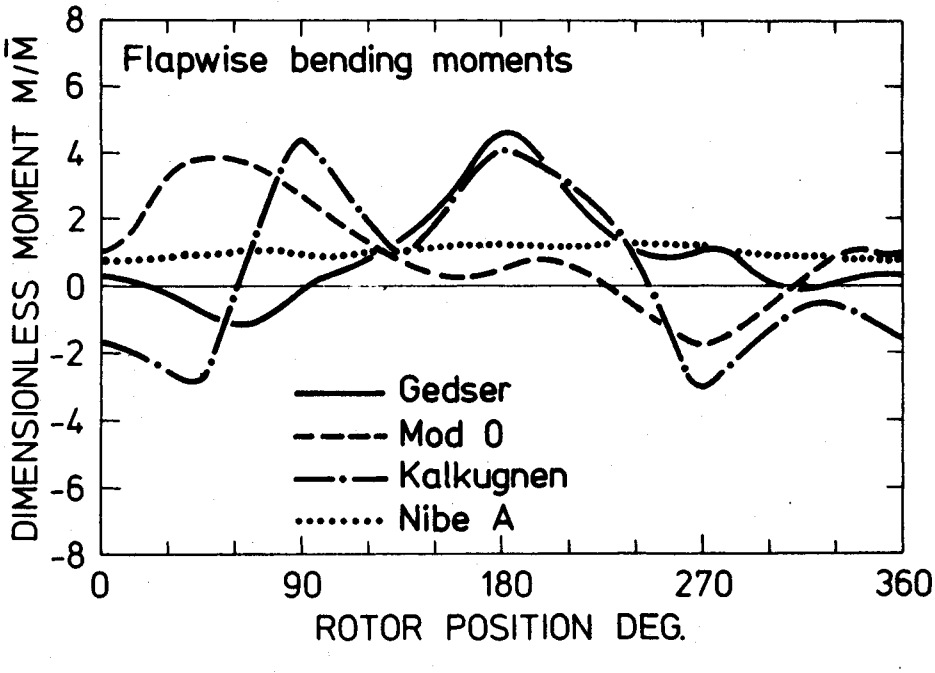

Fig. 6.6. Flapwise bending moment.

the average flapwise moment has a very small magnitude, and the curve therefore corresponds to small moment amplitudes. The pattern closest to the Gedser moment is that of the Kalkugnen turbine, but since Ref. 6.3 gives the results as strains and not moments, nothing can be said about the magnitude of the average moment. The average moments in the Nibe A and the Mod-O are an order of magnitude larger than the Gedser turbine, and they therefore experience significantly larger moment variations. Due to different coning angles and power output the average moment of the Nibe A is 6 times larger than that of the Mod-O, but the moment variations of the Nibe A are the smallest. This is most probably due to the effects of tower wake and nacelle motions on the Mod-O, but effects of flow stagnation and nacelle motions may be seen in the flapwise moments of both the Nibe A and the Gedser turbines.

Stress results for the Mod-O turbine have not been found, but stresses in the Kalkugnen may be derived from the strain results of Ref. 6.3. Stress results are available for the Gedser and the Nibe A turbines. The stress patterns are shown in Fig. 6.7 and Fig. 6.8 where the stresses in the Kalkugnen turbine have been computed assuming a uniaxial stress state in steel.

The stresses due to edgewise bending in the three turbines, all operating at a comparable percentage of rated power, have amplitudes of the order of ± 6 MN/m^2 to ± 28 MN/m^2, the Gedser turbine having the lowest stress amplitudes.

The stresses due to flapwise bending differ somewhat more than the edgewise stresses. While having amplitudes of the order of ± 4 MN/m^2 to ± 14, the average stresses cover the range ~ 5 MN/m^2 to ~ 55 MN/m^2. Again the Gedser turbine has the lowest stresses.

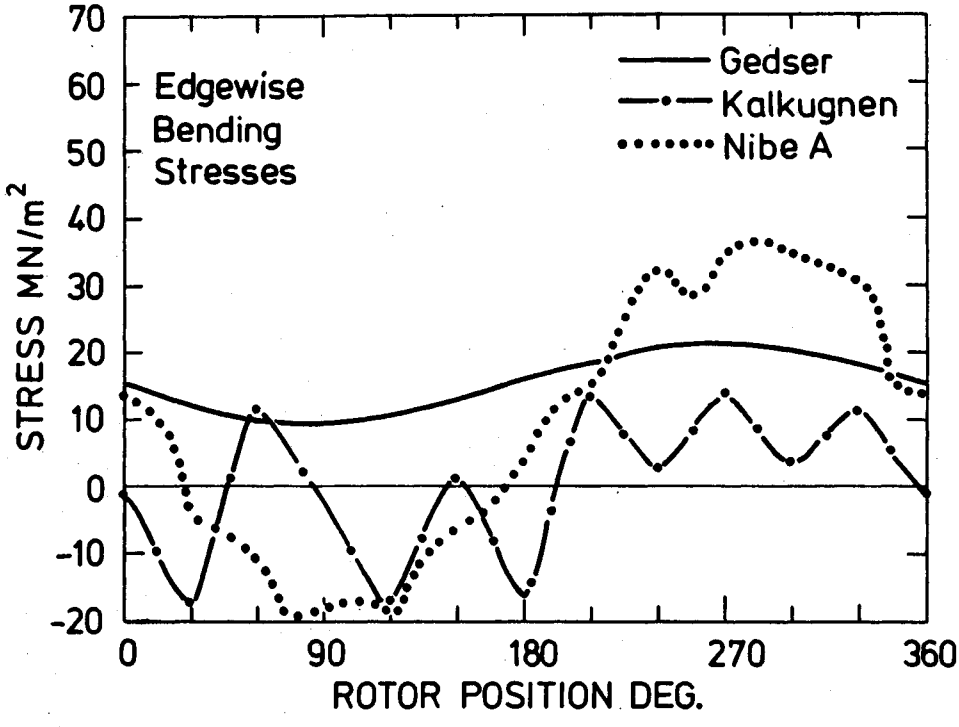

Fig. 6.7. Edgewise bending stress.

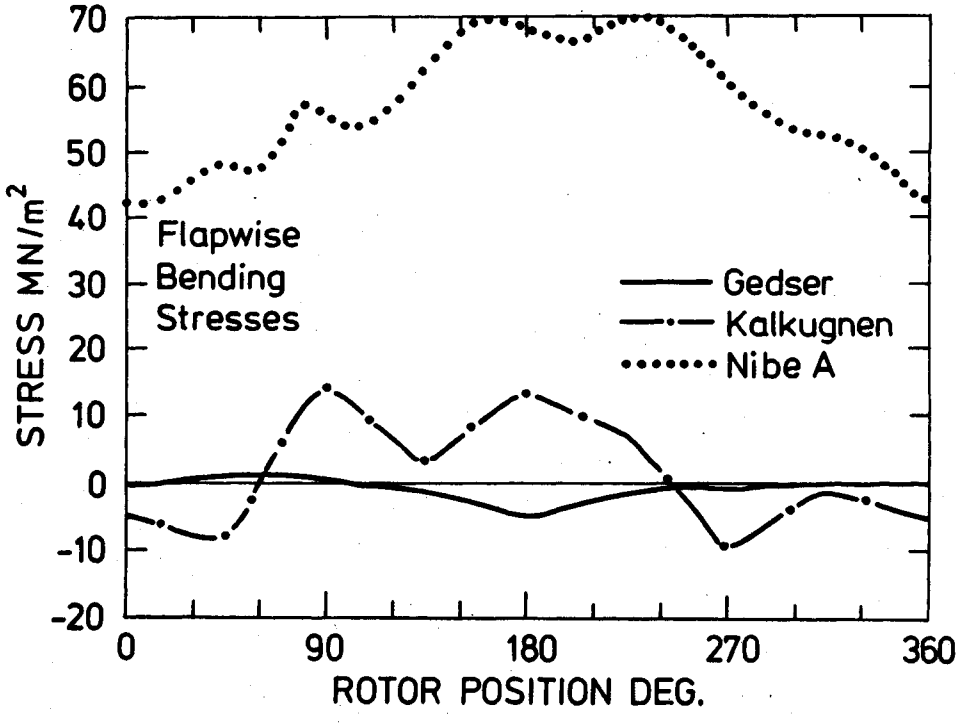

Fig. 6.8. Flapwise bending stress.

Performance

Because of the lack of standards for performance testing, problems arise when different turbines are compared. The data we have available for the power curve comparison in Fig. 6.9 were derived in very different ways. The power curve for the Gedser turbine is the result of linear regression on the data points (10-min. ave.) as described in Chapter 2 and Ref. 6.1. The Kalkugnen power curve was also produced by means of regression (though the data were averaged over 1 min. and fitted to a polynominum of higher order), Ref. 6.3. The power curves for the Mod-OA and Nibe A were derived quite differently. The curve for Nibe A by manual fitting in an x-y plot (2-min. floating averaging) of electric power vs. wind speed at 58 m. On the basis of this result the curve shown in Fig. 6.7 was derived by estimating the wind speed at hub height (45 m), assuming a logarithmic wind profile. Finally, the power characteristics for the Mod-OA was taken from Ref. 6.2A, where a regression analysis is presented. The power curve for the Mod-OA was measured using an anemometer mounted on top of the nacelle and then correcting the wind speed to the "free stream" wind speed.

Table 6.1 showed that the turbines are very different in rotor size and rated power, as is also clearly seen in Fig. 6.9. Another difference is the start-up wind speed, which varies by app. ±25%. This reflects a decision by the designer based on his expectations to the local frequency distribution of wind speed.

Fig. 6.10 also shows the power curves, but with electric power normalized to 1 m^2, so that the size is eliminated for the comparison of turbines of different magnitude. In this representation it is seen that the power curves qualitatively are very much alike.

As a good approximation over a fairly large span of wind speeds the curves can be represented by straight lines, though Mod-O and Kalkugnen at wind speeds slightly above the start-up speed

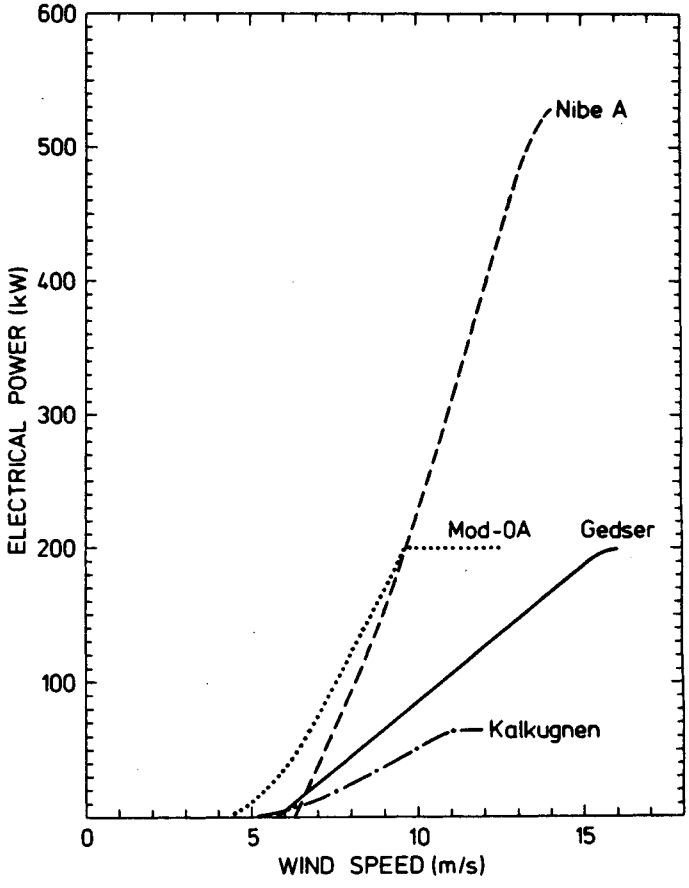

Fig. 6.9. Power curves.

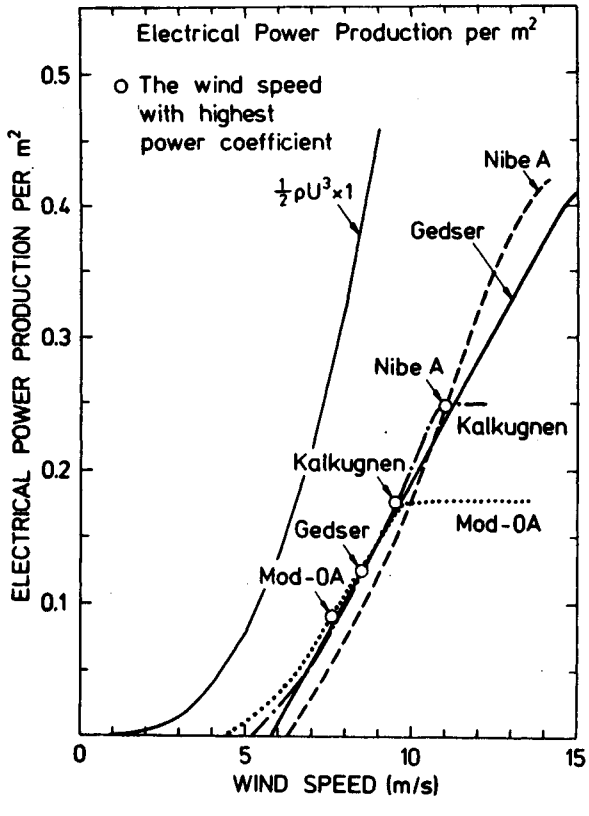

Fig. 6.10. Normalized power curves.

clearly have got more curvature than Gedser and Nibe A. This should actually be expected since the American and the Swedish turbines have continuous pitch regulation. The weak curvature on Nibe A is connected to the two-step pitch regulation (the pitch angle is changed 5 deg. at the wind speed 10 m/s).

The cut off power levels for Nibe A and Gedser are app. equal, while Kalkugnen and Mod-OA are designed to cut off at somewhat lower wind speeds, probably because of lower wind speeds of the sites.

Using the power curves of Fig. 6.9, the power coefficient curves were calculated as shown in Fig. 6.11. The maximum power coefficient for the different turbines are within ±6% of each other decreasing from 0.33 (Mod-OA) to 0.29 (Nibe A), while the corresponding wind speed at maximum power coefficient increases from 7.5 m/s to 11.0 m/s. The shape of the curves are similar, but the operational ranges are different, presumably designed to suit the local wind speed distributions.

One can characterize the wind speed distribution of a specific site in a good approximation by means of a Weibull distribution

$$f(v) = \frac{C}{A}\left(\frac{v}{A}\right)^{C-1} \exp\left(-\left(\frac{v}{A}\right)^{C}\right)$$

where just two parameters C and A decide the wind distribution. Choosing C = 2 the distribution simplifies into a Rayleigh distribution. Using this choice, the yearly average efficiency (i.e. yearly power production/year available energy flow through the rotor area) was calculated as a function of the Weibull parameter A. The result is shown in Fig. 6.12. The difference in maximum yearly average efficiency for the turbines is insignificant in view of the uncertainties involved in the power curve determination. We can conclude that the turbines are designed for different wind climates and - used at correct sites - are of comparable quality as far as production capabilities are concerned. Fig. 6.13 is a slightly different representation of the same data. It shows the yearly average production as a function of the same A.

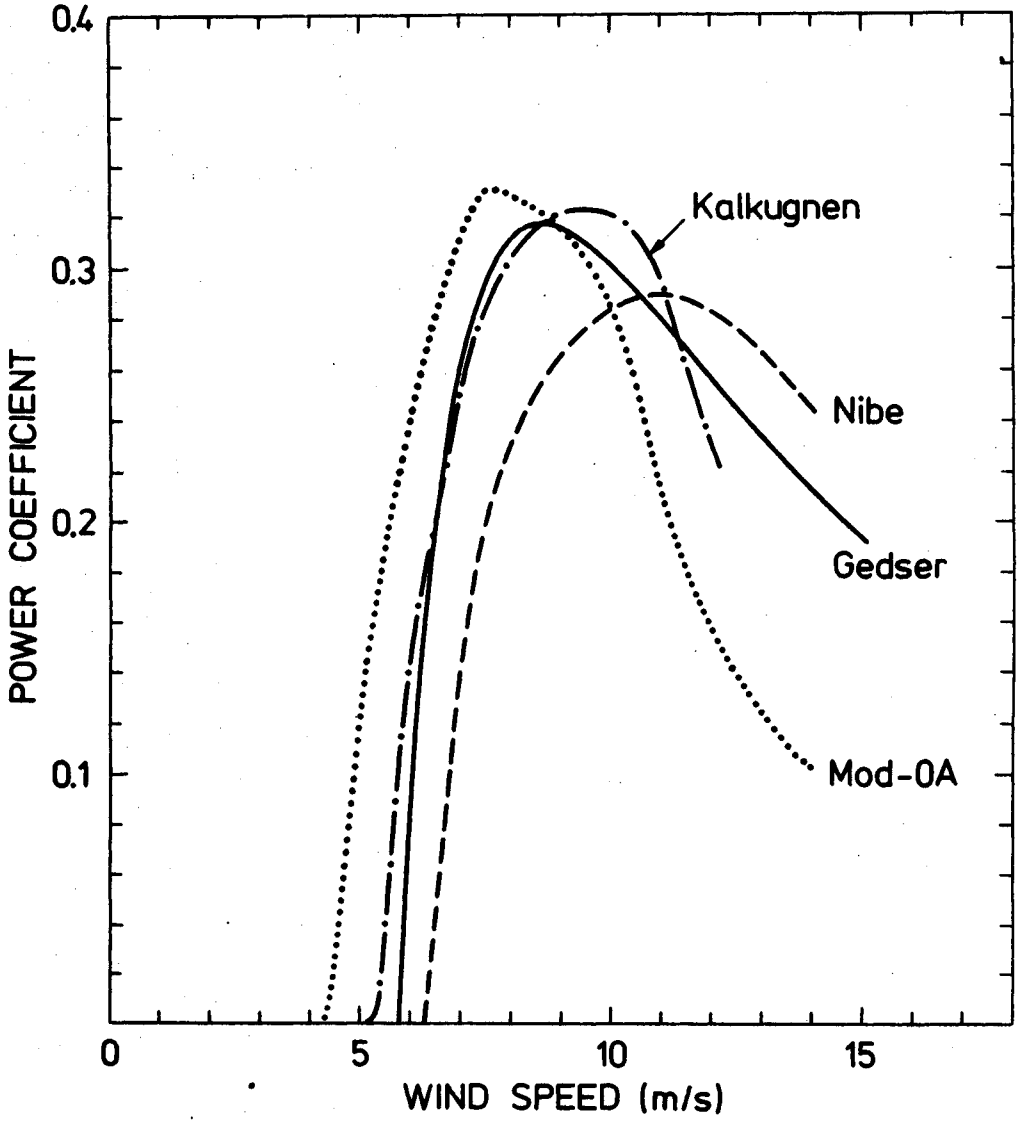

Fig. 6.11. Power coefficient curves.

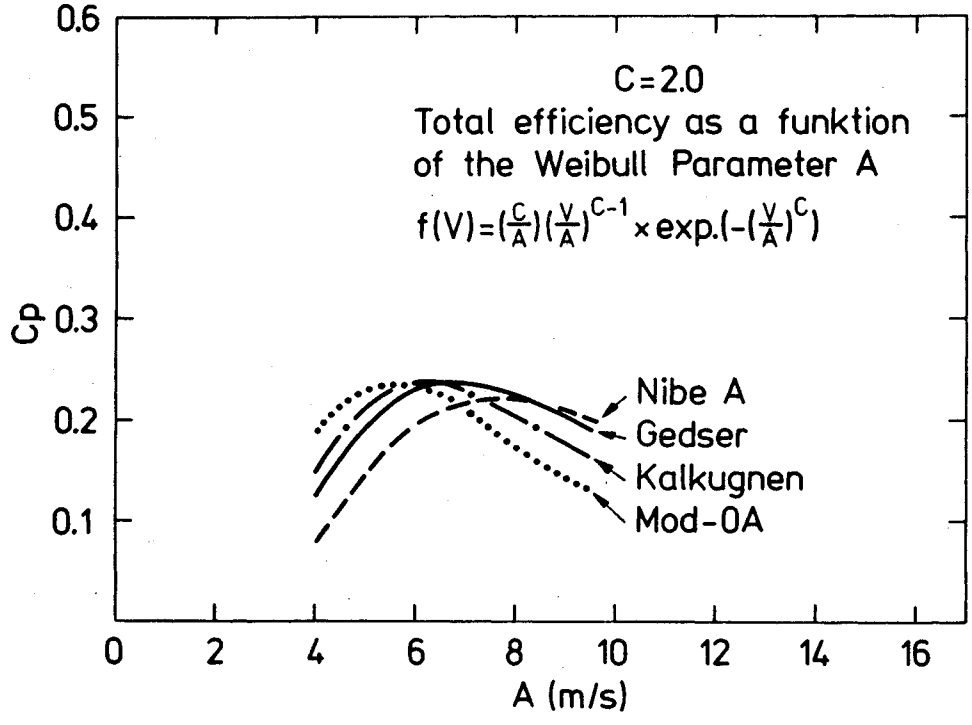

Fig. 6.12. Yearly average power coefficients as a function of the Weibull parameter A.

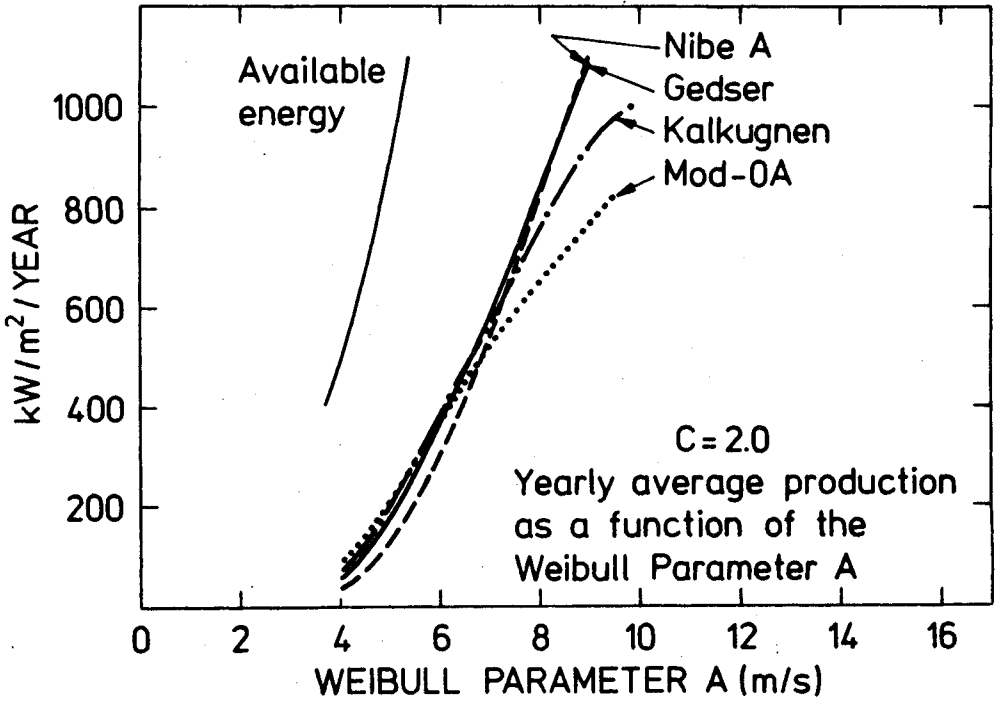

Fig. 6.13. Yearly production per m^2 as a function of the Weibull parameter A.

Conclusion concerning the Gedser turbine

Aerodynamically the Gedser turbine compares well with the three modern designs with which it has been compared. In spite of the stay systems and the rather primitive technology used in the blade assembly, the efficiency curve has the same peak value as the modern turbines.

The stresses are very low compared to those seen in the modern turbines. This is, of course, primarily a result of the stay system. The stays relieves the blades of the major part of the forces, especially the gravity forces and the out-of-plane wind load. In spite of the low forces, the blades were designed as a conservative, heavy construction. This design is presumably not suited for modern mass production, but is probably the prime reason why the rotor has survived 10 years of operation with ample fatigue life left for further operation.

The actual technological solutions chosen for the Gedser turbine are hardly applicable in modern designs due to the costs and some parts of the mechanical construction of the nacelle have proved to be unsuccessful, cf. Ref. 6.5. However, the fundamental principles of the Gedser turbine, a tip-stayed, three-bladed, upwind-located and stall-regulated rotor still appear to be one promising solution to the problem of designing a reliable wind turbine rotor.

REFERENCES

6.1. P. Lundsager, C.J. Christensen, S. Frandsen. "The Measurements on the Gedser Wind Mill 1977-1979". The Wind Power Program of the Ministry of Commerce and the Electric Utilities in Denmark. November 1979.

6.2. H.E. Neustadter, T.R. Richards, S.M. Sidik. "ERDA/NASA Wind Turbine Performance: I Mod-O Power Output". Rough draft.

6.2A. T.R. Richards, H.E. Neustadter. "DOE/NASA ModOA Wind Turbine Performance". NASA TM-78916, August 1978.

6.3. B. Lindkvist. Kalkugnen experimental wind power plant, rigid turbine hub configuration, report on testing, results and analysis. SAAB-SCAMA RRY-78.137, December 1978.

6.4. P. Lundsager, H. Petersen. Preliminary results from blade load measurements for the Nibe "A" wind turbine. Paper presented at the 4th Expert Meeting "Rotor blade technology with special respect to fatigue design problems" in Stockholm April 21st to 22nd, 1980.

6.5. Operational experiences with the Gedser Mill during the test period November 1977 to March 1979. (Driftserfaringer med Gedsermøllen i forsøgsperioden november 1977 - marts 1979). The wind power program of the Ministry of Energy and the Electric Utilities in Denmark. September 1979. (In Danish).

Appendix I. The accuracy of the converted data

The signals produced by the sensors during measurements experience a number of processes, before the final, converted data are available. The analog signals are amplified in one or more steps and digitized before being recorded as raw data, while pulse signals are being recorded directly. They are then converted to physical units using conversion expressions that may be available from the sensor manufacturer or determined by either laboratory tests or field tests. Finally the data are referred to some zero condition or reference state in order to obtain absolute results.

The contributions to the uncertainty of the results may be referred to one of three groups, namely deviations on the sensor signals converted into physical units, deviations due to the signals being transmitted to the recorders, and deviations of the reference state. The contributions to the deviations are commented upon below.

Sources of deviations

Sensor related deviations are:

Sensor signal deviations which are assumed to be insignificant compared to other sources.

Conversion/calibration deviations are estimated in table I.1 and in the reports Ref. I.1-2. They determine the magnitude of sensor related deviations.

Data transmission and recording deviations are:

Amplification deviations are assumed to be insignificant. Tests have shown that the gain of the rotor channel preamplifiers was very stable, and while this was not the case for the tower channel amplifiers, their gain may be checked by span check recordings.

Group	Quantity measured	Sensor	Manufacture	Range	Output	Operating Temp.range °C	Accuracy
Blade 3							
1	Blade section forces and stay forces	Strain gauge		± 500µStr.	± 1 V		
2	Differential pressure (stall)	Pressure transducer	Endevco	± 0.2 psi ± 0.4 psi	± 1 V	-15/+40	1%
Blade 2	Blade section forces and stay forces	Strain gauge		± 500µStr.	± 1 V		
3							
Tower	Forces between tower/nacelle (measuring cylinder)	Strain gauge	HBM		± 5 V	-40/+50	± 1 µStr.
4							
Nacelle							
5	Accelerations	Accellerometer	Schavitz	± 1 g	± 5 V	-40/+50	1%
5	Yaw rate	Gyro	Smiths	20 deg/sec	± 5 V	-40/+50	1%
6	Rotor position	Photo cell count	FORT	1/1 deg	TTL Pulse	-15/+40	
				1/360 deg	TTL Pulse	-15/+40	
6	Nacelle position	Potentiometer	Bourns	10 turns	± 10 V	-40/+50	1%
7	Transmission shaft torque	Strain gauge	HBM	± 200 µStr.	± 5 V FM	-40/+50	2%
Generator							
8	Voltage	Trafo	BBC	3 x 380 V	± 5 V	-40/+50	1%
8	Active power	Trafo	BBC	200 kW	± 5 V	-40/+50	1%
8	Reactive power	Trafo	BBC	200 KVAR	± 5 V	-40/+50	1%
Met.mast							
9	Wind vector and temperature	Ultrasonic anemometer	Kaijo Denki		± 1 V	-20/+50	±3%
10	Wind speed	Cup anemometer	Aanderaa 2219		Connected to Anderaa tape recorder	-40/+50	±2%
10	Wind direction	Wind vane	Aanderaa 2053	0-360° dead angle 3.5°		-40/+50	±5%
10	Air temperature	Pt-100	Aanderaa 1289	-44/+48°C			
10	Air pressure	Barometer	Yellow springs	914-1067 mb		-35/+83°C	0.3 mb
10	Air humidity	LiCl					
11	Wind speed	Cup anomometer	Risø 70				
11	Wind direction	Wind vane	Anderaa 2053	0-360° dead angle 3.5°			

Table I.1. Sensor specifications.

Digitizing deviations may occur in the digitizing process itself, but since this process is checked by span check recordings, these deviations are assumed to be insignificant except in a few cases where computed spectra will show digital white noise (rotor velocity, shaft moment).

Recording deviations may occur as a consequence of digitizing the analog signals. A typical resolution is 75 counts representing peak to peak values, and thus ~ 2% deviations may occur. However, channels with small resolutions may have considerably higher deviations. For pulse counting channels a deviation of one half pulse per scan is present, and the relative error then depends on the number of pulses recorded per scan.

These deviations determine the errors related to the data transmission.

Reference state deviations are:

Zero adjustment deviations caused by errors in alignments, or by zero drift of the instrumentation. They are errors affecting the absolute values of results, but they usually do not enter calculations involving differences of absolute results.

Reference state definition deviations occur on the rotor and measurement cylinder data due to problems in the definitions of a reference state. They are caused by the lack of long term zero stability of the sensors or amplifiers, that makes zero readings necessary before each run. Due to unknown external forces during zero recordings the reference state is not too well defined.

Accuracy of the channel groups

In this section the accuracies of the channel groups of table I.2 are estimated and the dominating sources of deviations are identified.

Group	Number of Channels	Transducers	Quantities measured
1	21	Strain gauge sensors on blade 3 and adjacent stays	Blade section forces and stay forces
2	5	Differential pressure transducers on blade 3	Differential pressures on blade 3
3	19	Strain gauge sensors on blade 2 and adjacent stays	Blade section forces and stay forces
4	5	Strain gauge sensors on measuring cylinder	Forces between nacelle and tower top
5	4	Accelerometers in nacelle	Linear and angular accelerations, yaw rate
6	3	Pulse counters and potentiometer in nacelle	Rotor positions ($1/1^{o}$ and $1/360^{o}$) and nacelle position
7	2	Strain gauge sensors on transmission shafts	Transmission and generator shaft torque
8	3	Electrical power transducers	KWATT, KVAR and Volt
10	9	Various sensor	Meterological wind condition data
11	2	Anemometer and wind vane	Wind speed and direction at hub heigth

Table I.2. Sensor groups

Rotor channels, groups 1 and 3

Typically 30 to 60 counts represent peak to peak values. Together with the coefficients of variation 0.04-0.10 stated in the laboratory test report this results in estimated coefficients of variation in the range 0.06-0.12. This is valid for converted data representing the difference between run data and zero run data. The conversion into absolute data referring to a common zero load state implies model considerations, and the deviations caused by the reference state depend strongly on the assumptions made in the conversion. Consequently they cannot be estimated here.

Measurement cylinder channels group 4

Typically 30 to 60 counts represent peak to peak values. Together with the coefficients of variation 0.07 to 0.23 stated in the measurement cylinder report this results in estimated coefficients of variations of 0.07 to 0.23. These values also include zero reference deviations for zero wind speed, but the conversion to absolute values of run data meet the same problems as the rotor channel data dealt with above.

Accelerometers group 5

Peak to peak values are typically represented by 30 to 70 counts. This is the dominating deviation, and estimated coefficient of variation thus is 0.03.

Position indicators group 6

The rotor position indicator is a pulse counting channel in both versions used. The angle of rotation during each scan is determined with a relative error of 14%, but it is estimated that by averaging a number of scans the rotor position may be determined with an accuracy of ±1 deg. In the new version the rotor speed is determined with an estimated accuracy of about 2% due to the large number of pulses recorded during a scan.

The nacelle position indicator has an estimated zero alignment error of ±2.5 deg, while the resolution is estimated as ±1 deg. However, during a number of the runs the readings are erroneous, presumably due to amplifier instability.

Shaft torque group 7

A poor resolution of the signal expressed in pulses per scan dominates the deviations on this channel. The coefficient of variation is estimated in the range 0.10-0.20.

Power measurements group 8

Calibration and recording errors are assumed to be equally important and to result in a coefficient of variation of less than 0.05.

Short term wind measurements group 11

Recording errors are assumed to be dominant for the wind speed measurement, an estimated coefficient of variation being 0.03. For the wind direction measurements a zero alignment error of ±2.5 deg. is estimated, while relative readings are estimated accurate within ±1 deg.

Long term wind measurements group 10

Due to the long averaging time, average wind speeds have an assumed relative error of less than 1%. The wind directions being instantaneous measurements the accuracy estimates are ±2.5 deg. absolute and ±1 deg. relative as above.

Conclusions

The main sources of deviations of the recorded data are uncertainties of rotor signals and their conversion into physical units. The data transmission and recording system does not contribute significantly to the deviations except when the resolution is small. In that case errors due to the digital representation of the signals may become significant. Estimated relative errors lie in the range 1-12% except for some of the

measurement cylinder channels, and on basis of this it seems reasonable to conclude that the data generally have an accuracy that makes analysis using current analytical models meaningful.

REFERENCES

I.1. V. Askegaard, P. Mossing. "Instrumentation and Calibration of Measuring Cylinder on Gedser Wind Turbine". Structural Research Laboratory, Technical University of Denmark, Report S28/77 1978.

I.2. V. Askegaard, C. Dyrbye, S. Gravesen. "Laboratory Tests on Gedser Wind Turbine's Blades". Structural Research Laboratory, Technical University of Denmark, Report S 28/77. (November 1977).

Appendix II. Zero correction of data

Definition of reference zero

The definition of a common reference state for the turbine, a reference zero, poses some problems for a number of the sensors. The instrumentation was not stable enough to allow for a zero adjustment once and for all. It was necessary to define a reproducible reference condition, where a zero-calibration reading could be taken before each run (stopped turbine, blade 3 down).

In this reference condition, however, not all sensors are exposed to a physical zero force (or whatever the sensor measures). Both the wind load and gravity forces will be present and distributed on the rotor in a somewhat arbitrary way, as the rotor is statically indeterminate. Therefore, the sensor reading R_i^o taken during a zero-(reference-)run does not represent a force free condition ($F_i^o \equiv 0$) but rather the real reference force $F_i^o \neq 0$ present. During the real run a reading R_i is obtained, which in turn corresponds to a force F_i, i.e.:

$$\begin{aligned} R_i^o &\rightarrow F_i^o \\ R_i &\rightarrow F_i \\ R_i - R_i^o &\rightarrow F_i - F_i^o \neq F_i \end{aligned} \qquad \text{II.1}$$

Now, if the calibration factor a_i and the reference force F_i^o are known:

$$\begin{aligned} F_i - F_i^o &= a(R_i - R_i^o) \\ F_i &= a(R_i - R_i^o) + F_i^o \end{aligned} \qquad \text{II.2}$$

Thus because of the reference zero problem the force must be determined through two stages:

1) measuring the force change from the reference state to the run
2) adding the force present in the reference state and usually to be calculated.

Fig. II.1 shows an example of this problem namely the bending moment M_3. The loading in the top of the figure represents the calculated value of the non-zero load F_i^o during the zero run.

Load case two exemplifies the real load F_i that one attempts to measure, whereas load 3 is the erroneous result

$$F_i = a(R_i - R_i^o) \qquad \text{II.3}$$

if one fails to correct for the zero-state load.

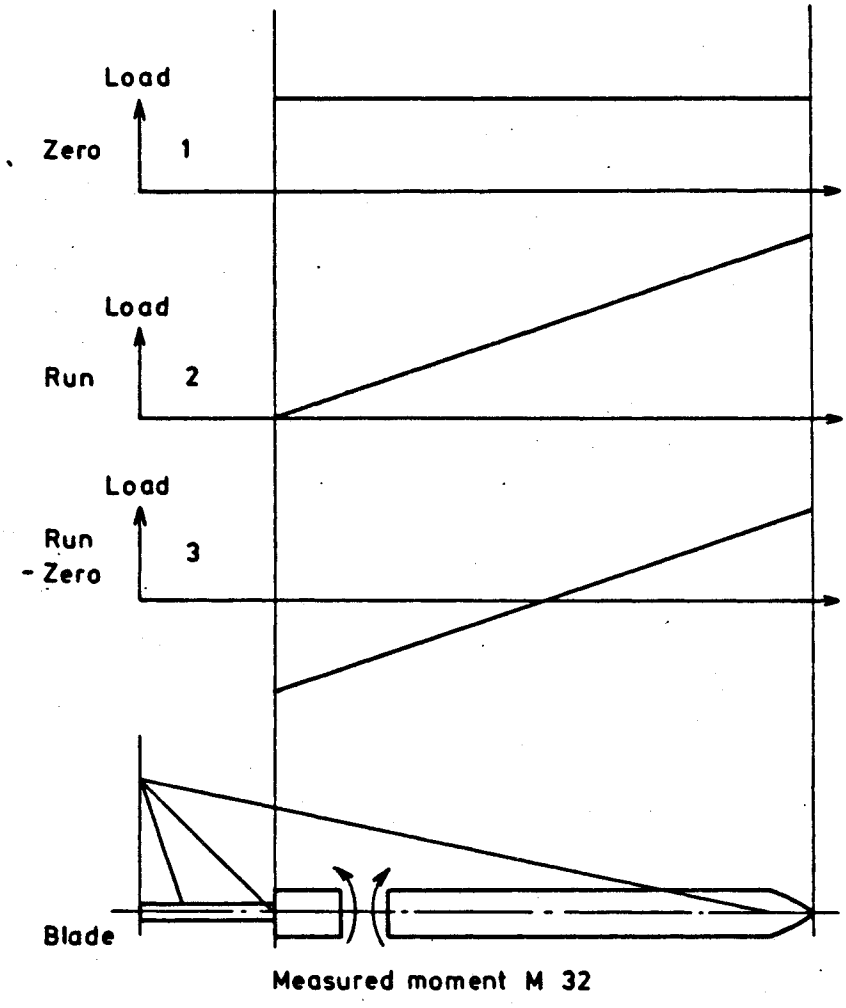

Fig. II.1. Zero correction

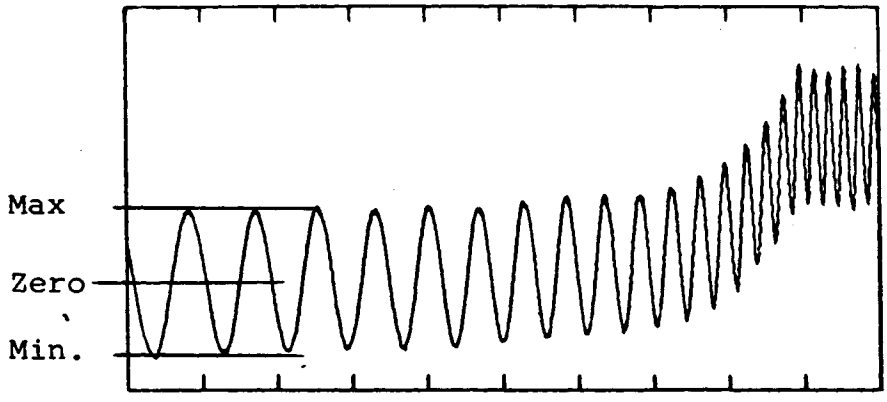

Fig. II.2. Dynamic zero

The determination of the moment F_{io} under the zero condition cannot be done by measurement because of the zero drift of the instrumentation. It therefore must be done by calculation, which poses two problems:

- The wind load distribution is not known and has to be calculated according to some set of assumptions (wind load model).
- The gravity load distribution is not well known except for a determination of total mass and centre of gravity.

Furthermore the Gedser mill rotor is statically indeterminate due to the stays, and the moment distribution due to wind and gravity loads therefore must be calculated by means of the same structural model that should be verified by the measurements. It is therefore not possible to obtain results, that refer to a common basis, by measurements alone. This is true for the entire rotor instrumentation.

Two types of zero measurements have been made before runs:

a. Static zero, measured while the rotor is stopped. There are no dynamic effects, but the measurement includes effects from wind forces and gravity forces.

b. Dynamic zero, computed from measurements during upstart when the rotor is rotating slowly. Typically one revolution lasted 20 sec. during this measurement, corresponding to a tip velocity of less than 4 m/s and a centrifugal accelera-

tion of 0.1 m/s^2 per meter radius. These values are about 10% of values during run.
There may be small dynamic effects, and the wind loads may be larger than under static zero (but not necessarily more difficult to calculate to a given accuracy). But gravity effects are usually averaged out by using this dynamic procedure. Fig. II.2 exemplifies this dynamic zero procedure.

For most of the runs both types of zero readings are available, but in the documentation of the processed runs dynamic zero values are used to correct the measured values according to Eq. II.2.

The beam model used in zero correction

The structural model used to calculate the rotor forces due to wind load during dynamic zero measurements is a conventional beam finite model.

The cross sectional properties were computed using a special purpose program Ref. II.1 Fig. II.3 shows a typical cross section, and the center locations are indicated. The beam model analyzed using the general purpose program SAP Ref. II.2, is shown schematically in Fig. II.4. The blade pretwist is represented by individual rotation of the principal axes of each element. The model was checked against the laboratory tests Ref. II.3 as shown in Fig. II.5, where the deflections of the blade without stays are shown.

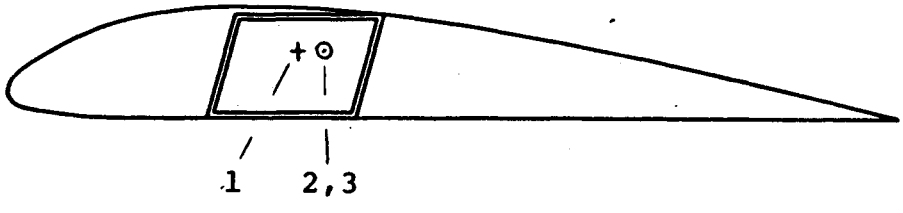

Fig. II.3. Calculated positions of 1. Shear center, 2. Elastic center and 3. Mass center in the blades.

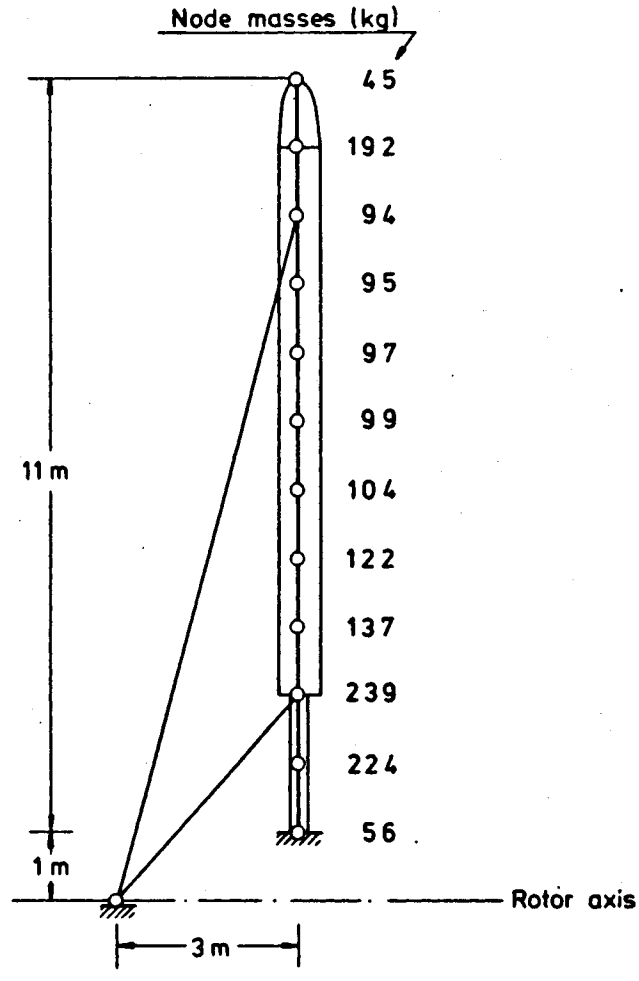

Fig. II.4. The beam model used for the computation of blade overall response.

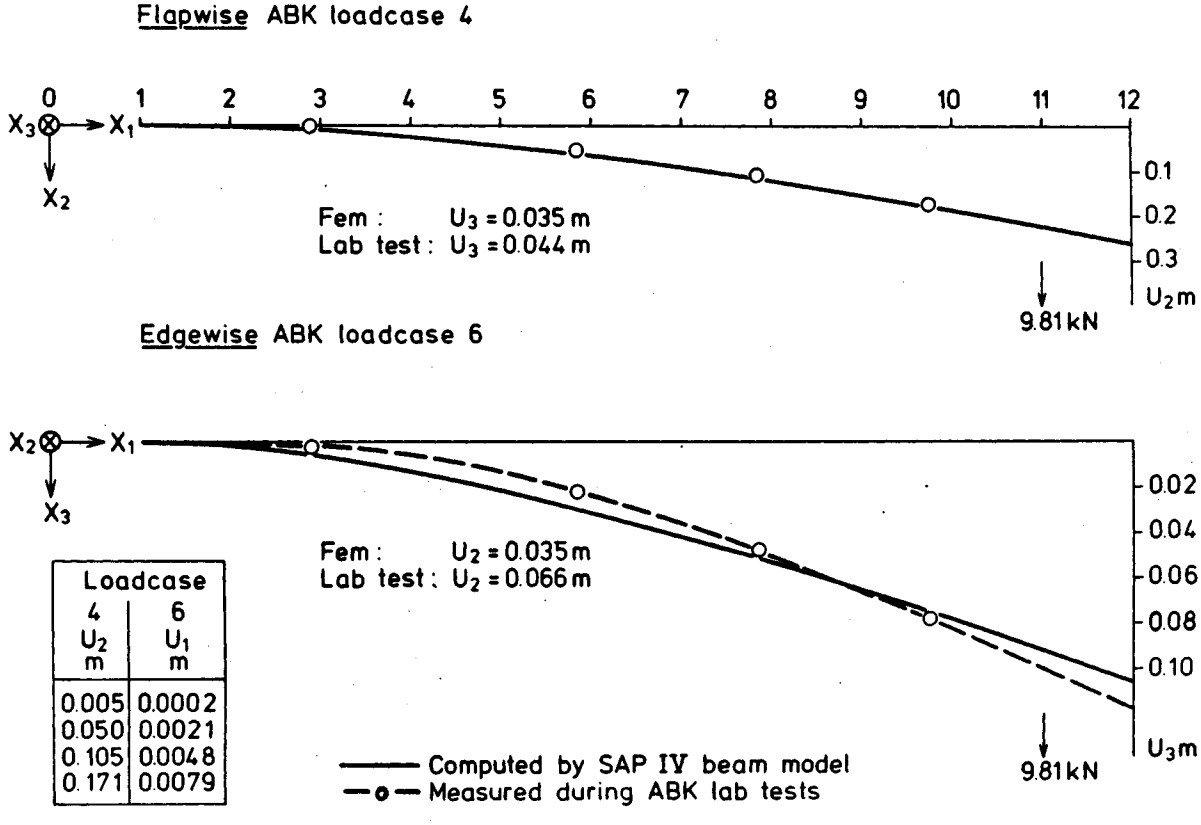

Loadcase 4 U_2 m	6 U_1 m
0.005	0.0002
0.050	0.0021
0.105	0.0048
0.171	0.0079

Fig. II.5. Comparison of beam model with laboratory test, (ref. II.3).

The blade model and a rotor model based on three blade models were checked against eigenfrequencies measured early in the measurement period, Ref. II.4. Figs. II.6 and II.7 show bending moments and deflections, respectively, computed using the beam model.

3. Calculated zero corrections

The bending moments and stay forces due to the wind load during zero measurements are shown in Fig. II.8. The wind load is assumed to be evenly distributed over the length of the aerofoil part of the blade, and the load intensity is calculated assuming $C_D = 1.0$. The load is supposed to act in the out-of-plane direction only.

The quantity $F_{io}(v)$ to be used in Eq. II.2 for the wind speed v is derived from the values $F_{io}(12)$ of Fig. II.8 by means of the equation

$$F_{io}(v) = \left(\frac{v}{12}\right)^2 \cdot F_{io}(12) \qquad \text{II.4}$$

The forces and moments are too large to be neglected.

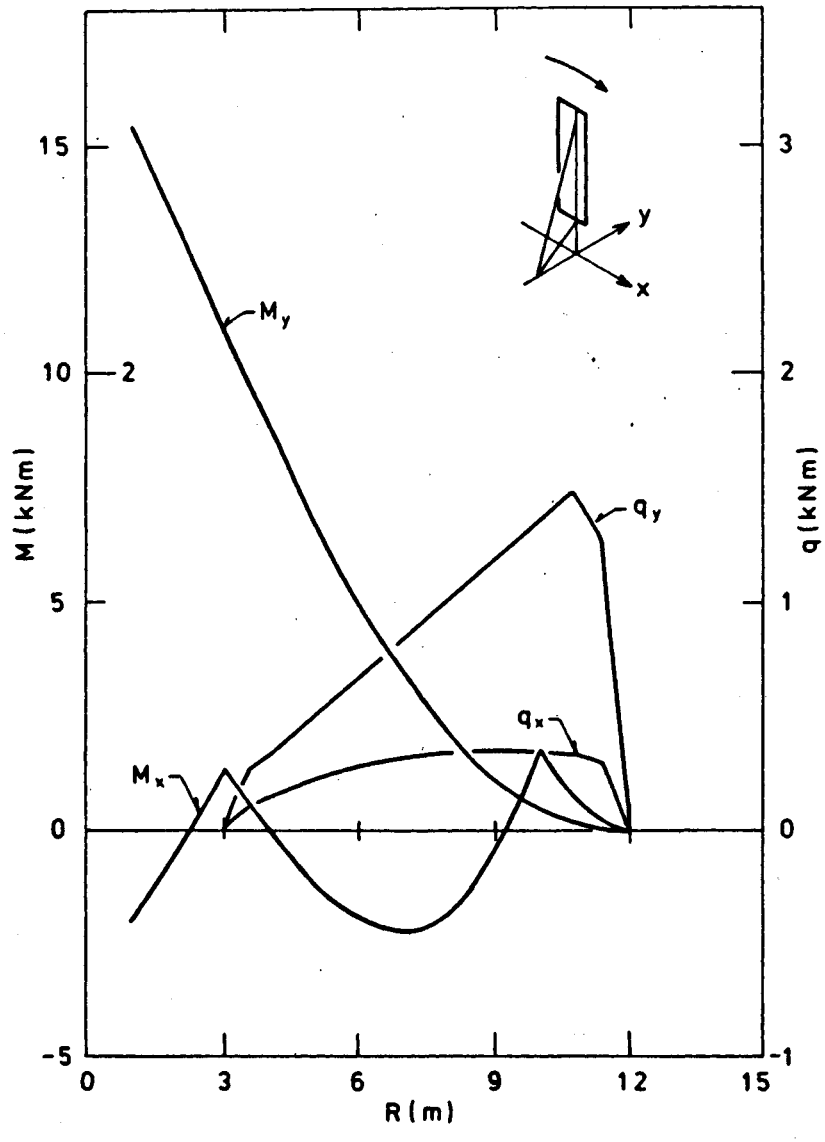

Fig. II.6. Bending moments calculated by the beam model for 12 m/s wind.

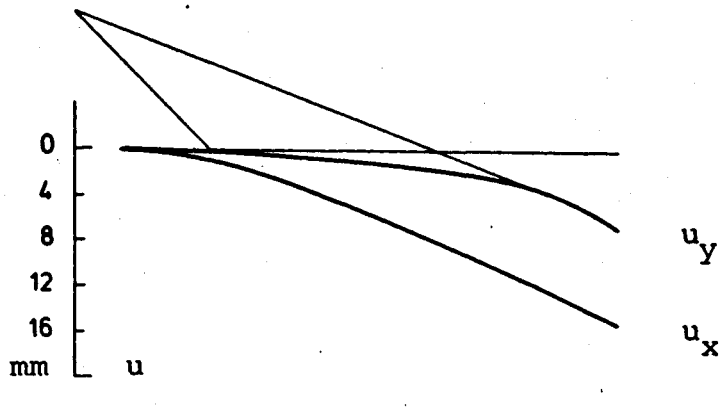

Fig. II.7. Deflection pattern calculated by the beam model for 12 m/s wind.

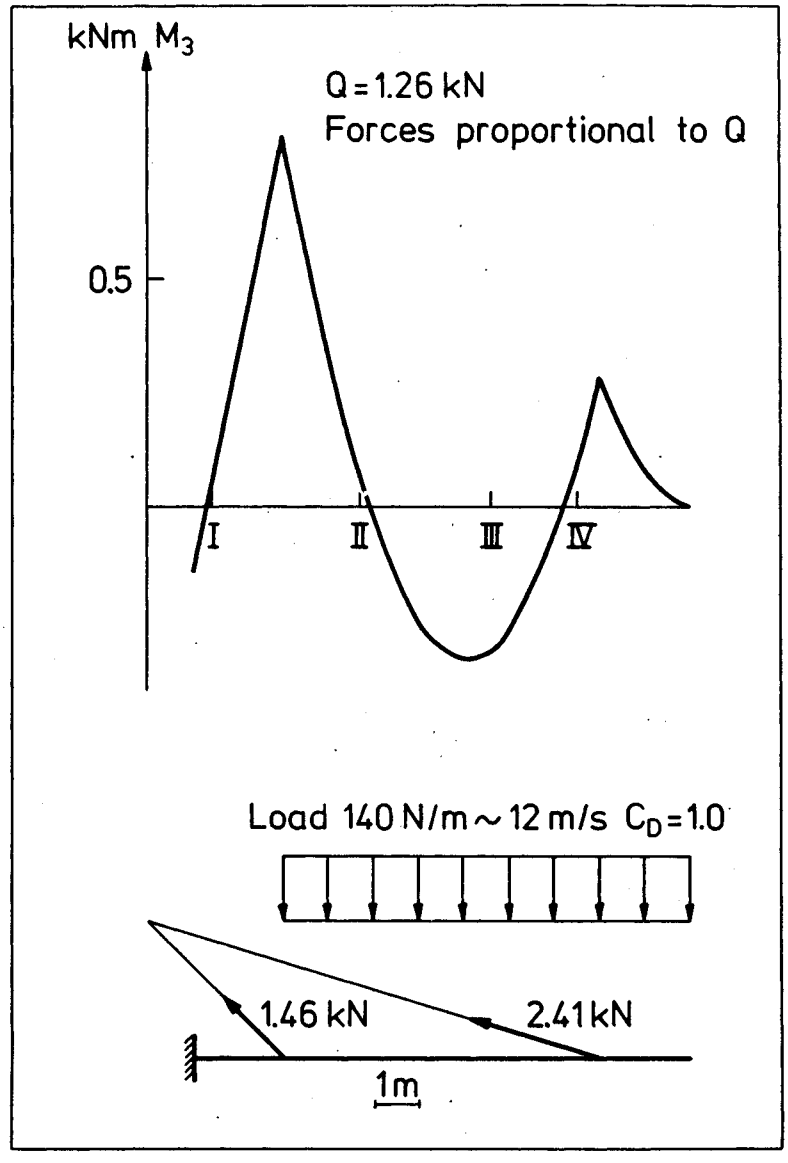

Fig. II.8. Loads due to wind load during zero measurements.

REFERENCES

II.1. P. Lundsager. "SECTIO-A Program for the Determination of Cross Sectional Properties of Closed, Thinwalled Beams". Risø-M-2159 July 1979.

II.2. SAP IV: Structural Analysis Program for Static and Dynamic Response of Linear Systems. Asea Atom Computer Program Rol058, 1976.

II.3. V. Askegaard, C. Dyrbye, S. Gravesen. "Laboratory Tests on Gedser Wind Turbine's Blades". Structural Research Laboratory, Technical University of Denmark, Report S 28/77. (November 1977).

II.4. P. Lundsager, C.J. Christensen, S. Frandsen. The measurements on the Gedser Wind Mill 1977-1979, Gedser test group 771.105-3, The wind power program of the Ministry of Commerce and the Electric Utilities in Denmark. (November 1979).

Risø National Laboratory **Risø - M - 2242**

Risø - M - 2242

Title and author(s)

ANALYSIS OF DATA FROM THE GEDSER WIND TURBINE 1977-1979

P. Lundsager, S. Frandsen, C.J. Christensen

Date August 1980

Department or group

Department of Physics

Group's own registration number(s)

136 pages + 7 tables + 53 illustrations

Abstract

In this report a number of topics have been chosen for further analysis, based on the data from the Gedser wind turbine measurements, made during 1977 to 1979. The report contains chapters dealing with power characteristics based on 10 min. averages, coherence between measurements of wind and electric power based on high speed scanning, drive train oscillations and structural response of the rotor. In most of the chapters theoretical models are developed and evaluated. First chapter contains a summary of the measurements and last chapter contains a comparison of the Gedser wind turbine with modern Danish, Swedish and American experimental wind turbines, based on published data.

Copies to

Standard distribution

Available on request from Risø Library, Risø National Laboratory (Risø Bibliotek), Forsøgsanlæg Risø), DK-4000 Roskilde, Denmark
Telephone: (03) 37 12 12, ext. 2262. Telex: 43116